

The central inner z-chamber of the  
H1 experiment at HERA

Inaugural Dissertation  
zur Erlangung der Philosophischen Doktorwürde  
vorgelegt der  
Philosophischen Fakultät II  
der  
Universität Zürich

von  
Peter Robmann  
aus Turbenthal ZH

begutachtet von Prof. Dr. P. Truöl

Zürich 1994

The central inner z-chamber of the  
H1 experiment at HERA

Inaugural Dissertation  
zur Erlangung der Philosophischen Doktorwürde  
vorgelegt der  
Philosophischen Fakultät II  
der  
Universität Zürich

von  
Peter Robmann  
aus Turbenthal ZH

begutachtet von Prof. Dr. P. Truöl

Zürich 1994

## Zusammenfassung

HERA, die Hadron Elektron Ring Anlage, ist der Elektron Proton Speicherring am Deutschen Elektronen-Synchrotron (DESY) in Hamburg. In zwei übereinanderliegenden Ringen werden Pakete der Teilchen gespeichert und schliesslich auf höhere Energien beschleunigt. Die Sollenergien von 30 GeV Elektronen und 820 GeV Protonen ergeben eine Gesamtenergie im Elektronen-Protonen-Schwerpunktsystem von 314 GeV. Sie liegt um mehr als einen Faktor zehn über den bisher in Lepton-Nukleon-Streuexperimenten erreichten Energien. In der Mitte der beiden Detektoren H1 und ZEUS treffen die Elektronen und Protonen frontal aufeinander. Die Elektronen-Quark und Elektronen-Gluon Kollisionen in einem neuen kinematischen Bereich führen die klassischen Streuexperimente mit Elektronen, Myonen und Neutrinos weiter. Um das breit gefächerte Spektrum von Reaktionen zu verstehen, ist eine gute Teilchenidentifikation unumgänglich.

In dieser Arbeit werden die Entwicklung, die Konstruktion und der Betrieb der innersten Driftkammer des H1 Detektors beschrieben. Sie erlaubt eine präzise Bestimmung der z-Koordinaten von geladenen Teilchen und damit eine gute Impulsauflösung. Um die Wahrscheinlichkeit für störende Streuprozesse so gering wie möglich zu halten, wurden bei der Konstruktion die Dicken und Dichten aller nötigen Materialien so klein wie möglich gewählt. Eine weitere Herausforderung bestand darin, die Bereiche von nicht aktiven Zonen zu minimieren.

Im ersten Teil werden das H1 Experiment und die Grundlagen zum Bau von Driftkammern diskutiert. Dann werden Simulationsrechnungen und Abschätzungen dargestellt. Vergleichend mit Driftzellen in bisher verwendeten Detektoren wird auf die Eigenheiten, der in unserem Detektor neu implementierten Konstruktion mit geeigneten Drahtebenen hingewiesen. Mit der Beschreibung der Konstruktion endet dieser zentrale Teil. In den abschliessenden Kapiteln werden die Elektronik, die Analyse der Kammerpulse und erste Resultate vom Betrieb der Kammer im H1 Experiment beschrieben.

## Abstract

HERA, the Hadron Electron Ring Accelerator, is the electron-proton storage ring at the DESY Laboratory (Deutsches Elektronen-Synchrotron) in Hamburg, Germany. In two rings the particles are stored and finally accelerated to higher energies. The design energies of 30 GeV electrons and 820 GeV protons result in a center of mass energy of 314 GeV. This is more than a factor of ten above the energies reached so far in lepton-nucleon scattering experiments. In the center of the two detectors H1 and ZEUS the electrons collide with the protons. The electron-quark and electron-gluon collisions in a new kinematical domain carry on the classical scattering experiments done with electrons, muons and neutrinos. To understand the wide area of physics prime attention has to be given to a clean particle identification.

This thesis describes the development, the construction and the operation of the innermost drift chamber of the H1 detector. The chamber allows a precise measurement of the z-coordinate of charged particles and therefore a good momentum resolution. To keep the probability for secondary scattering processes as low as possible the thickness and the density of all used parts was minimized. The dead zones of the detector were reduced as much as possible.

The first part describes the H1 experiment, and the basics of drift chambers are discussed. Then simulations and estimations are presented. In comparing with standard drift cells, the peculiarities of our detector with tilted wire planes are pointed out. This central part finishes with a description of the construction. The concluding chapters deal with the electronics, the analysis of the chamber pulses, and first results of the operation at the H1 experiment are presented.

# Contents

<b>1</b>	<b>General introduction to ep-physics</b>	<b>9</b>
1.1	Motivation . . . . .	9
1.2	Deep inelastic scattering . . . . .	10
1.3	Hard scattering of almost real photons . . . . .	15
<b>2</b>	<b>Charged particles within the H1 detector</b>	<b>17</b>
2.1	General description of the H1 detector . . . . .	17
2.2	Synchrotron radiation shielding . . . . .	21
2.3	The H1 tracking system in the central region . . . . .	22
2.4	Momentum measurement . . . . .	25
2.4.1	Momentum resolution and spatial resolution in z . . . . .	25
2.4.2	Influence of multiple scattering . . . . .	28
<b>3</b>	<b>General aspects of drift chambers</b>	<b>32</b>
3.1	Introduction . . . . .	32
3.1.1	The drift chamber . . . . .	33
3.2	Detection of charged particles . . . . .	34
3.2.1	Energy loss due to electromagnetic interaction . . . . .	34
3.2.2	Statistical distribution of ion pair production . . . . .	36
3.3	Drift and diffusion of charges in gases with electric and magnetic field . . . . .	39
3.3.1	Mobility of ions . . . . .	39
3.3.2	Drift and diffusion of electrons in electric and magnetic fields . . . . .	40
3.4	Loss of primary ion pairs by recombination and electron capture . . . . .	41
3.5	Excitation and ionization in high electric fields . . . . .	42
3.6	Resolution of the particle track coordinate measuring the drift time . . . . .	45
3.7	Determination of the coordinate along the anode wire . . . . .	47

<b>4</b>	<b>Design considerations for the inner z-chamber</b>	<b>50</b>
4.1	Choice of the drift cell geometry . . . . .	50
4.2	Electrostatic simulations . . . . .	52
4.2.1	Electrostatic simulation of the drift cell chosen . . . . .	53
4.2.2	The coupling between the drift field and the gas amplification field	53
4.2.3	Influence of the field forming strip width . . . . .	57
4.2.4	Influence of double / single layered field forming strips . . . . .	57
4.2.5	Dependence of the electric field on mechanical tolerances . . . . .	61
4.3	Simulation of the drift lines and times . . . . .	62
4.3.1	Choice of gas mixtures . . . . .	62
4.3.2	Simulation studies without magnetic field . . . . .	63
4.3.3	Influence of the magnetic field . . . . .	65
4.4	Estimation of the gas gain . . . . .	67
4.5	Development of the signal . . . . .	70
4.6	Geometrical acceptance of the detector and simulated response . . . . .	72
<b>5</b>	<b>Construction of the drift chamber</b>	<b>75</b>
5.1	Overview . . . . .	75
5.2	Mechanical aspects . . . . .	76
5.2.1	Construction techniques . . . . .	76
5.2.2	Cell boundaries . . . . .	79
5.2.3	Field forming strip foil . . . . .	80
5.3	Detector parameters . . . . .	82
5.4	Gas system . . . . .	84
<b>6</b>	<b>Electronic</b>	<b>86</b>
6.1	The high voltage system . . . . .	86
6.2	The analog signal electronics . . . . .	89

<b>7</b>	<b>The readout and trigger system</b>	<b>93</b>
7.1	The central part of the H1 data acquisition system . . . . .	93
7.2	The trigger system . . . . .	93
7.3	The drift chamber readout system . . . . .	96
7.3.1	Overview . . . . .	96
7.3.2	FADC card . . . . .	98
7.3.3	Scanner card . . . . .	99
7.4	The slow control system . . . . .	100
<b>8</b>	<b>Pulse shape analysis and space point reconstruction</b>	<b>102</b>
8.1	Introduction . . . . .	102
8.2	Determination of the charge and the time (Qt analysis) . . . . .	102
8.2.1	Timing algorithms . . . . .	103
8.2.2	Characteristic drift time distributions . . . . .	104
8.2.3	Charge integration and characteristic distribution . . . . .	104
8.3	Space point reconstruction . . . . .	105
8.3.1	General . . . . .	105
8.3.2	Reconstruction of CIZ segments . . . . .	106
8.3.3	Linking CIZ hits to CJC segments . . . . .	107
8.4	Calibration constants and their determination . . . . .	108
<b>9</b>	<b>Chamber performance — cosmic and test beam data</b>	<b>111</b>
9.1	Intrinsic resolution . . . . .	111
9.2	Combined resolution . . . . .	112
<b>10</b>	<b>Chamber performance at HERA</b>	<b>117</b>
10.1	Operation at HERA . . . . .	117
10.2	Efficiency . . . . .	118
10.3	Correlation of beam and chamber currents . . . . .	119
10.4	Estimation of the total accumulated charge . . . . .	123
10.5	Analysis of the wire surfaces . . . . .	123
<b>11</b>	<b>Summary</b>	<b>126</b>

## List of Figures

1.1	Feynman diagrams . . . . .	10
1.2	Basic diagram . . . . .	11
1.3	Scattered electron angle and energy . . . . .	12
1.4	Current jet angle and current jet energy . . . . .	14
1.5	Domains in the $x, Q^2$ plane, where the systematic errors on $d^2\sigma/(dx dQ^2)$ are below 10% . . . . .	15
1.6	$D^*$ reconstruction . . . . .	16
2.1	Longitudinal cut through the H1 detector . . . . .	19
2.2	Transverse cut through the H1 detector . . . . .	20
2.3	Front view of the H1 detector . . . . .	20
2.4	Arrangement of the synchrotron masks . . . . .	22
2.5	The H1 tracking system ( $rz$ view) . . . . .	23
2.6	Central tracking system . . . . .	24
2.7	Track coordinate in $rz$ . . . . .	27
2.8	Resolution improvement by $z$ -chambers . . . . .	29
2.9	Resolutions for different momenta . . . . .	29
2.10	Multiple scattering at a given polar angle . . . . .	30
2.11	Multiple scattering in the beampipe wall . . . . .	31
3.1	Multiwire proportional chamber . . . . .	33
3.2	Drift chamber . . . . .	34
3.3	Energy loss . . . . .	35
3.4	Relative probability of different processes . . . . .	36
3.5	Landau distribution . . . . .	37
3.6	Space distribution . . . . .	38
3.7	Drift velocity . . . . .	42
3.8	Attachment coefficient . . . . .	43
3.9	Gain-voltage characteristics . . . . .	43



3.10	Simulated avalanche . . . . .	44
3.11	First Townsend coefficient . . . . .	45
3.12	Track coordinate errors . . . . .	46
3.13	Charge division . . . . .	47
3.14	Signal charge versus input resistance . . . . .	49
3.15	Charge division resolution versus input resistance . . . . .	49
4.1	Standard driftcell . . . . .	50
4.2	CIZ driftcell . . . . .	51
4.3	Geometrical layout of the CIZ driftcells . . . . .	51
4.4	Electrostatics of a standard cell . . . . .	53
4.5	Electrostatics of a CIZ cell . . . . .	54
4.6	Field with low potential wire voltage . . . . .	54
4.7	Field near the wires in CIZ cell . . . . .	55
4.8	Field near the wires in standard cell . . . . .	55
4.9	Field with high potential wire voltage . . . . .	56
4.10	Relation between the applied voltages . . . . .	56
4.11	Field near the 4 mm wide strips . . . . .	58
4.12	Field near the 4 mm wide strips . . . . .	58
4.13	Field near the 2 mm wide strips . . . . .	59
4.14	Field near the 2 mm wide strips . . . . .	59
4.15	Field distortion near the gaps . . . . .	60
4.16	Using double layered strips . . . . .	60
4.17	Influence of two shortened strips . . . . .	61
4.18	Influence of two shortened strips . . . . .	61
4.19	Field configuration, with moved cover . . . . .	62
4.20	Drift velocity and diffusion . . . . .	63
4.21	Simulated drift lines in a CIZ cell . . . . .	63
4.22	Drift distance versus field and time . . . . .	64

4.23	Drift distance versus field and time . . . . .	65
4.24	Influence of the magnetic field . . . . .	65
4.25	Drift region boundaries and isochrone shape . . . . .	66
4.26	Influence of the magnetic field . . . . .	67
4.27	Multiplication factor from Charles . . . . .	68
4.28	Multiplication factor versus the electric field . . . . .	69
4.29	Circuitry representing one drift chamber ring . . . . .	70
4.30	Induced current for different angles . . . . .	71
4.31	Simulated response . . . . .	71
4.32	Geometrical layout and deadzones . . . . .	72
4.33	Acceptance of the different wires . . . . .	73
5.1	Sketch of the drift chamber . . . . .	75
5.2	Longitudinal cross section . . . . .	76
5.3	Cross section of the CIZ . . . . .	77
5.4	Photograph, showing the CIZ during construction . . . . .	78
5.5	Cross section and longitudinal cut . . . . .	79
5.6	Wall on the wire end . . . . .	80
5.7	Wire support with built in resistor chain . . . . .	81
5.8	Field forming strip foil . . . . .	81
5.9	Radiation thickness . . . . .	83
5.10	Sketch of the gas system . . . . .	85
6.1	High voltage system layout . . . . .	86
6.2	Schematic of the high voltage circuit . . . . .	87
6.3	Schematic of the current meter . . . . .	88
6.4	Relation of the supply voltages . . . . .	89
6.5	Schematic of the linedriver . . . . .	90
6.6	Overview of the signal electronics . . . . .	91
6.7	Influence of the linedrivers . . . . .	91

6.8	Circuit of the H1 drift chamber amplifier . . . . .	92
7.1	Physical layout of the H1 data acquisition . . . . .	94
7.2	Overview over the trigger system . . . . .	95
7.3	H1 trigger levels . . . . .	96
7.4	The drift chamber readout system . . . . .	97
7.5	FADC response function . . . . .	100
7.6	Slow control system . . . . .	101
8.1	Typical pulse . . . . .	103
8.2	Characteristic drift time distribution . . . . .	104
8.3	Characteristic charge distribution . . . . .	105
8.4	Calibration constants $t_0^{offset}$ and $v_D$ . . . . .	108
8.5	Charge division from cosmic tracks . . . . .	109
9.1	Deviation of the single wires . . . . .	111
9.2	Chamber resolution . . . . .	112
9.3	Combined resolution in $z$ . . . . .	113
9.4	Systematic shifts due to miscalibration . . . . .	114
9.5	Resolution in $\phi$ . . . . .	115
10.1	Number of hits per event . . . . .	117
10.2	Potential wire current during the 1993 luminosity periode . . . . .	118
10.3	Efficiency and cathode voltage . . . . .	119
10.4	Potential wire current correlations . . . . .	120
10.5	Electron and proton currents for a proton filling . . . . .	121
10.6	Potential wire correlations for one electron filling . . . . .	122
10.7	Potential wire current measured only with electrons . . . . .	122
10.8	Potential wire current versus the electron beam current . . . . .	123
10.9	Elements found on sense wire surface . . . . .	124
10.10	Elements found on potential wire surface . . . . .	124
10.11	Photograph of a sense wire . . . . .	125
10.12	Photograph of a potential wire . . . . .	125
11.1	High $Q^2$ event seen in the H1 detector . . . . .	127

## List of Tables

1.1	Summary of HERA parameters . . . . .	9
2.1	Summary of H1 detector parameters . . . . .	18
2.2	Resolutions . . . . .	28
3.1	Properties of several gases used in proportional counters . . . . .	37
3.2	Diffusion coefficients for ions . . . . .	39
4.1	Sense wire surface charge and field . . . . .	57
4.2	Wire surface charge with the cover shifted by 1 mm . . . . .	62
4.3	Dead zones . . . . .	73
5.1	CIZ parameters . . . . .	82
6.1	Potentials in the CIZ cell . . . . .	87
6.2	Properties of the CIZ line drivers . . . . .	90
6.3	Properties of the H1 drift chamber amplifier . . . . .	92
7.1	Correlation wire to byte . . . . .	98
7.2	Properties of the FADC units . . . . .	99

# 1 General introduction to ep-physics

## 1.1 Motivation

The drift chamber described in this thesis is one of the innermost parts installed within the H1 experimental setup. The H1 detector was built around one of two interaction regions of the first ever constructed electron-proton storage ring — HERA at the DESY Laboratory in Hamburg, Germany. At the interaction point 26.7 GeV electrons collide with 820 GeV protons resulting in a center of mass energy of  $s^{1/2} = (4E_e E_p)^{1/2} = 292$  GeV. The accelerator parameters are summarized in Table 1.1. The HERA program

	Design		Autumn 1992		unit
	<i>p</i> -ring	<i>e</i> -ring	<i>p</i> -ring	<i>e</i> -ring	
Energy	820	30	820	26.7	GeV
Luminosity	$1.5 \times 10^{31}$		$3.0 \times 10^{29}$		$\text{cm}^{-2}\text{s}^{-1}$
Integrated luminosity	$10^5$		32		$\text{nb}^{-1}/\text{y}$
Interaction points	4		2		
Magnetic field	4.68	0.165	4.68	0.149	T
Number of particles	210	80	2.6	3.7	$10^{11}$
Current per bunch	760	290	200	280	$\mu\text{A}$
Number of bunches	210	210	10	10	
Bunch separation	96	96	96	96	ns
Injection energy	40	14	40	12	GeV
Filling time	20	15	120	30	min
$\sigma_x/\sigma_y$ at interaction point	0.29/0.07	0.26/0.02	0.36/0.10	0.30/0.07	mm
$\sigma_z$ at interaction point	110	8	$\approx 200$	$\approx 10$	mm
Energy loss per turn	$6.2 \times 10^{-6}$	127			MeV
RF-frequency	52.03/208.1	499.8	52.03	499.8	MHz

Table 1.1: Summary of HERA parameters (taken from references [1, 2]).

extends the classical scattering experiments which played a crucial role in understanding the fundamental forces of nature to a higher energy domain. Previous lepton scattering experiments led to the development of the standard model of the electroweak and the strong interaction of quarks, gluons and leptons. Compared to fixed target experiments HERA provides an increase by an order of magnitude in resolving power. The values of  $Q^2$  can reach  $4 \times 10^4 \text{ GeV}^2$ , at least two orders of magnitude more than ever before. The spatial resolution  $\Delta$  by which the electron probes the structure of the nucleon is given by the four-momentum transfer  $Q$  of the incoming and outgoing lepton using the Heisenberg uncertainty relation  $\Delta \approx \hbar/Q$ . New particles may be generated up to the center of mass energy. At high  $Q$  the contributions from the weak interaction are comparable or even higher than those from the electromagnetic interaction. At low  $Q$  processes induced by quasireal photons dominate the cross sections. Total cross sections up to 200 GeV center of mass energy can be measured and heavy quark-antiquark-pairs are produced with high probability.

## 1.2 Deep inelastic scattering

On a microscopic level HERA is in reality an electron quark or an electron gluon collider. Both quarks and gluons are found in the proton. The constituents which do not participate in the collision are called proton remnants and lead to hadronic activity which normally escapes near the initial proton direction through the beam pipe hole in the detector. The electron quark interaction is either mediated by the exchange of a virtual photon ( $\gamma$ ) or virtual vector boson ( $Z^0$ ) (Figure 1.1.a) in the neutral current processes or by a charged vector boson ( $W^-$ ) in the charged current process (Figure 1.1.b). A photon radiated by the electron may also fuse with a gluon creating a quark-antiquark pair (Figure 1.1.c). The most relevant kinematical quantities in the deep elastic scattering process are the

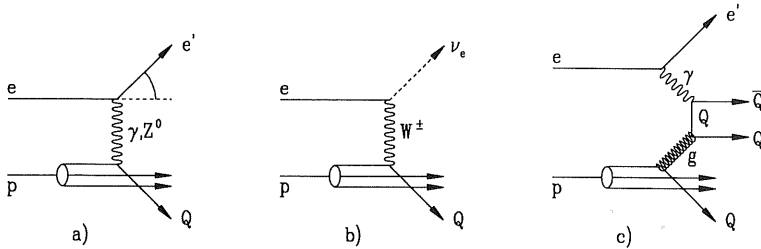


Figure 1.1: Feynman diagrams for the basic processes studied at HERA (from ref. [3]).

square of the four-momentum transfer  $Q^2$ , the fraction of the proton four-momentum  $p$  carried by the struck parton (quark  $q$  or gluon  $g$ )  $x$  and the energy loss of the electron measured in the proton rest frame. Often  $x$  is called the Bjorken scaling variable, while  $Q^2$  and  $\nu$  may also be interpreted as the mass squared and the energy of the current  $\gamma, W^-, Z^0$ . These variables (instead of  $\nu$  the dimensionless variable  $y$  is used) are given in terms of the energies of the incoming electron  $E_e$ , the scattered electron  $E'_e$ , the incoming proton  $E_p$ , the hadronic recoil jet  $E_h$  and the corresponding polar angles  $\theta_e$  and  $\theta_h$ , both measured relative to the proton direction ( $\theta = 0$ , positive  $z$ -direction).

In the basic diagram shown in Figure 1.2  $\ell, \ell'$  and  $P$  are the four-momentum vectors of the incoming lepton, the outgoing lepton and the incoming proton respectively.  $P_H$  is the four-momentum of the total outgoing hadronic system. Neglecting the lepton and the proton masses with respect to the energies in the laboratory frame and the positive  $z$ -axis along the proton beam direction we can write

$$\ell = \begin{pmatrix} E_e \\ 0 \\ 0 \\ -E_e \end{pmatrix} \quad \ell' = \begin{pmatrix} E'_e \\ E'_e \sin \theta_e \\ 0 \\ E'_e \cos \theta_e \end{pmatrix} \quad P = \begin{pmatrix} E_p \\ 0 \\ 0 \\ E_p \end{pmatrix} \quad P_H = \sum_{h_i} \begin{pmatrix} E_{h_i} \\ P_{x_{h_i}} \\ P_{y_{h_i}} \\ P_{z_{h_i}} \end{pmatrix}$$

In terms of these four-momentum vectors  $Q^2, x, y$  are then defined as

$$\begin{aligned} Q^2 &= -(\ell - \ell')^2 = -q^2 \\ x &= \frac{Q^2}{2P \cdot q} \\ y &= \frac{P \cdot q}{P \cdot \ell} \end{aligned}$$

With the center of mass energy squared  $s = 4E_e E_p$  one obtains the usual relation between  $Q^2, x$  and  $y$

$$Q^2 = sxy$$

with  $Q_{\max}^2 = s = 4E_e E_p$  and  $y = \nu/\nu_{\max}$  with  $\nu_{\max} = s/2m_p$ . For charged current events

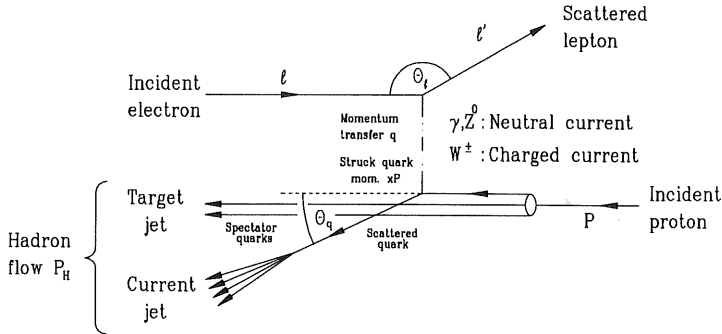


Figure 1.2: Basic diagram for deep inelastic scattering.

the kinematics can only be reconstructed from the hadrons, since the outgoing lepton is a neutrino. In neutral current events the kinematics can be reconstructed either by using the scattered electron, the hadron flow or both. When the electron is measured  $Q^2, x$  and  $y$  can be expressed in terms of the scattered lepton energy  $E'_e$  and the angle  $\theta$  in the laboratory frame as

$$\begin{aligned} Q^2 &= 4E_e E'_e \cos^2 \frac{\theta_e}{2} & x &= \frac{Q^2}{4E_e E_p y} = \frac{E_e E'_e \cos^2 \frac{\theta_e}{2}}{E_p (E_e - E'_e \sin^2 \frac{\theta_e}{2})} \\ y &\equiv y_e = 1 - \frac{E'_e}{E_e} \sin^2 \frac{\theta_e}{2} \end{aligned}$$

Figure 1.3 shows some contours of constant  $\theta_e$  and  $E'_e$  in the  $x, Q^2$  plane. Pre-HERA experiments were limited to a triangle in the upper left hand corner of Figure 1.3. (see also Figure 1.5). The influence of finite electron angular and energy resolution can be shown by taking the partial derivatives of the above expressions giving the uncertainties

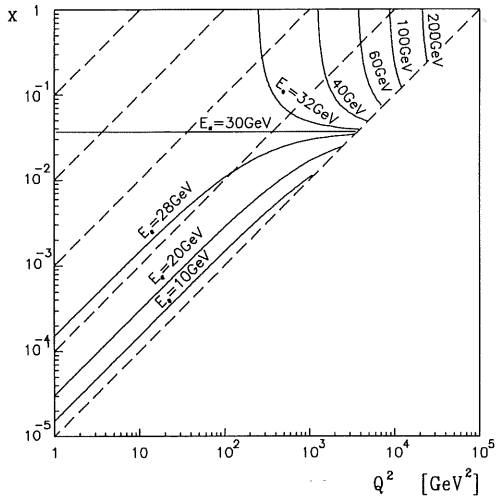
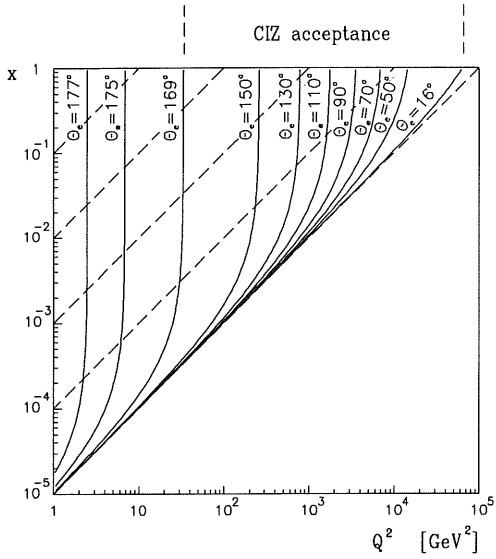


Figure 1.3: a) Lines of constant scattered electron angle to the proton direction. b) Lines of constant scattered electron energy.

$\Delta$  for  $x$  and  $Q^2$  to

$$\frac{\Delta Q^2}{Q^2} = \frac{\Delta E'_e}{E'_e} \quad \frac{\Delta Q^2}{Q^2} = -\tan \frac{\theta_e}{2} \Delta \theta_e$$



$$\frac{\Delta x}{x} = \frac{1}{y} \frac{\Delta E'_e}{E'_e} \quad \frac{\Delta x}{x} = \tan \frac{\theta_e}{2} \left( x \frac{E_p}{E_e} - 1 \right) \Delta \theta_e .$$

The resolution of  $Q^2$  is determined by the electron energy resolution except for very small scattering angles ( $\theta_e \approx 180$ ), where the angular resolution becomes the dominant term. The electron is then mostly scattered into the backward electromagnetic calorimeter and its angle is given by the vertex and hits in the tracking chambers (see chapter 2). Therefore the resolution and efficiencies of the latter chambers will be important. The angular term only influences the  $x$  resolution for large  $x$  and small  $Q^2$ . At low  $y$  the  $x$  resolution is poor, because of the factor  $y^{-1}$  in the corresponding derivative, in particular if an electromagnetic sampling calorimeter is used. These results are illustrated in Figure 1.3 using the actual design values of the H1 detector. Note, that one must consider also the effects of migration and systematic errors [4, 5] before one can translate such results into a contour plot in the  $x, Q^2$  plane such as shown in Figure 1.5 indicating where a reliable structure function measurement is possible. In charged current events  $x$  and  $Q^2$  can be determined only using the outgoing hadronic flow, as proposed by [6] A. Blondel and F. Jacquet. From energy-momentum conservation it is straightforward to express  $y$  and  $Q^2$  as a function of the laboratory variables of the outgoing hadrons. The following relations can be derived

$$Q^2 = \frac{E_h^2 \sin^2 \theta_h}{1 - y_h} = \frac{(\sum_{h_i} p_{th_i})^2}{1 - y_h} = \frac{P_t^2}{1 - y_h}$$

$$y \equiv y_h = \sum_{hadrons, h_i} \frac{E_{h_i} - p_{z, h_i}}{2E_e}$$

where  $E_h, p_{zh}$  and  $p_{th}$  are the energy, longitudinal momentum and transverse momentum of the hadron  $h$  respectively.  $P_t$  is the total transverse momentum of the outgoing hadronic flow. It is the total hadronic flow, that enters in the above expressions and so no assumption about the internal structure of the proton needs to be made either. Hadrons emitted in the forward direction do not contribute to  $Q^2$  and  $y_h$ , therefore the unavoidable dead areas in forward direction along the beam pipe have only minor influence. The reconstruction errors depend mainly on the size of the beam hole, the errors on the angle and the energies of the outgoing hadrons. Lines of constant current jet energies and constant jet angles are drawn in Figure 1.4. At small  $x$  the jet energies are small. Remembering that  $x$  is the fraction of proton momentum carried by the struck parton it is obvious, that the current jet is emitted more and more in the forward direction, as  $x$  rises. The sensitivity to the angular and the energy resolution can be seen in taking the following partial derivatives, where  $E_J$  is the energy and  $\theta_J$  the polar angle of the current jet

$$\frac{\Delta Q^2}{Q^2} = \frac{(2-y) \Delta E_J}{(1-y) E_J} \quad \frac{\Delta Q^2}{Q^2} = (2 \cot \theta_J + \frac{y}{1-y} \cot \frac{\theta_J}{2}) \Delta \theta_J$$

$$\frac{\Delta x}{x} = \frac{1}{1-y} \frac{\Delta E_J}{E_J} \quad \frac{\Delta x}{x} = (-2 \cot \theta_J + \frac{1-2y}{1-y} \cot \frac{\theta_J}{2}) \Delta \theta_J$$

The resolution in the forward direction is very poor due to the  $\cot \theta_J/2$  and  $\cot \theta_J$  terms and because of the loss in the beam pipe. The measurement of charged current events will

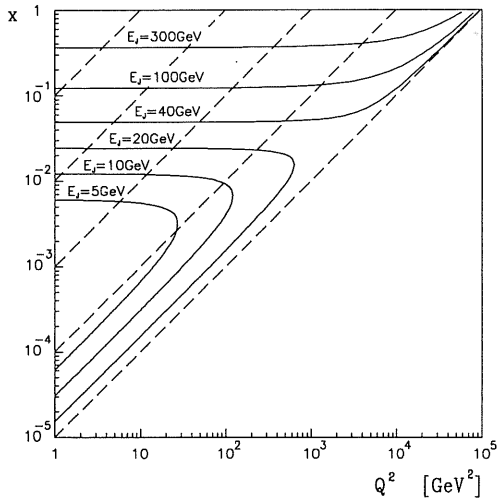
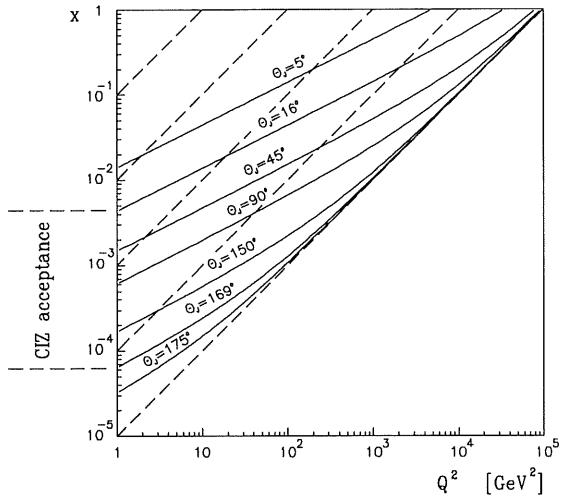


Figure 1.4: a) Lines of constant current jet angle to the proton direction in the laboratory frame. b) Lines of constant current jet energy.

then be restricted to events with a current jet angle  $\theta_J$  above 10 degrees. The resolution on  $Q^2$  and  $x$  is poor at large  $y$  or at low jet energy. Requiring a good resolution on

the measurement of  $Q^2$  and  $x$  excludes therefore the region at large  $y$  and small  $x$ . The question of which variable to use to best determine the kinematics at the parton level within the limits set by the experimental resolution and the influence of the radiative corrections has been extensively studied within the H1 collaboration (see [7, 8]). In some areas the electron variables suffice, as in all fixed target experiments, in some areas hadron variables are to be preferred. Lastly there are areas of overlap where a cross-check is possible or a combination of electrons and hadrons is optimal. An example is the double-angle method utilizing the angle  $\theta_e$  of the electron and  $\theta_h$  the angle of the hadron-jet. The domains in the  $x, Q^2$  plane accessible by the different methods of kinematical reconstruction are illustrated in Figure 1.5.

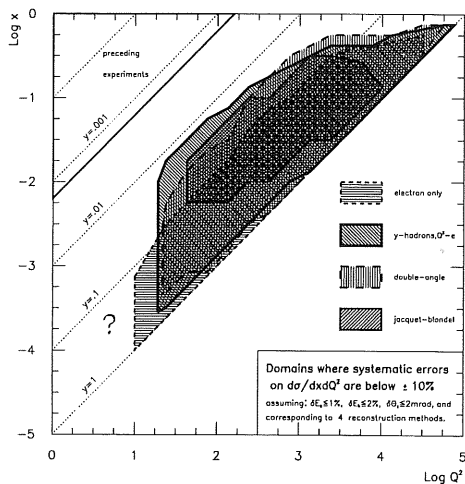


Figure 1.5: Domains in the  $x, Q^2$  plane, where the systematic errors on  $d^2\sigma/(dx dQ^2)$  are below 10%. The dotted lines correspond to constant  $y$ . The different shadings indicate the method of kinematical reconstruction used (from reference [9]). The area in the upper left corner corresponds to the range accessible to previous experiments.

### 1.3 Hard scattering of almost real photons

In most of the interactions at HERA, the scattered electron is emitted at very low angle, the squared momentum transfer  $Q^2$  is almost zero. This gives a unique opportunity to study high energy collisions of almost real photons with protons. A first measurement of the total photoproduction ( $\gamma p$ ) cross section  $\sigma_{\gamma p}^{tot}$  has already been published by both

experiments H1 and Zeus. Observation of prompt photons is a source of information on both the proton structure and the anomalous photon structure. A detailed account of all aspects of HERA physics can be found in [7, 8]. To give an example from low  $Q^2$

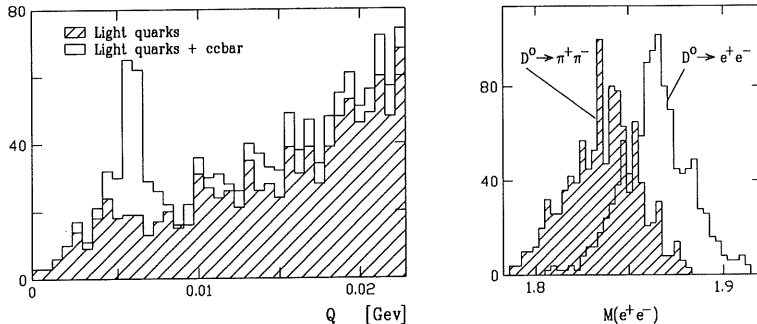


Figure 1.6: Left:  $D^*$  tagging signal in the distribution of mass excess  $\Delta M \equiv Q$  (see text for definition) for  $c\bar{c}$  events produced in  $\gamma g$  fusion superimposed on combinatorial background from light quark production. Right:  $D^0$  mass resolution for the decay into  $e^+e^-$  (similar for  $K^-\pi^+$ ,  $\mu^+\mu^-$  and  $\pi^-\pi^+$ ), the shaded histogram gives the result if the  $e$  mass is assumed for the  $\pi^+\pi^-$  channel. Results from a reconstruction of Monte Carlo simulated data.

photoproduction and to illustrate the need for high quality tracking, we discuss briefly  $D^{*\pm}$  tagging of charmed events [10]. The tagging exploits the fact, that in the decay chain  $D^{*+} \rightarrow D^0\pi^+$  with e. g.  $D^0 \rightarrow K^-\pi^+$  the  $\pi^+$  from  $D^{*+}$  decay is nearly at rest in the  $D^*$  center of mass system (the mass excess is only 6 MeV). Hence the  $K^-$  and  $\pi^+$  candidate tracks with an invariant mass  $M_D^{inv}$  near  $M(D^0)$  can be combined with a usually low momentum  $\pi^+$  candidate to form a  $D^*$  candidate. Due to the special kinematic conditions one achieves a higher mass resolution in the variable

$$\Delta M = M_D^{inv}((K^-\pi^+)\pi^+) - M_D^{inv}(K^-\pi^+)$$

than in the mass  $M_D^{inv}$  itself. This is illustrated in figure 1.6, where the expected signal is superimposed on a combinatorial background from light quark photoproduction. With the tracking system of H1 one actually obtains a mass resolution of 20 MeV at the  $D^0$  mass. Since the  $D$  meson momentum is sufficiently well correlated with the charmed quark produced in  $\gamma$  gluon fusion, the gluon momentum can be reconstructed knowing  $y_h$  and the gluon density within the proton be measured. If forbidden decays such as  $D^0 \rightarrow \mu^+\mu^-$  or  $e^+e^-$  are to be studied it is important to have good muon identification, and good electron identification at momenta near 1 GeV/c, because the  $D$  meson spectrum peaks at rather low energies in particular in the midrapidity region, where these low multiplicity events can be reconstructed.

## 2 Charged particles within the H1 detector

### 2.1 General description of the H1 detector

A detailed description of the H1 detector is given in [11]. In order to carry out the physics program which was outlined in the previous section prime attention has to be given to the clean identification of electrons and to their energy measurement. Therefore a large coil is used, which contains the electromagnetic and the hadronic calorimeter. With this choice the amount of dead material in front of the calorimeter and its total weight are minimized. Choosing a liquid Argon calorimeter we further benefit from the proven stability of this technique, the ease of its calibration and the fine granularity, which allows to separate electrons from pions to a high degree. Lastly the homogeneity of the response and overall hermiticity are helpful for energy flow measurements as well as neutrino detection for charged current events. Supplementing the calorimeter by high resolution tracking on the inside and an instrumented iron yoke on the outside is crucial for the identification of high-density particle jets characterizing the hadronic final states in deep inelastic scattering events as well as for muon detection. Identifying muons is particularly important for some exotic channels and for photoproduced low multiplicity heavy flavour events. In these design aspects the H1 detector does not differ strongly from the detectors at  $e^+e^-$  colliders, or  $p\bar{p}$  colliders built in the past. Different at HERA is however the imbalance in the energy of the two colliding beams, which requires an asymmetric detector. Different also is the microstructure of the two beams, which leads to short intervals ( $\approx 100$  ns) between two subsequent bunch crossings, and also the high background level, as proton induced background arises from beam line vacuum conditions, usually met with electron accelerators and which are worse than for pure proton accelerators.

Since the centre of mass for HERA collisions is boosted along the proton direction with  $\gamma_{cm} = 2.86$  the H1 detector is considerably more massive and higher instrumented in this direction. This is apparent from Figure 2.1, which shows a perspective view and cut along the beam axis. The cut perpendicular to the axis in Figure 2.2 shows that the different shells of the H1 detector are at least symmetric in azimuth. In the following we often refer to the direction of the exiting electron (incoming proton) as the backward direction (negative  $z$ -values relative to the center of the interaction region and  $\theta = \pi$ ), and vice versa to that of the exiting proton as the forward direction (positive  $z$  and  $\theta = 0$ ). Starting the description from the center of the interaction region the detector consists of a central and a forward tracking system, each containing different layers of drift chambers and trigger proportional chambers. The liquid argon cryostat surrounds the trackers. It houses the lead absorber plates and readout gaps of the electromagnetic section, which are followed by the steel plates of the hadronic section with their readout gaps. A superconducting and cylindrical coil with a diameter of 6 m and a length of 5.75 m provides the analysing field of 1.15 T. The iron return yoke of the magnet is laminated and filled with limited streamer tubes. The small fraction of hadronic energy leaking out of the back of the calorimeter is registered here and muon tracks are found. Muon

Calorimetry		
Main calorimeter: liquid Ar	Electromagnetic part	Hadronic part
Granularity	10 to 100 cm <sup>2</sup>	50 to 2000 cm <sup>2</sup>
Depth (number of channels)	20 to 30 X <sub>0</sub> (30784)	4.7 to 7 λ <sub>abs</sub> (13568)
Resolution σ(E <sub>e,h</sub> )/E <sub>e,h</sub>	12%/√E <sub>e</sub> ⊕ 1%	≈ 50%/√E <sub>h</sub> ⊕ 2%
LAr purity (stability of el. calibration)	≤ 0.2% over one year (one month)	
Noise per channel	10 to 30 MeV	
Angular coverage – dead channels	4° < θ < 153°	< 0.3%
Backward calorimeter: Pb–scintillator		
Angular coverage – granularity	151° < θ < 177°	16 × 16 cm <sup>2</sup>
Depth – resolution σ(E <sub>h</sub> )/E <sub>e</sub>	22.5 X <sub>0</sub> (1 λ <sub>abs</sub> )	10%/√E <sub>e</sub> ⊕ 2 [1]%
Tail catcher: iron–streamer tubes		
Angular coverage	4° < θ < 177°	
Depth – resolution σ(E <sub>h</sub> )/E <sub>h</sub>	4.5 λ <sub>abs</sub>	100%/√E <sub>h</sub>
Plug calorimeter: Cu–Si		
Angular coverage – granularity	0.7° < θ < 3.3°	5 × 5 cm <sup>2</sup>
Depth – resolution σ(E <sub>h</sub> )/E <sub>h</sub>	4.25 λ (44.6 X <sub>0</sub> )	≈ 150%/√E <sub>h</sub>
Electron tagger: Tl(Cl/Br)		
Angular coverage – granularity	θ > 179.7°	2.2 × 2.2 cm <sup>2</sup>
Depth – resolution σ(E <sub>e</sub> )/E <sub>e</sub>	21 X <sub>0</sub>	≈ 10%/√E <sub>e</sub> ⊕ 1%
Tracking		
Coil: radius – field	3 m – B = 1.15 T, ΔB/B ≤ 2%	
Central tracking		
Angular – radial coverage	25° < θ < 155°	150 < r < 850 mm
Jet chamber: spatial resolution	σ <sub>r,φ</sub> = 170 μm	σ <sub>z</sub> = 22.0 mm
z-chambers: spatial resolution	σ <sub>r,φ</sub> = 25 and 58 mm	σ <sub>z</sub> ≈ 350 μm
Momentum – dE/dx resolution	σ <sub>p</sub> /p <sup>2</sup> < 0.01 [0.003] GeV <sup>-1</sup>	σ(dE)/dE = 10 [6]%
Forward/backward tracking		
Angular – radial coverage (f)	7° < θ < 25°	120 < r < 800 mm
Spatial resolution (f)	σ <sub>r,φ</sub> = 170 μm (σ <sub>r</sub> = 29 mm)	σ <sub>x,y</sub> = 210 μm
Angular coverage – resolution (b)	155° < θ < 175°	σ <sub>x,y</sub> = 1 mm
Trigger proportional chambers		
Angular coverage – channels	7° < θ < 175°	3936
Muon detection		
Instrumented iron		
Angular coverage – total area	4° < θ < 171°	4000 m <sup>2</sup>
Number of channels	wires: 103700, strips: 28700, pads: 4000	
Spatial resolution	σ <sub>wire</sub> = 3 – 4 mm	σ <sub>strip</sub> = 10 – 15 mm
Angular – momentum resolution barrel	σ <sub>θ</sub> (σ <sub>φ</sub> ) = 15(10) mr	[σ <sub>p</sub> /p ≈ 0.35]
Forward muon toroid		
Angular coverage – resolution	3° < θ < 17°	[0.25 < σ <sub>p</sub> /p < 0.32]
Overall size (x, y, z) – weight	12 × 15 × 10 m <sup>3</sup>	2800 t

Table 2.1: Summary of H1 detector parameters.

The actual status after the first running phase of HERA in 1992 has been given. Alternatively design and test beam figures have been given in brackets []. Energies are given in GeV.

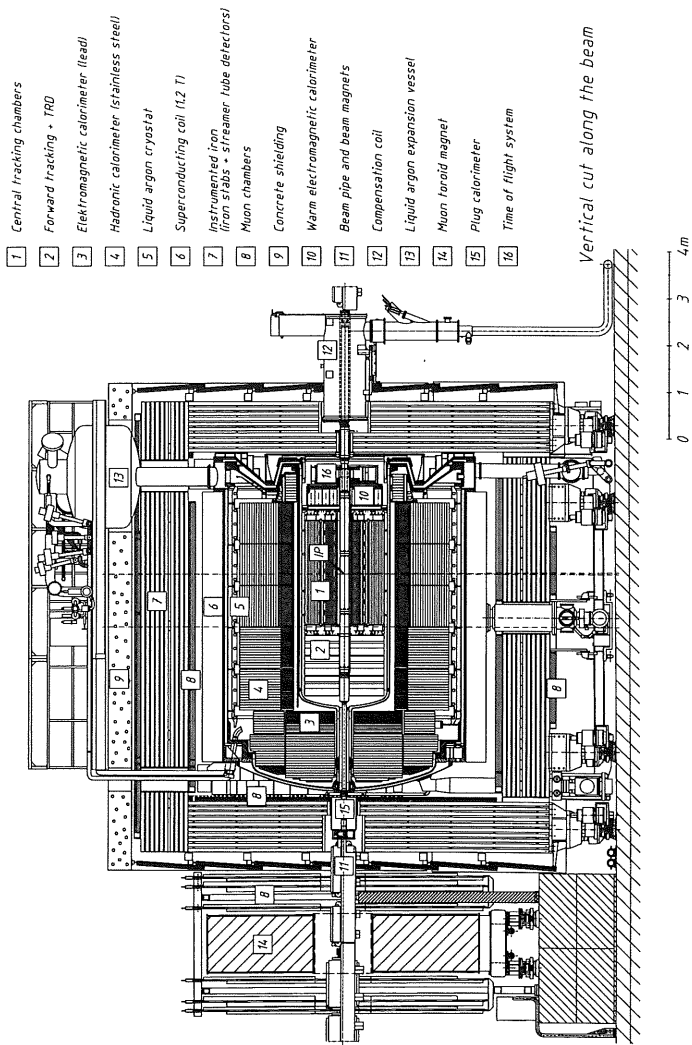


Figure 2.1: Longitudinal cut through the H1 detector along the beam line.

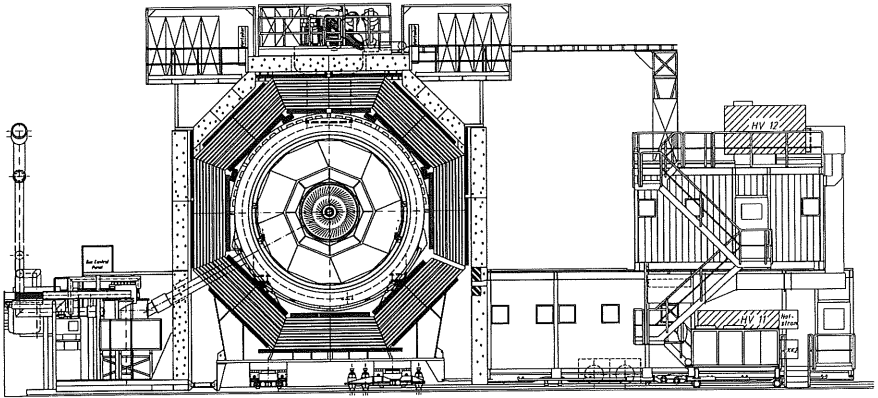


Figure 2.2: Transverse cut through the H1 detector at the center of the interaction region.

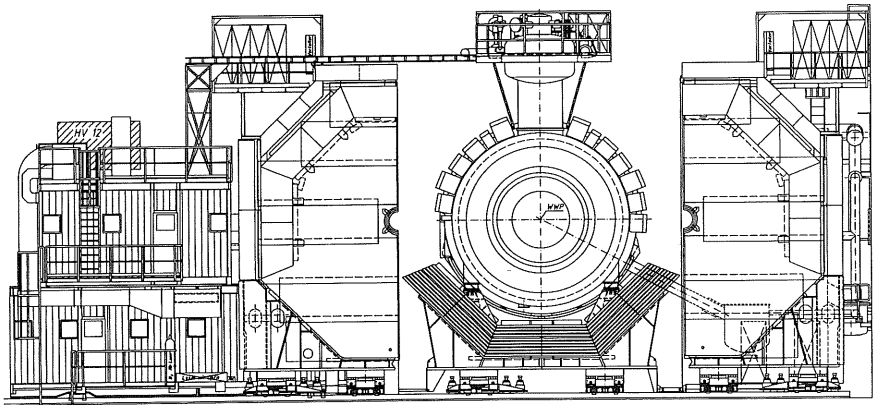


Figure 2.3: Front view of the H1 detector with the iron yoke opened]Front view of the H1 detector with the southern and the northern shells of the iron yoke opened.



identification further benefits from additional chambers inside and outside of the iron. The very stiff muon tracks in forward direction are analysed in a supplementary toroidal magnet sandwiched between drift chambers. The remaining holes in the liquid argon calorimeter are closed with warm calorimeters, a Si-Cu plug at very forward angles, a Pb-scintillator calorimeter backed by a tail catcher (part of the muon system) in backward direction and lastly an electron tagger at  $z = -33$  m from the interaction point not shown in Figure 2.1. The tagger marks the energy of an electron with very small scattering angle inducing a photoproduction event and, taken in coincidence with a corresponding photon detector at  $z = -103$  m upstream from the interaction point, monitors the luminosity by the bremsstrahlung process. Two scintillator walls in backward direction are installed to recognize background produced by the proton beam upstream of the H1 detector. A survey of detector parameters is given in Table 2.1.

## 2.2 Synchrotron radiation shielding

The HERA  $e^-$  beam is accompanied by a strong flux of synchrotron radiation photons which are produced in the last bending magnet before the interaction point and the interaction quadrupoles. Synchrotron radiation from the arcs is absorbed before the H1 detector and need not be considered.

At a beam energy of 30 GeV and a stored current of 60 mA we expect a flux of  $10^{18}$  photons per second with an energy above 5 keV into the interaction region. This flux represents a radiated power of 3.6 kW. The critical energy is 42.4 keV. In order to protect the detector elements a system of masks inside the beam pipe is installed. The design criteria for the synchrotron radiation absorbers were such that only photons which have undergone at least two scatters can reach the central detector region. In order to reduce the photon flux the aperture of the collimators should be as small as possible. The width is thus determined by the requirement for sufficient aperture at injection. Masks which are hit by synchrotron radiation are sources of secondary photons. Therefore the albedo of all surfaces has been reduced by coating the tungsten absorbers with 0.5 mm silver and 0.2 mm copper. For 100 keV photons the albedo is reduced from 10% for pure tungsten to 1% with the appropriate coating. The geometry of the absorbers is shown in Figure 2.4. The collimators  $C_1$ ,  $C_2$  and  $C_3$  are hit by direct synchrotron light and have to stand a radiated power of about 1 kW each. These collimators are movable and water cooled. The synchrotron radiation, missing  $C_3$ , is passed through the detector area and hits an absorber 24 m behind the interaction point. The collimators  $C_4$ , and  $C_5$  have a fixed horizontal aperture of +30 mm -25 mm and  $\pm 50$  mm, respectively. They protect the detector elements against secondary photons originating from edge scattering at the collimators  $C_1 - C_3$  and backscattered photons from the absorber at 24 m. The collimator  $C_6$  is movable and provides an additional shield against photons from 24 m downstream. The aperture can be set between 65 mm and 25 mm with respect to the beam. The principle of shielding the interaction region is shown in Figure 2.4. The present arrangement of synchrotron radiation masks cuts down the number of photons which enter

the central part of the detector to a level of  $10^6$  photons per second with an energy above 20 keV. Thus at nominal beam conditions we expect about  $10^{-1}$  spurious synchrotron hits in the central tracking chamber per bunch crossing. The observations during the first runs in 1992 are consistent with the above estimates. Due to the low currents and the

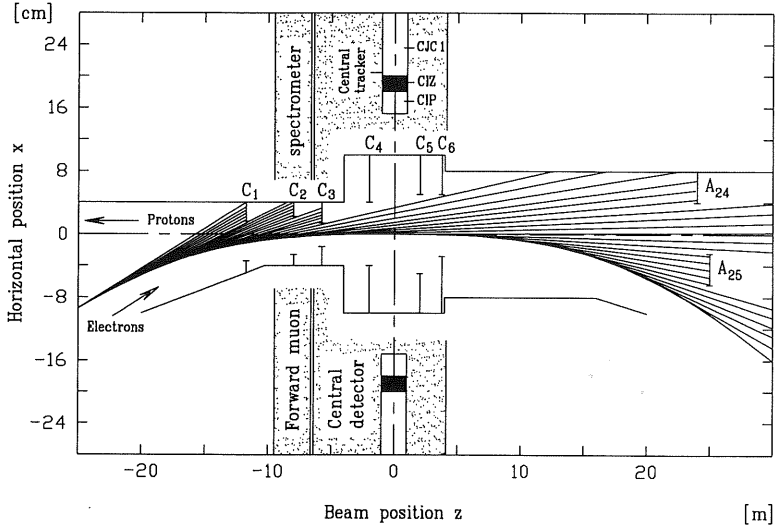


Figure 2.4: Arrangement of the synchrotron masks shielding the H1 detector from direct synchrotron radiation.

reduced electron energy of 27 GeV we did not observe synchrotron radiation hits in the tracking chambers.

### 2.3 The H1 tracking system in the central region

The tracking system of H1 provides simultaneous track triggering, reconstruction and particle identification for the event topology particular to HERA electron proton collisions. It has been designed to reconstruct jets with high particle densities and to measure the momentum and angles of scattered isolated charged particles to a precision of  $\sigma_p/p^2 \approx 3 \times 10^{-3} \text{ GeV}^{-1}$  and  $\sigma_\theta \approx 1 \text{ mr}$ .

Because of the asymmetry between the electron and proton beam energies many charged particles are produced at small angles  $\theta$  to the incident proton (forward) direction. To maintain good efficiency for triggering and reconstruction over the whole

solid angle, we divide the tracking system between the central and forward regions (see Figure 2.5). Two mechanically distinct tracking detectors have been constructed, the central (CTD) and forward (FTD) trackers, respectively. Each is optimised for tracking and triggering in its angular region.

Track reconstruction in the central region (see Figure 2.6) is based on two large concentric drift chambers, CJC1 and CJC2. The chambers have wires strung parallel to the beam axes ( $z$ -direction) with the drift cells inclined with respect to the radial direction. The measured space point resolution is  $170 \mu\text{m}$  in the drift coordinate ( $r\phi$  plane) and, by comparing signals read out at both wire ends, one percent of the wire length in  $z$ . From the signals recorded in these chambers the transverse track momentum is determined and in addition the specific energy loss  $dE/dx$  is used to improve particle identification.

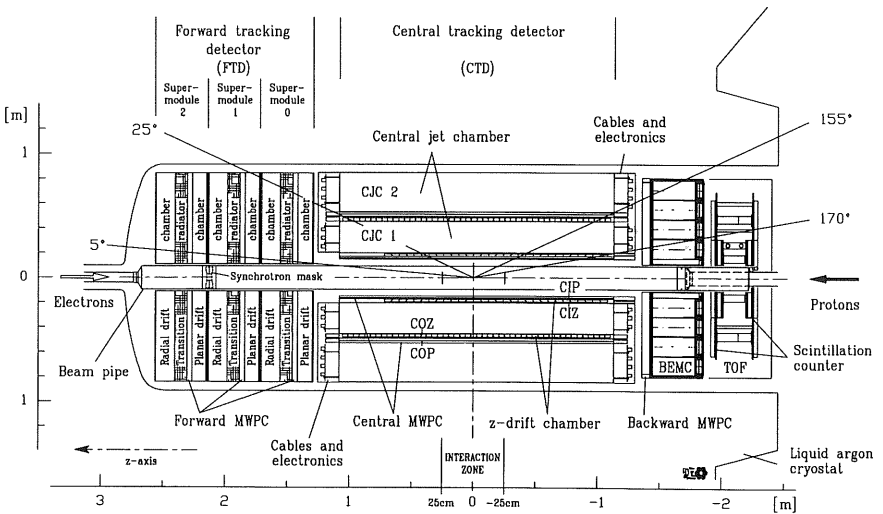


Figure 2.5: The H1 tracking system ( $rz$  view).

Two thin drift chambers, the central inner (CIZ), described in this thesis and the central outer (COZ)  $z$ -chambers complement the measurement of charged track momenta in the central chambers. The CIZ chamber fits inside CJC1, and the COZ chamber fits in between CJC1 and CJC2. These two chambers deliver track elements with typically  $300 \mu\text{m}$  resolution in  $z$  and 1 to 2% of  $2\pi$  in  $\phi$ . This requires a drift direction parallel to, and sense wires perpendicular to the beam axis.

Triggering over the full solid angle is based on multiwire proportional chambers with pad readout in the central and forward region and wire readout in the backward direction. They provide a fast first level (L1) trigger decision which can be used to distinguish

between successive beam crossings. In addition, in the central and forward region, combinations of pads hit in the central inner proportional chamber (CIP), the central outer proportional chamber (COP) and the forward proportional chambers (FWPC) are used to trigger on tracks coming from a nominal interaction vertex.

Each of the central chambers has an independent gas volume and separate electrostatic shielding. They were built and tested separately, and then assembled and locked to one mechanical unit. The detector walls are thin to reduce photon conversion, and in particular its effect on identification of primary electrons. Neighbouring volumes share a thin (1.5 mm) cylinder of carbon fibre reinforced epoxy with a 50  $\mu\text{m}$  aluminium coating on each side. The complete system of central tracking detectors is housed in a single aluminium cylinder of 4 mm wall thickness. The assembly also provides a precise alignment of the chambers relative to the outside support.

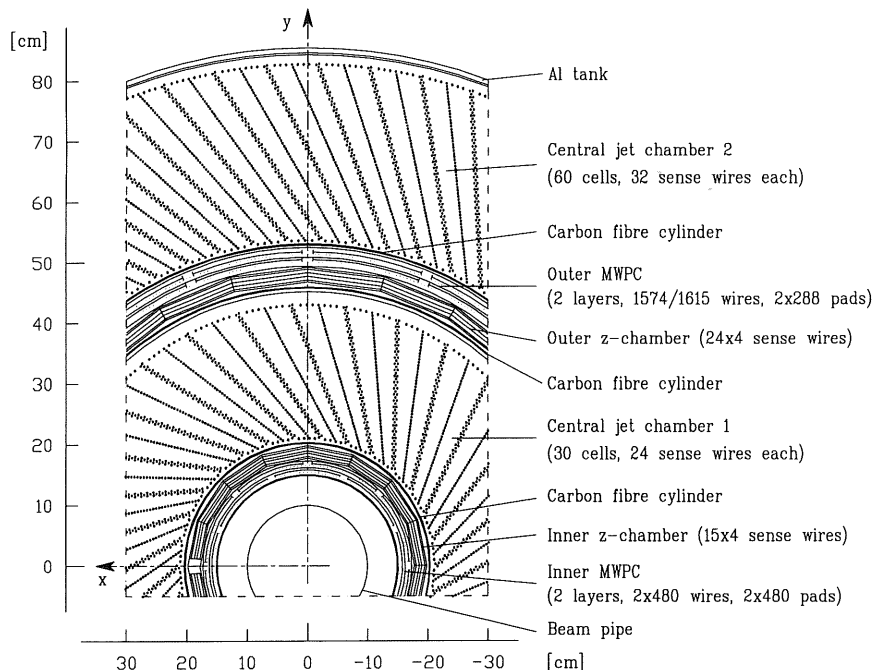


Figure 2.6: Central tracking system, section perpendicular to the beam.

Charged tracks produced at polar angles  $\theta$  close to the beam axis (forward  $\theta < 30^\circ$ , backward  $\theta > 150^\circ$ ) no longer traverse the full bending ( $r\phi$ ) plane radius of the solenoid

magnetic field. Consequently in the CTD both track pattern recognition and track accuracy of reconstruction deteriorate as the measured track length and the number of precision space points decrease. A way of rectifying this loss is to compensate for the reductions in track length and the number of points in the central region by means of a higher radial density of accurate space points obtained using wires strung in the bending plane closely spaced in  $z$ . This is provided by the forward tracking detector which consists of an integrated assembly of three nearly identical supermodules as also illustrated in Figures 2.5. Each supermodule includes, in increasing  $z$ : three different orientations of planar wire drift chambers designed to provide accurate  $\theta$  measurements, a multiwire proportional chamber (FWPC) for fast triggering, a passive transition radiator and a radial wire drift chamber which provides accurate  $r\phi$  (drift coordinate) information, moderate radius measurement by charge division and limited particle identification by measuring the transition radiation produced immediately upstream. The FTD and CTD are linked together, aligned and surveyed prior to installation into the calorimeter cryostat.

## 2.4 Momentum measurement

In the constant magnetic field  $B$  of the central tracking region the trajectory of a particle with the momentum  $p$  and the charge  $ze$  is a helix with the radius of curvature  $r$  and the pitch angle  $\lambda$ . The curvature is determined by the jet chambers which measure the space points of the tracks in the  $r\phi$  plane. The radius is then related to the transversal momentum by

$$p_T = 0.3 \cdot z \cdot B \cdot r$$

where  $B$  is in Tesla,  $r$  in m and  $p_T$  in  $GeV/c$ . The total momentum of the track is then the sum of both components the transversal and the longitudinal momentum. The latter is given by the pitch angle  $\lambda$  or more convenient by the polar angle  $\theta$ . Hence the square of the momentum can be written as

$$p^2 = p_T^2 + p_L^2 = p_T^2(1 + \cot^2 \theta) = p_T^2 / \sin^2 \theta .$$

The polar angle  $\theta$  is determined by the measurement of the  $z$  coordinates of the track at different radii in the  $rz$  plane. This is done also in the jet chambers by using the charge division method, but the more precise  $z$  coordinate and consequently more accurate  $\theta$  is provided by the  $z$ -chambers.

### 2.4.1 Momentum resolution and spatial resolution in $z$

The momentum resolution in the central tracking region is determined by the spatial resolution in  $r\phi$  (curvature radius  $r$ ) of the jet chambers and the resolution in  $z$  given by

the  $z$ -chambers in combination with the jet chambers. In taking the partial derivatives the momentum resolution can be written as

$$\Delta p = \sqrt{\frac{1}{\sin^2 \theta} \Delta p_T^2 + \frac{p_T^2 \cos^2 \theta}{\sin^4 \theta} \Delta \theta^2}$$

or

$$\begin{aligned} \frac{\Delta p}{p} &= \sqrt{\frac{1}{p^2 \sin^2 \theta} \Delta p_T^2 + \frac{p_T^2 \cos^2 \theta}{p^2 \sin^4 \theta} \Delta \theta^2} \\ &= \sqrt{\frac{\Delta p_T^2}{p_T^2} + \frac{\cos^2 \theta}{\sin^2 \theta} \Delta \theta^2}. \end{aligned}$$

The first term  $\Delta p_T/p_T$  is determined by the single wire resolution  $\Delta_{r\phi}$  of the jet chambers. Following [12] the error of the curvature  $\kappa = 1/r$ , if many ( $N \geq 10$ ) uniformly spaced points are measured, can be written as

$$\Delta \kappa_{res} = \frac{\Delta_{r\phi}}{L'^2} \sqrt{\frac{720}{N+5}}$$

And the transverse momentum resolution becomes ( $L'$  is the projected length of the track onto the  $r\phi$  plane and  $\Delta_{r\phi}$  the measurement error for each point)

$$\frac{\Delta p_T}{p_{T,es}} = \frac{\Delta_{r\phi} p_T}{0.3 B L'^2} \sqrt{\frac{720}{N+5}}.$$

Inserting the values for a track coming from the vertex and crossing both jet chambers, namely  $N = 56$ ,  $\Delta_{r\phi} = 150 \mu m$ ,  $B = 1.136 T$  and  $L' = 0.6 m$  [13], one obtains

$$\frac{\Delta p_T}{p_{T,es}} = 0.0042 p_T.$$

The second term  $\Delta \theta$  is given by the resolution of the  $z$ -chambers in combination with the  $z$ -measurement in the jet chambers. In fitting a straight line to the measured points in the  $rz$  plane the influence of the different detector parts can be demonstrated. From a straight line fit one gets for the coordinate  $z_0$  at the vertex  $r = 0$  and for the slope  $\alpha = \tan \theta$

$$\begin{aligned} z_0 &= (S_{zg} \cdot S_{r_g^2} - S_{r_{zg}} \cdot S_{r_g}) / D \\ \alpha &= (S_{r_{zg}} S_g - S_{z_g} \cdot S_{r_g}) / D \end{aligned}$$

where

$$\begin{aligned} S_{zg} &= \sum_{i=1}^n z_i g_i & S_{r_g^2} &= \sum_{i=1}^n r_i^2 g_i \\ S_{r_{zg}} &= \sum_{i=1}^n r_i z_i g_i & S_{r_g} &= \sum_{i=1}^n r_i g_i \\ S_g &= \sum_{i=1}^n g_i & \text{with the weights } g_i &= \frac{1}{(\Delta z_i)^2} \end{aligned}$$

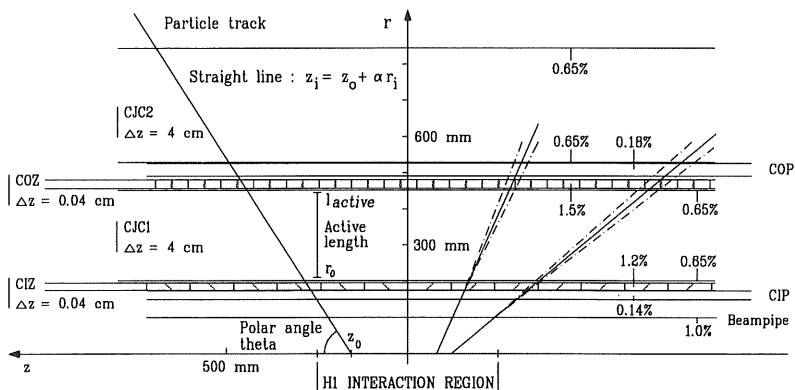


Figure 2.7: Track coordinates in  $rz$  given by  $z$  and the slope  $\alpha$ . The numbers on the right give the radiation length of the different parts.

and  $D = S_g \cdot S_{r_g}^2 - (S_{r_g})^2$ . The resolution of  $z_0$  and  $\alpha$  is

$$\Delta z_0^2 = S_{r_g} / D$$

$$\Delta \alpha^2 = S_g / D$$

Assuming a simple model, where the points are aequidistant and all measurements have the same weight  $g$ ,  $\Delta z_0$  and  $\Delta \alpha$  can be calculated. With  $r_i = r_0 + (i-1)l_{active}/(N-1)$  and  $g_i = g = 1/(\Delta z)^2$  follows

$$S_g = Ng \quad S_{r_g} = Ng \left( r_0 + \frac{l_{active}}{2} \right)$$

$$S_{r_g}^2 = Ng (r_0^2 + r_0 l_{active} + l_{active}^2 (2N-1)/6(N-1))$$

and for the resolutions

$$\Delta z = \frac{r_0 \Delta z}{l_{active}} \sqrt{\frac{12(N-1)}{N(N+1)} \left( 1 + \frac{l_{active}}{r_0} + \frac{l_{active}^2 (2N-1)}{r_0^2 6(N-1)} \right)}$$

$$\Delta \alpha = \frac{\Delta z}{l_{active}} \sqrt{\frac{12(N-1)}{N(N+1)}}$$

In the following table 2.2 the resolution of each detector part as well as the combined resolutions are given assuming the given intrinsic resolutions  $\Delta z$ . The active region of the detector starts at  $r_0$  and the length is  $l_{active}$ . With  $\alpha = \tan \theta$ , using all detectors the resolution of the polar angle is  $\Delta \theta = \Delta \alpha \cos^2 \theta = 1.07 \text{ mr} \cos^2 \theta$  and the spatial resolution

Single resolutions						
Detector	$n$	$r_0[cm]$	$l_{active}[cm]$	$\Delta z[cm]$	$\Delta z_0[cm]$	$\Delta\alpha[mr]$
CIZ	3	18.0	1.0	0.04	1.05	56.6
COZ	4	46.0	1.8	0.04	1.40	29.8
CJC1	24	21.8	20.7	4.0	4.29	131.1
CJC2	32	54.5	27.8	4.0	5.88	85.4

Combined resolutions		
Detectors	$\Delta z_0[cm]$	$\Delta\alpha[mr]$
CIZ / COZ	0.04	1.07
CIZ / CJC1	0.72	38.70
CIZ / CJC1 / COZ	0.04	1.07
CJC1 / CJC2	1.55	27.51
CJC1 / COZ / CJC2	0.93	19.72
CIZ / CJC1 / CJC2	0.25	13.16
All detectors		
CIZ / CJC1 / COZ / CJC2	0.04	1.07

Table 2.2: Single and combined resolutions of the central tracking detectors.

in  $z$  at the vertex ( $r = 0$ ) is  $\Delta z_0 = 0,04cm$ . The total momentum resolution can then be calculated as

$$\frac{\Delta p}{p} = \sqrt{(0,0042p \sin \theta)^2 + \frac{\cos^2 \theta}{\sin^2 \theta} (\Delta \theta)^2}.$$

In Figure 2.8 the momentum resolution is shown for the combined set of all detectors and as a comparison only using the jet chambers. The resolution for the ideal detector is plotted in 2.9 for different momenta.

## 2.4.2 Influence of multiple scattering

In addition to the spatial resolution multiple scattering must be considered. Though the distribution of scattering angles for large-angle scatterings shows non-Gaussian tails. We use the Gaussian approximation [14] to estimate the influence on the detector performance. One then gets for the width

$$\Delta \theta = \frac{13.6MeV}{\beta c p} z \sqrt{x/X_0} [1 + 0.038 \ln(x/X_0)]$$

where  $p, \beta$ , and  $z$  are the momentum in MeV/c, velocity  $v/c$  and charge number of the incident particle. The thickness of the scattering medium is given in radiation length  $x/X_0$ . Considering now a track coming from the vertex in the  $r\phi$  plane, the multiple scattering in the material in front of the inner jet chamber e.g., the beam pipe, the CIP, CIZ and the jet chamber wall will contribute to the error of the azimuthal angle  $\phi$  and the distance of closest approach (DCA) because of the resulting deflections. The error



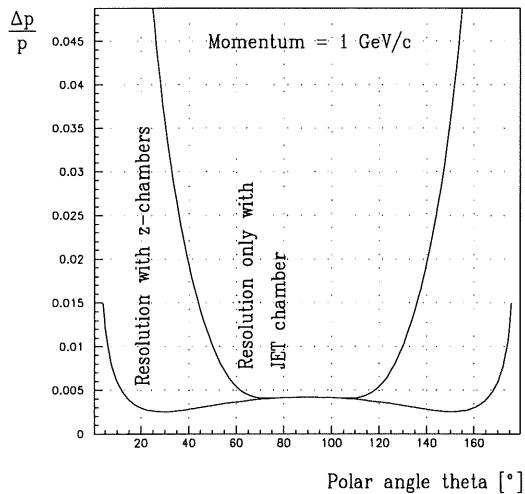


Figure 2.8: Resolution including the z-chambers and using only the JET chambers.

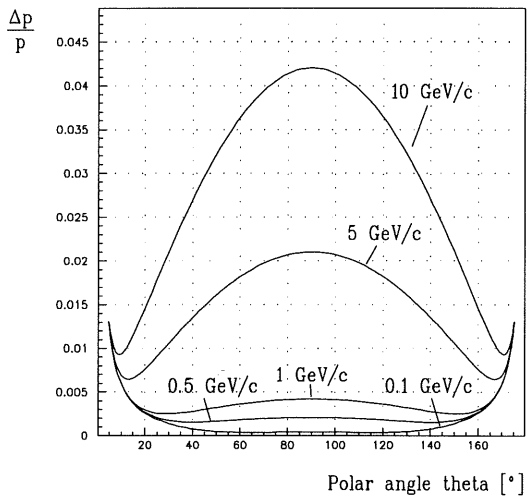


Figure 2.9: Momentum resolutions versus the polar angle.

in curvature within a jet chamber will only come from scattering in the gas of the active detector volume. Following [12] the contribution due to multiple Coulomb scattering is approximately

$$\Delta\kappa_{ms} = \frac{0.016(\text{GeV}/c)Z}{Lp\beta} \sqrt{\frac{L}{X_0}}$$

and the contribution to the resolution of the transverse momentum

$$\frac{\Delta p_{Tms}}{p_T} = \frac{0.016(\text{GeV}/c) \sin \theta}{0,3 \cdot BL\beta} \sqrt{\frac{L}{X_0}}.$$

The total error in the measurement of the transversal momentum is therefore

$$\left(\frac{\Delta p_T}{p_T}\right)^2 = \left(\frac{\Delta p_{Tres}}{p_T}\right)^2 + \left(\frac{\Delta p_{Tms}}{p_T}\right)^2.$$

As shown in Figure 2.10, for a given polar angle  $\theta$  the contribution from multiple scattering does not vary with the momentum in contrast to that from spatial resolution. In the  $rz$

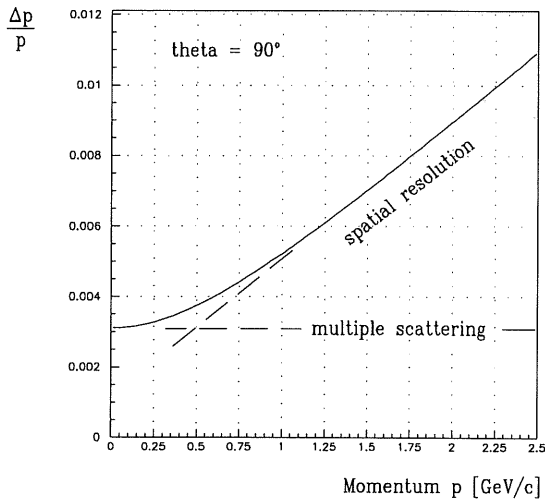


Figure 2.10: Multiple scattering for a given polar angle  $\theta$ .

plane the direction of the track will be deflected by multiple scattering as well. This will introduce an error on the measurement of the polar angle  $\theta$  and the origin  $z_0$  of the track. The error of the momentum measurement can then be expressed as

$$\frac{\Delta p}{p} = \sqrt{\left(\frac{\Delta p_{Tres}}{p_T}\right)^2 + \left(\frac{\Delta p_{Tms}}{p_T}\right)^2 + \frac{\cos^4 \theta}{\sin^2 \theta} (\Delta\theta_{res}^2 + \Delta\theta_{ms}^2)}.$$

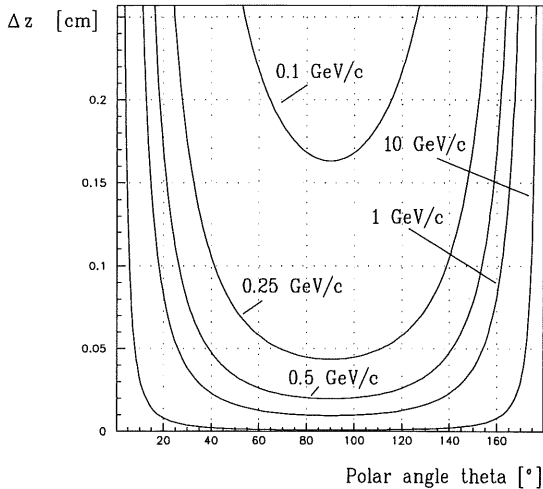


Figure 2.11: Width of the distribution in the CIZ due to multiple scattering in the beampipe wall.

The error in  $\Delta\theta_{ms}$  results from multiple scattering deflections between the interaction point and the COZ as illustrated in Figure 2.7. In this region of the central tracker the beampipe and the detector elements in front of the active volume of the inner jet chamber are the most dense parts. Multiple scattering processes in the beampipe wall will distort the  $z$  coordinate measurement already in the CIZ. The resulting width depends on the polar angle and the distance between the beam pipe and the chamber. It is shown in Figure 2.11, using the radiation length of 1% for the beampipe. Scattering processes in the material in front of the active volume of the inner JET chamber (CIP, CIZ and CJC1 wall) will not much influence the  $z$  measurement in the CIZ, but still lead to a smeared  $z$  coordinate measurement of the COZ. Hence it is obvious, that in reducing the above mentioned material, one will improve the momentum measurement.

## 3 General aspects of drift chambers

### 3.1 Introduction

The processes which lead to particle detection differ for neutral and charged particles. The electromagnetic interaction of charged particles allows a direct measurement. Photons interact in different ways depending on their energy, i.e. via photoeffect, Compton scattering and pair production, producing charged particles which then can be measured directly. Neutrons produce charged secondary particles via strong interactions with nucleons. Neutrinos can only be observed through their weak interaction with electrons and nucleons. Ultimately it is always an electromagnetic process, which is used as a basis for detection.

In 1908 Ernest Rutherford and Hans Geiger built the first prototype of a single wire gas chamber. It was simply a metallic cylinder containing an ionizing gas and a single anode wire running along the axis kept at high potential (Figure 3.1). If a particle traverses the chamber it liberates electrons, which are then accelerated in the electric field to high enough energies to produce an avalanche of secondary electrons through further ionisation. The negative charge is finally collected at the anode wire, while the ions move towards the cylinder. For very high applied voltages the avalanche fully discharges the potential difference. This is the well known "Geiger" mode of operation, where the resulting signal is so large, that one needs only a microphone and speaker to hear the familiar click of the Geiger Counter. For lower voltage the anode signal is proportional to the initial ionization with a multiplication factor of about  $10^4$  for every primary electron. This voltage regime is called the proportional mode. The proportional counter did not find widespread application in high energy physics until Georges Charpak built the first multiwire tracking chamber in 1968. In Charpak's design a parallel array of fine, grounded anode wires was sandwiched between two cathode planes or meshes kept at a potential several kilovolts in an atmosphere of ionizing gas (Figure 3.1). With a gap between the anode and the cathode planes of about 6 mm the adjacent anode wires were only separated by 2 mm. It is this small spacing that determines the spatial resolution of the instrument. Testing his first chamber with an x-ray source, he found that the anode wire closest to the point where the primary ionization occurred showed a negative voltage pulse as one would expect. The two anode wires on either side of it unexpectedly exhibited positive pulses. The negative pulse flanked by two induced positive pulses identified the wire of closest approach quite unambiguously. The 1992 Nobel Prize went to Georges Charpak for inventing these detectors, whose main advantage over the existing device was the capability to handle a million events per second without an external trigger. The multiwire proportional chamber and its derivatives — the drift chamber, the time projection chamber (TPC) and the time expansion chamber (TEC) are the principal means by which high-energy physicists visualize the tracks of particles emerging from collisions at the big accelerators. Presently the experimentalists are developing new types of gas chambers, like straw tubes, honeycomb strip chambers and gas microstrip detectors.

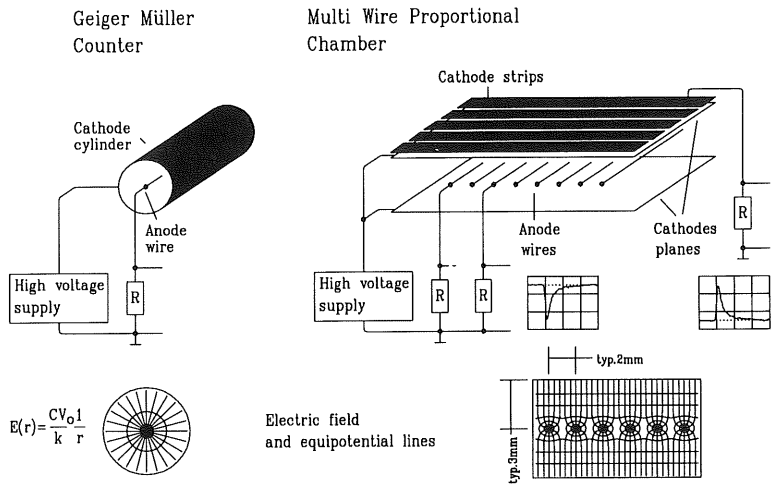


Figure 3.1: From the single wire to the multiwire proportional chamber.

The devices are also used in many different fields, e.g. in medicine and biology as imaging detectors.

The primary electrons drift in the electric field towards the nearest anode wire. The avalanche does not begin until they are within about  $50 \mu\text{m}$  of the wire, because only there the field is high enough to produce a strong accelerating field. The positive ions created in the avalanche, rather than the electrons, produce most of the negative pulse on the wire, essentially because the ions traverse a larger potential difference as they move far away from the wire than does the incoming electron avalanche. The recession of the ions induces also the positive pulses on the adjacent wires, and on the cathode planes as well. By segmenting the cathode planes into strips running perpendicular to the anode wires one can thus localize the avalanche in two dimensions. The cathode pulses appear essentially simultaneous with the anode pulses, long before the slow ions actually reach the cathodes. The pulses can be recorded within about 20 ns after the particle passage. The actual time resolution of the instrument depends also on the geometry, because the liberated electrons have to travel a certain distance to the anode wire before they produce a signal. This drift time contributes to the time resolution.

### 3.1.1 The drift chamber

The spacing between the anode wires needs not to be the limit of spatial resolution. If one also measures the time delay it is possible to determine the origin of the electrons

more precisely. In a drift chamber the primary electrons typically drift for about several centimeters in a low intensity electric field before they reach the anode wire at the time  $t_A$ . The coordinate of the ionizing particle (produced at time  $t_0$ ) relative to the anode wire is then given by

$$z = \int_{t_0}^{t_A} v_D(t) dt .$$

Here  $v_D(t)$  is the drift velocity. The drift velocity is essentially proportional to the electric field  $E$  at constant pressure  $p$  ( $v_D \sim E$ ). A careful choice of the field configuration results in a more or less constant field and the relation becomes linear

$$z = v_D \cdot (t_A - t_0) = v_D \cdot \Delta t .$$

The dependence of the drift velocity on the electric field in the gas mixture used has to be minimized such that inhomogeneities in the field have only small effects and become negligible. Not only the drift and the diffusion of the electrons and ions in the electric and magnetic field towards the anode wire, determines the resolution, but also the primary ionisation process, the gas amplification near the anode wire and the time resolution of the signal electronics. In the next chapters these aspects will be dealt with in more detail (for enthusiasts more details and references can be found in [15, 16]).

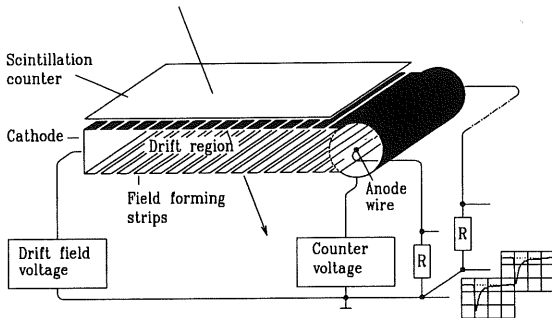


Figure 3.2: Sketch of a single cell drift chamber.

## 3.2 Detection of charged particles

### 3.2.1 Energy loss due to electromagnetic interaction

As a particle passes through a medium it can ionize an atom, emit Cerenkov light or produce transition radiation by electromagnetic interaction. A precise calculation in the photoabsorption and ionization (PAI) model [17] yields the cross section as a function of

the energy  $E$  and the momentum  $\vec{p}$  for a charged particle in a medium ( $Z, A$ ) with the complex dielectric constant  $\varepsilon = \varepsilon_1 + i\varepsilon_2$ . ( $\varepsilon_1 = u^2$ ,  $\beta = \frac{v}{c}$ )

$$\frac{d\sigma}{dE} = \frac{\alpha}{\beta^2\pi} \frac{\sigma_\gamma(E)}{EZ} \ln[(1 - \beta^2\varepsilon_1)^2 + \beta^4\varepsilon_2^2]^{-1/2} + \frac{\alpha}{\beta^2\pi} \frac{\sigma_\gamma(E)}{EZ} \ln\left(\frac{2mc^2\beta^2}{E}\right) + \frac{\alpha}{\beta^2\pi} \frac{1}{E^2} \int_0^E \frac{\sigma_\gamma(E')}{Z} dE' + \frac{\alpha}{\beta^2\pi} \frac{1}{ZN\hbar c} (\beta^2 - \frac{\varepsilon_1}{|\varepsilon|^2})\theta$$

where  $\alpha$  is the fine structure constant, and  $\theta = \arg(1 - \varepsilon_1\beta^2 + i\varepsilon_2\beta^2)$ . In this expression  $\sigma_\gamma$  gives the cross section for the absorption of a photon with energy  $E$  by the atoms of the medium. The first three terms describe the energy loss of the charged particle by ionization and the fourth describes the Cerenkov radiation — The third term gives the probability for producing energetic electrons ( $\delta$  electrons). From the first two terms one can calculate approximately the differential energy loss  $dE/dx$  for a particle, i.e. the Bethe-Bloch formula [18]

$$-\frac{dE}{dx} = \frac{4\pi r_e^2 m_e c^2 N_0 Z z^2}{A\beta^2} \left[ \ln\left(\frac{2m_e c^2 \beta^2}{(1 - \beta^2)I}\right) - \beta^2 \right].$$

In this relation  $r_e$  is the classical Thomson radius of the electron,  $N_0$  Avogadro's number,  $z$  the charge of the particle, and  $I$  the average ionisation potential of the medium. The expression shows, that the differential energy loss depends only on the projectile velocity  $\beta$  and not on its mass. After a fast decrease dominated by the  $\beta^{-2}$  term, the energy loss reaches a constant value around  $\beta \cong 0,97$  and eventually slowly increases (relativistic rise). This increase is a basis for particle identification at very high energies since, for

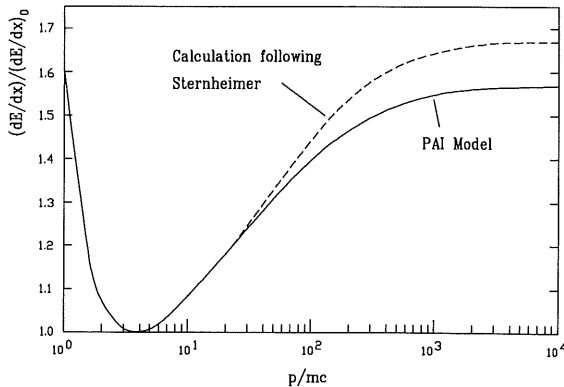


Figure 3.3: Energy loss by ionization.

a given momentum, the average energy loss will be different for different masses. Even

for thin materials, the electromagnetic energy loss is the result of a small number of discrete interactions. These interactions can be divided in close collisions, with large energy transfers resulting in liberation of charges (ionization), and distant collisions involving smaller energy transfers and resulting in both ionization and atomic excitation. The wide range of possible energy transfers, determines a characteristic shape of the energy loss distribution. In a classical formulation the energy loss distribution was calculated by

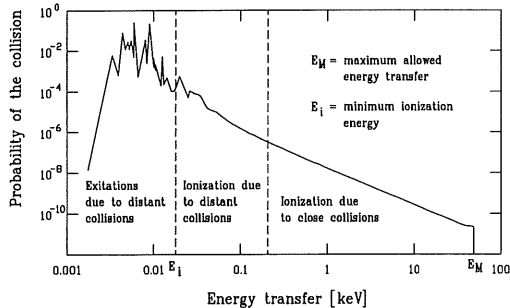


Figure 3.4: Relative probability of different processes induced by fast (100 keV) electrons in water, as a function of the energy transfer in a collision.  $E_M = 50$  keV is the maximum kinematically allowed energy transfer.

Landau [19] and Sternheimer [20]. This approximation does not reproduce the measured energy loss distribution for thin media very accurately. The more precise calculation in the PAI model which considers the shell structure of the atoms gives a better description. It also reproduces the relativistic rise in Figure 3.3. The ejected electron in the primary ionization can have enough energy (larger than the ionization potential of the medium) to further ionize, producing secondary ion pairs. The sum of the two contributions is called total ionization and the total number of ion pairs is conveniently expressed by

$$n_T = \frac{\Delta E}{W_i},$$

where  $\Delta E$  is the total energy loss in the gas volume considered and  $W_i$  is the effective average energy to produce one pair. The total number of ion pairs is 2 – 7 times the number of primary pairs.

### 3.2.2 Statistical distribution of ion pair production

Since the primary ionization process results from a small number of collisions, it is governed by Poisson statistics. The probability for the actual number  $k$  is then given by

$$P_k^n = \frac{n^k}{k!} e^{-n}$$



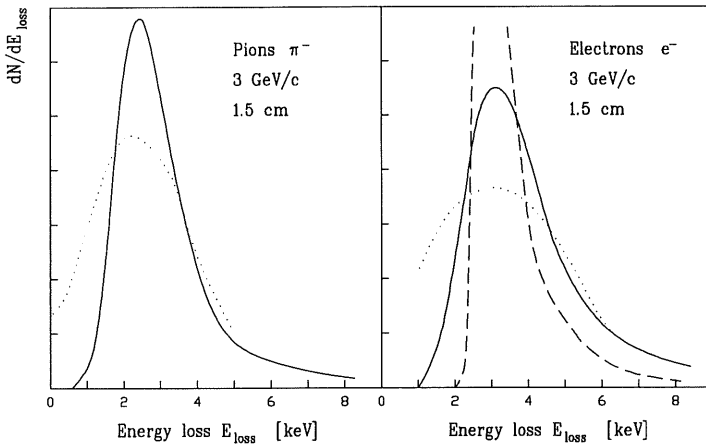


Figure 3.5: Calculated energy loss distributions for  $\pi$ -mesons and electrons in 1.5 cm of  $Ar/CH_4$  (95/5) at 1 atm (for references see [16]).

Gas	Z	A	$\rho$ g/cm <sup>3</sup>	$E_{ex}$	$E_i$ eV	$I_0$	$W_i$	$dE/dx$ MeV/(gcm <sup>2</sup> ) (keV/cm)	$n_p$ i.p./cm	$n_T$ i.p./cm
H <sub>2</sub>	2	2	$8.38 \times 10^{-5}$	10.8	15.9	15.4	37	4.03 (0.34)	5.2	9.2
He	2	4	$1.66 \times 10^{-4}$	19.8	24.5	24.6	41	1.94 (0.32)	5.9	7.8
N <sub>2</sub>	14	28	$1.17 \times 10^{-3}$	8.1	16.7	15.5	35	1.68 (1.96)	(10)	56
O <sub>2</sub>	16	32	$1.33 \times 10^{-3}$	7.9	12.8	12.2	31	1.69 (2.26)	22	73
Ne	10	20.2	$8.39 \times 10^{-4}$	16.6	21.5	21.6	36	1.68 (1.41)	12	39
Ar	18	39.9	$1.66 \times 10^{-3}$	11.6	15.7	15.8	26	1.47 (2.44)	29.4	94
Kr	36	83.8	$3.49 \times 10^{-3}$	10.0	13.9	14.0	24	1.32 (4.60)	(22)	192
Xe	54	131.3	$5.49 \times 10^{-3}$	8.4	12.1	12.1	22	1.23 (6.76)	44	307
CO <sub>2</sub>	22	44	$1.86 \times 10^{-3}$	5.2	13.7	13.7	33	1.62 (3.01)	(34)	91
CH <sub>4</sub>	10	16	$6.70 \times 10^{-4}$		15.2	13.1	28	2.21 (1.48)	16	53
C <sub>4</sub> H <sub>10</sub>	34	58	$2.42 \times 10^{-3}$		10.6	10.8	23	1.86 (4.50)	(46)	195

Table 3.1: Properties of several gases used in proportional counters [15]. The energy loss and the ion pairs per unit length are given at atmospheric pressure for minimum ionizing particles.

where  $n$  is the average number of primary interactions. Defining the efficiency of a perfect detector as  $\epsilon$  one can write the inefficiency as

$$1 - \epsilon = P_0^n = e^{-n}$$

with the values for  $n$  from Table 3.1 for a given detector the limits can be estimated. The resolution of the detector will also depend on the space distribution of the ion-electron pairs. The probability for producing a pair along a track is proportional to the ionizing length. Taking this into consideration the space distribution of each pair  $j$  ( $1 \leq j \leq k$ ) along a normalized coordinate  $x$  ( $0 \leq x \leq 1$ ), when  $k$  ion pairs are produced in an event, can be calculated

$$D_j^k(x) = \frac{k!}{(k-j)!(j-1)!} (1-x)^{k-j} x^{j-1} .$$

With the Poisson distribution one gets a more general expression for the space distribution

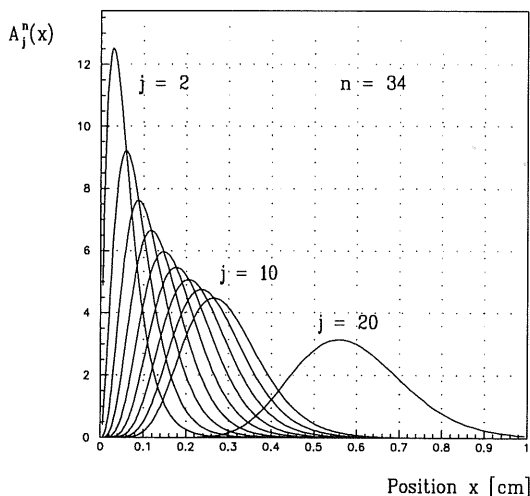


Figure 3.6: Space distribution of the  $j^{\text{th}}$  ion pair along the normalized coordinate  $x$ .

of the pair  $j$ , if  $n$  is the average number produced.

$$A_j^n(x) = \sum_{k=j}^{\infty} P_k^n D_j^k = \frac{x^{j-1}}{(j-1)!} n^j e^{-nx}$$

Considering the commonly used gas Argon ( $Ar$ ) in a 1 cm thick detector the average number of produced ion pairs is  $n = 34$ . The space distribution for some ion pair is represented in Figure 3.6 as a function of the coordinate along the ionizing track. For

the  $j^{th}$  pair which eventually leads to the detector signal the distribution has a certain spread (typically  $100 - 200\mu\text{m}$ ) and it is therefore obvious, that the statistics of the ion pair production sets a limit to the resolution of the detector.

### 3.3 Drift and diffusion of charges in gases with electric and magnetic field

#### 3.3.1 Mobility of ions

In the electric field applied across the detector volume the primary ions experience a constant force. The average drift velocity  $v_D^+$  along the field direction is found to be proportional to the so called reduced field  $E/p$ , with  $p$  being the gas pressure. This is true up to very high fields. It is convenient to define the mobility  $\mu^+$  as

$$\mu^+ = v_D^+ \left(\frac{E}{p}\right)^{-1} \text{ and } v_D^+ = E \cdot \frac{1}{p\mu^+} .$$

The average energy of the ions is almost unmodified by the applied field and the mobility consequently constant. This will not be the case for the electrons.

For mixtures of  $n$  gases as used in detectors the mobility  $\mu_i^+$  of the ion is given by

$$\frac{1}{\mu_i^+} = \sum_{j=1}^n \frac{p_j}{\mu_{ij}^+}$$

where  $p_j$  is the volume concentration of gas  $j$  in the mixture. In gas mixtures however

Gas	A	u cm/s	D <sup>+</sup> cm <sup>2</sup> /s	$\mu^+$ cm <sup>2</sup> s <sup>-1</sup> V <sup>-1</sup>	$\lambda$ 10 <sup>-5</sup> cm
H <sub>2</sub>	2.02	$1.8 \times 10^5$	0.34	13.0	1.8
He	4.00	$1.3 \times 10^5$	0.26	10.2	2.8
Ar	39.95	$0.41 \times 10^5$	0.04	1.7	1.0
O <sub>2</sub>	32.00	$0.46 \times 10^5$	0.06	2.2	1.0
H <sub>2</sub> O	18.02	$0.61 \times 10^5$	0.02	0.7	1.0

Table 3.2: Thermal velocity, diffusion coefficients, mobility and the classical mean free path for molecules [15].

the ions with higher ionization potential transfer its charge to a molecule with a lower ionization potential. It takes between 100 and 1000 collisions for an ion to transfer the charge and finally only one kind of ion will be left migrating.

### 3.3.2 Drift and diffusion of electrons in electric and magnetic fields

The mean free pathlength of electrons is larger than that of the ions. Therefore electrons accumulate more energy between two collisions. Their mobility is 100 to 1000 times larger than the ion mobility. Following Townsend one writes the drift velocity as

$$v_D^e = \frac{e}{m} E \tau .$$

where  $\tau$  is the mean time between collisions. In this expression  $\tau$  varies for some gases very strongly with  $E$  going through maxima and minima (Ramsauer effect). The electron wavelength in the range of a few eV kinetic energy approaches the diameter of the electron shells. The resulting quantum-mechanical processes change the original Maxwellian energy distribution. At high fields the average energy can exceed the thermal value by several orders of magnitude. For the study of drift chamber performance theories of electron drift in gases have been developed. If the electrons produced by ionization are not subjected to any electric or magnetic fields they will move randomly with an average energy given by the formula  $\varepsilon = \frac{3}{kT}$  (about  $3,7 \times 10^{-2} \text{eV}$  at  $18^\circ$ )

$$F(\varepsilon) = c\sqrt{\varepsilon} e^{-\left(\frac{\varepsilon}{kT}\right)} .$$

In the presence of electric and magnetic fields, the free electrons will continue to have a nondirectional velocity  $v_D^e$  but they will exhibit a small drift according to the field directions. The velocity is entirely determined by the cross sections and the fields. The successful classical theory of electrons in gases is based on the Boltzmann transport equation. If one introduces the distribution function  $f(\vec{v}, \vec{r}, t)$  of the electrons at the point  $\vec{r}$ ,  $\vec{v}$  of phase space at time  $t$ , we have

$$\frac{\partial f}{\partial t} = -\vec{v} \text{ grad}_{\vec{r}} f - \vec{a} \text{ grad}_{\vec{v}} f + \left[ \frac{\delta f}{\delta t} \right]_{\text{via collisions}}$$

where  $\vec{a} = \vec{a}(\vec{E}, \vec{B})$  depends on the applied fields. Solving the equation numerically [21] one gets the drift velocity  $v_D^e$  as well as the diffusion coefficient  $D$ .

Assuming, that the electrons diffuse by multiple collision following a Gaussian law, then the number of electrons at the point  $x$  at time  $t$  is given by solving the diffusion equation

$$n(x, t) = \frac{1}{\sqrt{4\pi Dt}} \cdot e^{-\frac{x^2}{4Dt}} .$$

For a constant drift velocity  $v_D^e = x/t$  the standard deviation can be written as

$$\sigma = \sqrt{2Dt} = \sqrt{\frac{2Dx}{v_D^e}} .$$

It is customary to define a characteristic energy  $\varepsilon_k$  as follows

$$\varepsilon_k = \frac{eD}{\mu^e} = \frac{eDE}{v_D^e} > kT$$

with the electron mobility  $\mu^e = v_D^e/E$ . Replacing the diffusion coefficient with the characteristic energy  $\varepsilon_k$  one obtains

$$\sigma = \sqrt{2\varepsilon_k x / eE}.$$

Hence for a given drift distance  $x$  the diffusion will be minimal for  $\varepsilon_k = kT$ . In electric and magnetic fields the charged particle move along circular trajectories superimposed to the translation with velocity  $\vec{v}_D$ . Knowing the drift velocity  $\vec{v}_D$  one can solve the equation of motion. The result can be written as

$$\vec{v}_D = \frac{\mu}{1 + \omega^2\tau}(\vec{E} + \frac{\vec{E} \times \vec{B}}{B}\omega\tau + \frac{(\vec{E} \cdot \vec{B}) \cdot \vec{B}}{B^2}\omega^2\tau^2)$$

with  $\mu = q\tau/m = v_D/E$  the electron mobility, and  $\omega$  the cyclotron frequency. Generally  $\vec{v}_D$  consists of a component parallel to  $\vec{E}$ , one parallel to  $\vec{B}$  and a third which is perpendicular to the plane formed by  $\vec{E}$  and  $\vec{B}$ . The diffusion in an electric field is not isotropical as calculations and measurements show [22]. The component  $D_{L\vec{E}}$  along the electric field will be changed. If  $D$  is the diffusion coefficient in gas without fields one finds for the longitudinal and transversal components in an electrical field

$$D_{L\vec{E}} \neq D \quad D_{T\vec{E}} = D.$$

In a magnetic field the longitudinal component  $D_{L\vec{B}}$  ( $D_L || \vec{B}$ ) will not be changed whereas the transversal component will become smaller.

$$D_{L\vec{B}} = D \quad D_{T\vec{B}} = \frac{D}{1 + \omega^2\tau^2}.$$

Only in the case, where the electric field is parallel to the magnetic field a simple combination of these results is possible, namely

$$\begin{aligned} \sigma_{L_{\vec{E}||\vec{B}}} &= \sqrt{2D_{L_{\vec{E}||\vec{B}}}t} = \sqrt{2D_{L_t}t} \neq \sqrt{2Dt} \\ \sigma_{T_{\vec{E}||\vec{B}}} &= \sqrt{2D_{T_{\vec{E}||\vec{B}}}t} = \sqrt{2\frac{D}{1 + \omega^2\tau^2}t} \end{aligned}$$

### 3.4 Loss of primary ion pairs by recombination and electron capture

Some of primary ions may be lost due to neutralisation through negative ion or electron capture, charge transfer to other molecules or extraction of electrons from the chamber. Electrons may also be lost through neutralisation, absorption in the walls or attachment to a molecule during a collision. The probability for the latter process is essentially zero for

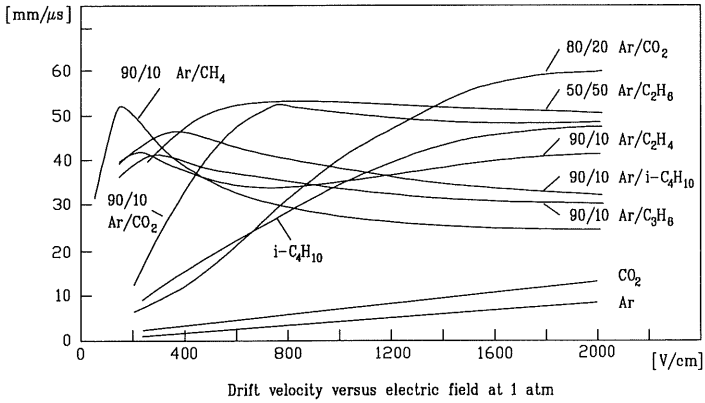


Figure 3.7: Drift velocity versus the electric field for various gases.

noble gases,  $N_2$ ,  $H_2$  and  $CH_4$ , while for other gases it may be non-negligible, in particular for electronegative pollutants like oxygen and water.

If  $p$  is the fraction of the electronegative additive in the gas, the attachment probability can be calculated knowing the drift velocity  $v_D^e$ , the electron mean free path  $\lambda$  and the instant velocity  $u_e \cong \sqrt{3kT/m_e}$ . The number of collisions for an electron with the electronegative molecules is  $u_e p / \lambda$  and the probability of attachment therefore

$$p_{attach} = \frac{h u_e p}{\lambda v_D^e} = \frac{1}{\lambda_c}$$

Here  $h$  is a coefficient characteristic for the attachment. With  $\lambda(\varepsilon) = 1/(N\sigma(\varepsilon))$  and  $u_e = \sqrt{2\varepsilon/m_e}$  one obtains

$$\lambda_c = \sqrt{\frac{m}{2\varepsilon}} \frac{v_D^e}{N h p d(\varepsilon)}$$

The loss of electrons in a constant field across a distance  $x$  is now given by the relation

$$\frac{n}{n_0} = e^{-x/\lambda_c}$$

If one is adding water to the detector gas this loss has to be considered.

### 3.5 Excitation and ionization in high electric fields

Near the anode wires the electric field increases to a few kV/cm. The electrons receive enough energy between two collisions to allow inelastic excitation in various ways, and

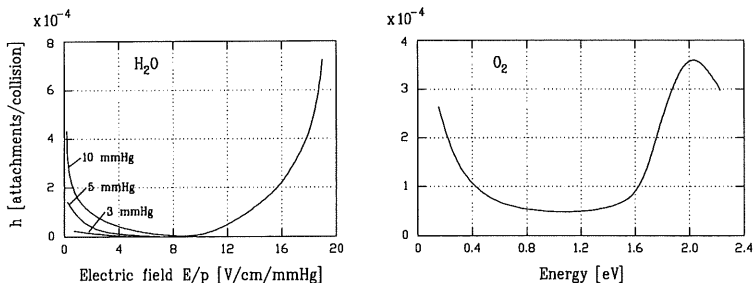


Figure 3.8: Attachment coefficient for electrons in oxygen and water, as a function of electron energy.

ionization. Among the detector gases the weakly-bound polyatomic molecules will undergo radiationless rotational and vibrational transitions whereas noble gases can only be excited through photon absorption or emission. It is essential for gaseous detectors to dissipate a good fraction of the energy in radiationless transitions to allow high gain and stable operation. If the energy of an electron increases over the first ionization potential

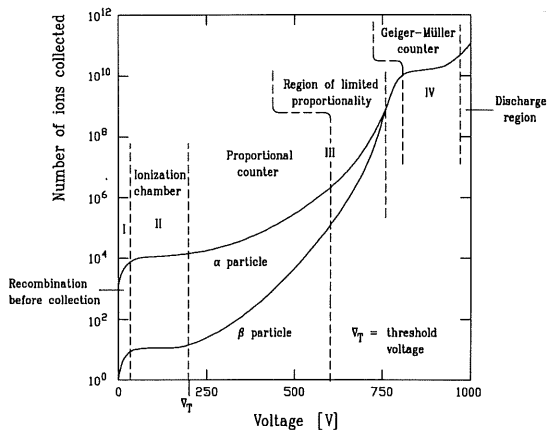


Figure 3.9: Gain-voltage characteristic for a proportional counter.

of the gas  $E_{igas}$ , the result of a collision can be an ion pair, while the primary electron continues its journey. Above threshold the probability of ionization rapidly increases leading to avalanche formation. For the geometry of the original cylindrical proportional counter a relation between the charge collected on the wire and the potential difference may be

established (Figure 3.9). Four different regions may be distinguished. At low voltages some charge is collected, but recombination still dominates. When all primary electrons reach the anode full collection starts and the detector works in the ionization chamber mode. At a threshold voltage  $V_T$  the field close to the anode is large enough to initialize the multiplication process. Gains in excess of  $10^4$  can be obtained by increasing the voltage. For multiplication factors up to  $10^8$  the collected charge can be proportional to the original charge and therefore also proportional to the energy loss. This feature is lost at higher potential differences due to field distortions by the large space charge building up around the anode wire. Proceeding further the photon emission process starts leading up the typical Geiger-Müller operation mode. This mode introduces a large dead time, which can be avoided in the proportional mode.

The number of electrons  $n$  at a given position  $x$  will increase by an amount  $dn$  after a path  $dx$  as

$$dn = n\alpha(x)dx \text{ and } n = n_0 e^{\int_a^c \alpha(x)dx}$$

where  $\alpha(x)$  is the inverse of the mean free path for ionization. It is called the first Townsend coefficient and represents the number of ion pairs produced per unit drift length. The multiplication factor is then

$$M = \frac{n}{n_0} = e^{\int_a^c \alpha(x)dx} .$$

From the known Townsend coefficient for a given electric field one can compute the multiplication factor. Many analytical approximations for  $\alpha$  exist which are valid in different regions of  $E$  [23]. Computer simulations of avalanches have also been performed [24]. Figure 3.10 shows the simulated development of an avalanche, which also gives an im-

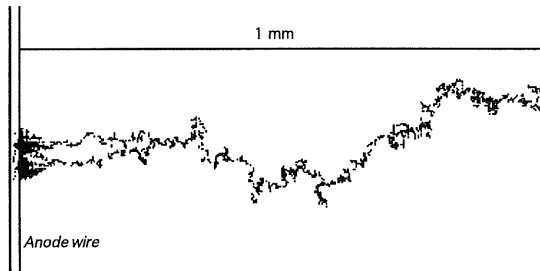


Figure 3.10: Simulated avalanche generated by a primary electron.

pression of the transversal diffusion. For low values the coefficient  $\alpha$  can be assumed to



linearly depend on the energy of the electrons [25]

$$\alpha = kN\varepsilon .$$

The limits of this approximation are apparent from Figure 3.11. Adding polyatomic components to noble gas generally increases the value of the necessary field for a given value of  $\alpha$ . Processes like the space charge deformation, which appears near the front of the avalanche and the photon emission mentioned above, where the photon generates a new avalanche are limiting the multiplication factor. The phenomenological limit established by Raether [15] is  $M \sim 10^8$ , but in practice one has to operate at average gains below  $10^6$  because of the statistical distribution of the electron energy.

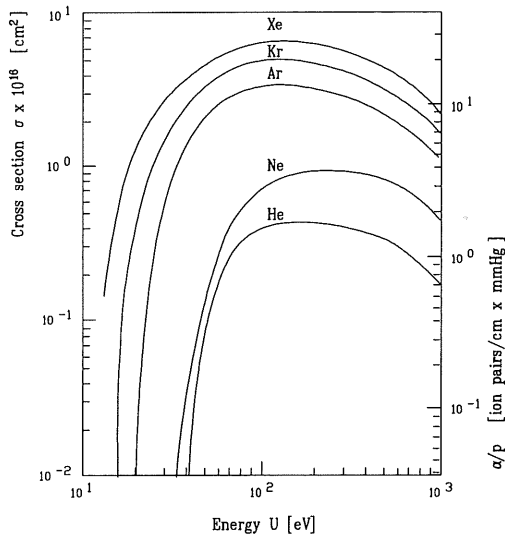


Figure 3.11: Cross section and first Townsend coefficient as a function of electron energy, for noble gases.

### 3.6 Resolution of the particle track coordinate measuring the drift time

Apart from problems such as imperfect electronics and mechanical construction the accuracy of the drift time measurement is determined by three different processes.

The dispersion of the number of primary electrons resulting (see Chapter 3.2) will clearly contribute to the spatial resolution. If a particle passes a drift cell the electron with the shortest drift distance will determine the final drift time and track coordinate. The spatial distribution of the first electron candidate can be deduced from Figure 3.6. Increasing the electron density will reduce this spread.

If the lines of constant drift times (isochrones) can be approximated by circles (see Figure 3.12) the error introduced by the dispersion will depend on the isochrone radius. Obviously this error will be most important close to the wire, where the radius of the isochrones is quite small.

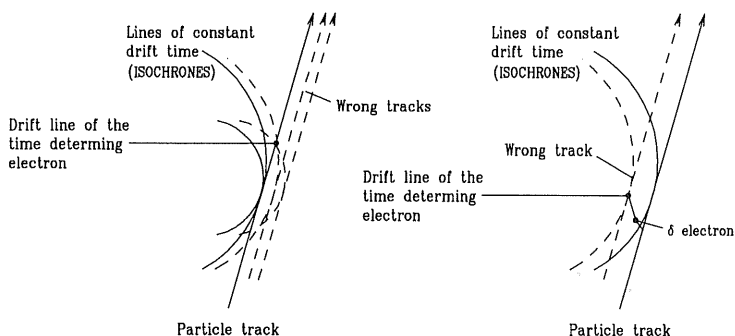


Figure 3.12: Illustration of the errors on the drift time measurement resulting from fluctuations in the primary ionisation and  $\delta$  electrons.

Particles with high energies may also lead to a  $\delta$  electron of relatively high energy which can travel an appreciable distance in the chamber ( $\sim 10\mu\text{m}$ ). Computing this contribution to the resolution of the detector accurately is difficult because one has to take into account random walk, but its effect is nearly independent of the drift distance.

The accuracy of a drift chamber is further limited by the diffusion in the detector gas, which shows a dispersion in drift direction given by (see Chapter 3.3)

$$\sigma = \sqrt{2D_L x / v_D^2} = \sqrt{\frac{2\epsilon_k x}{eE}}$$

In order to decrease  $\sigma$  one should decrease  $E_k$  and increase  $E$  in the drift region. Because the two quantities are not independent, one has to choose generally gases with small diffusion coefficients. Decreasing the maximum drift distance will obviously help too. However, it is not only the width of the electron distribution along the drift direction which determines the spatial resolution of the drift chamber. Depending on thresholds, noise and the sensibility of the electronics the drift time will be determined by the  $m^{\text{th}}$  fastest

electron. Therefore the maximum precision will be given by the mean of  $m$  electrons and the width will be reduced by a factor  $1/\sqrt{m}$

$$\sigma = \frac{\sigma_{DIFF}}{\sqrt{m}}$$

### 3.7 Determination of the coordinate along the anode wire

The charge from the avalanche will be deposited on the anode wire at the point  $x$ . The anode wire can be considered as a transmission line with distributed resistance, inductance and capacitance. The signal travels along such a transmission line through electric diffusion and electromagnetic wave propagation. The relative importance of each mechanism depends on the parameters of the line. Electric diffusion dominates, if the total ohmic resistance  $\ell R$  of the anode is larger than the critical resistance  $\ell R_c = 2\pi\sqrt{L/C}$ .

If  $\ell R < 2\pi\sqrt{L/C}$ , the electromagnetic wave propagation dominates. Looking at the signals at both wire ends one can determine the coordinate  $x$  by measuring the difference in arrival time of the two signals or comparing their charges. Both methods need appropriate electronics, a detailed discussion of the time method is given in [26]. Here the charge division method will be discussed. It can be shown, that the ratio of the charges at the wire ends depends only on the resistance ratio and not on the capacitance and the inductance of the line [27]. The ratio of the charges can therefore be written as a function

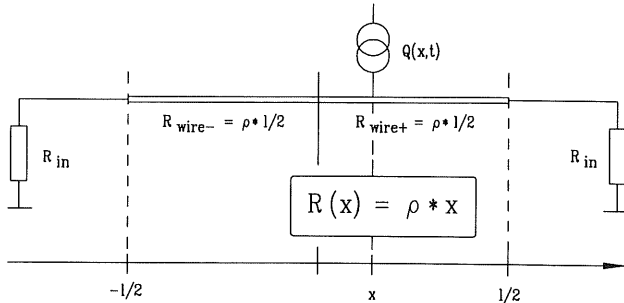


Figure 3.13: Illustration of the charge division mechanism.

of  $x$ , as

$$\frac{Q_+}{Q_-} = \frac{R_-}{R_+} = \frac{R_{wire-} + \rho x + R_{in-}}{R_{wire+} - \rho x + R_{in+}}$$

where  $\rho$  is the resistance of the wire per unit length. The distance  $x$  is then given by

$$x = \frac{1}{\rho} \frac{Q_+(R_{wire+} - R_{in+}) - Q_-(R_{wire-} + R_{in-})}{Q_+ + Q_-}$$

Ignoring any difference in the wire resistance and the input resistance of the amplifiers at each wire end the equation may be written as

$$x = \frac{R_{Total}}{2\rho} \frac{Q_+ - Q_-}{Q_+ + Q_-} = \frac{L}{2} \left( \frac{L_{eff}}{L} \right) \frac{Q_+ - Q_-}{Q_+ + Q_-}.$$

With  $R_{Total} = R_{wire} + 2R_{in}$  and  $L_{eff}/L = (R_{wire} + 2R_{in})/R_{wire}$ . The effect of the amplifier input resistance  $R_{in}$  on the charge precision can be considered by taking the derivative of  $x$  with respect to  $Q_+$  and  $Q_-$  respectively

$$\frac{dx}{dQ_+} = \frac{R_{Total}}{2\rho} \frac{Q_-}{(Q_+ + Q_-)^2}.$$

The relation shows that the error in  $x$  can be minimized by setting  $R_{in}$  as low as possible. Increasing the wire resistivity will lead to a larger rise time of the pulse and causes therefore a degradation of the drift time measurement. In the experimental environment the measured charges depend on the gain  $g_i$  of each electronic channel. Also the effective wire length  $L_{eff}$  will not correspond to the theoretical value. With  $Q_+ = g_+ Q_{sig+}$ ,  $Q_- = g_- Q_{sig-}$  and  $g_{rel} = g_-/g_+$  the equation becomes

$$x = x_0 + \frac{L}{2} \left( \frac{L_{eff}}{L} \right) \frac{Q_{sig+} - g_{rel} Q_{sig-}}{Q_{sig+} + g_{rel} Q_{sig-}}.$$

Where the calibration constants  $L_{eff}^i$  and  $g_{eff}^i$  have to be determined for each single wire experimentally. Obviously the charges  $Q_+$  and  $Q_-$  will be equal for a signal collected at the wire center. The smallest signals will result from the charge collected at the end of the signal wire, since one signal has to travel the whole wire length. The minimal charge needed for a signal to be seen is given by the actual thresholds of the electronics. The dynamic range can be calculated from

$$DR = \frac{Q_+}{Q_-} = \frac{R_{wire-} + \rho x + R_{in-}}{R_{wire+} - \rho x + R_{in+}}$$

assuming that  $R_{in} = R_{in+} = R_{in-}$  and  $R_{wire+} = R_{wire-} = R_{wire}/2 = \rho l/2$ , with  $x = l/2$  follows

$$DR = \frac{Q_+}{Q_-} = \frac{R_{wire-} + R_{wire+} + R_{in}}{R_{in+}} = \frac{R_{wire} + R_{in}}{R_{in}}.$$

The total signal charge is then

$$Q = Q_+ + Q_- = Q_-(2R_{in} + R_{wire})/R_{in}.$$

Given a threshold charge  $Q_{min}$  for a signal to be detected, the total charge depends on the ratio of the wire and the amplifier input resistance as illustrated in Figure 3.14. Increasing the amplifier input resistance (or lowering the wire resistance) will make the necessary total signal charge smaller. Therefore the detector can be operated with a lower gas gain, this is an advantage in an environment with bad background conditions. On the other hand one will loose in charge division resolution, which is shown in Figure 3.15.

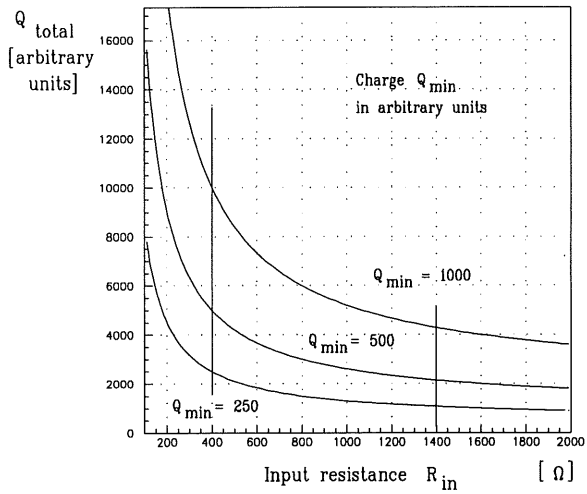


Figure 3.14: Signal charge versus input resistance.

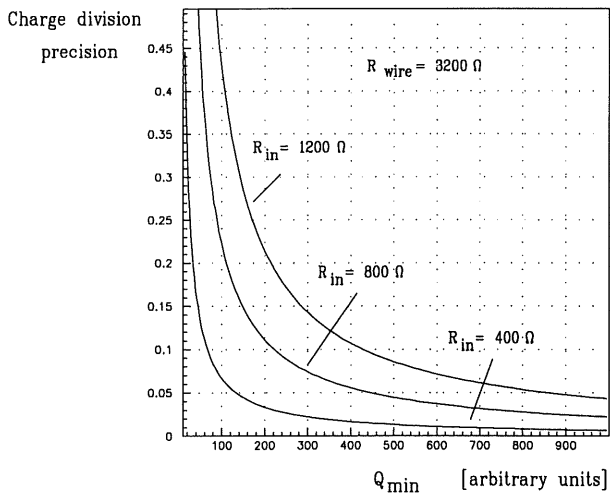


Figure 3.15: Charge division resolution versus input resistance.

## 4 Design considerations for the inner z-chamber

### 4.1 Choice of the drift cell geometry

In its basic form, a single cell drift chamber consists of a region of moderate field, followed by a proportional counter (see Chapter 3). In large detectors multicell structures are used which enclose the interaction region as well as possible. In this case also the anode wire becomes necessarily part of the active volume and therefore it is not possible to obtain a constant field over the full drift cell. To form the desired electrical field configuration one has to arrange field shaping electrodes, wires or strips in a suitable way as shown in Figure 4.1. The multiwire drift chamber shown combines several single drift cells,

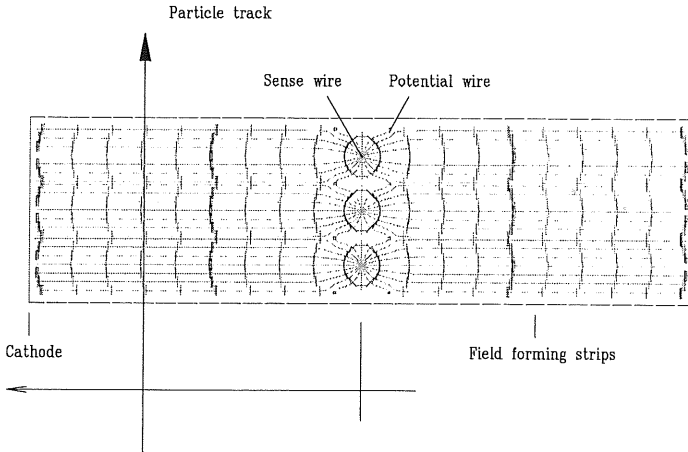


Figure 4.1: Layout of a standard drift cell.

where thin anode wires alternate with thick or potential wires. The latter strengthen the electrical field in the region where the electron multiplication takes place. In this scheme the drift field is given by the potential difference between the cathode voltage  $V_{cat}$  and the potential wire voltage  $V_{pot}$ . The electric field, which determines the drift velocity is then  $(V_{cat} - V_{pot})/\ell$ . The multiplication factor is regulated by the potential between the anode wire and the potential wires. In a standard arrangement like the one shown in Figure 4.1 the electric field which determines the multiplication factor and the drift field can be optimized independently because they are strongly decoupled. Generally one expects the optimum resolution for tracks crossing the cell parallel to the lines of constant drift time (isochrones), and reduced resolution for tracks crossing at other angles. At HERA the range of possible crossing angles for the inner z-chamber extends down to  $20^\circ$  in the

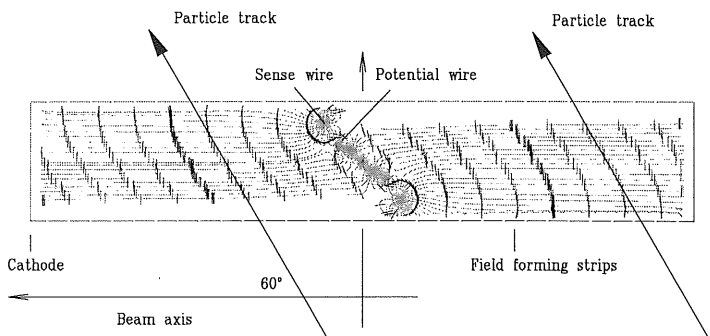
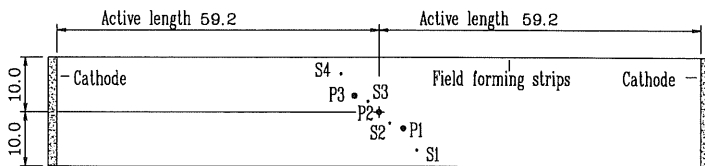


Figure 4.2: Layout of the CIZ drift cells.

forward and up to  $170^\circ$  in the backward region. Therefore a new wire arrangement has been chosen for this chamber (Figures 4.2 and 4.3). The wire planes are not normal to the beam axis as commonly used, but are tilted by  $45^\circ$ . That causes the isochrones to be tilted to  $30^\circ$  which improves resolution for the track crossing angles in forward direction. In the backward part of the chamber, a tilt in the opposite direction is required. The tilting also resolves the left-right ambiguity normally encountered in drift chambers. The



Wire positions [mm]

Potential wire 1 (P1)  $z = 4.5$   $y = -3.0$   
 Potential wire 2 (P2)  $z = 0.0$   $y = 0.0$   
 Potential wire 3 (P3)  $z = -4.5$   $y = 3.0$

Anode wire 1 (S1)  $z = 7.0$   $y = -7.0$   
 Anode wire 2 (S2)  $z = 2.0$   $y = -2.0$   
 Anode wire 3 (S3)  $z = -2.0$   $y = 2.0$   
 Anode wire 4 (S4)  $z = -7.0$   $y = 7.0$

Wire diameters

Potential wires  $120 \mu\text{m}$

Anode wires  $20 \mu\text{m}$

Figure 4.3: Geometrical layout of the CIZ drift cells.

field lines are distorted such that a track crossing the cell will usually give signals on only three of the four sense wires. Tracks crossing on the left side give signals on wires 0, 1, 2, while those on the right hand side give signals on wires 1, 2 and 3. The presence of a signal on either wire 0 or 3 identifies on which side of the wire plane the track crossed.

A single drift cell of the final chamber is 2 cm high and 12 cm long. The maximum drift distance varies from  $\sim 53$  mm to  $\sim 62$  mm depending on the wire. Sixteen cells are combined together forming a sixteen fold polygon in cross section with inner and outer radius of 173.5 mm and 199.5 mm respectively. The whole detector consists of 15 subrings of 16 cells.

## 4.2 Electrostatic simulations

Dedicated procedures to calculate the electric field and the potentials in wire chambers were developed, since these detectors became of interest. An general description of the problem is given in [28] and for the special case of proportional chambers in [29]. Mostly the programs are primarily designed for the use with chambers, which consist only of thin wires and infinite equipotential planes. Electrode planes and strips can only be handled by approximation, using an array of wires. They also can not deal with three dimensional structures. With the requirement, that the wires have an infinite length, the expressions for the electric field and the potential of a single wire become simple (see for example [21]). In this approximation the dipole and quadrupole terms are not considered, therefore the wire spacing in the simulation should be at least 5-10 times the wire radius. Today with the given computing power the Poisson equation can be solved more or less exactly, using a dedicated numerical method (finite elements, finite differences). Programs such as discussed in reference [30] treat the problems in three dimension and handle dielectric materials as well.

The simulation studies shown in this thesis, were done using the WIRCHA [31] and the GARFIELD [32] code, which both use the thin wire approximation. They perform a variety of informative tasks for designing a drift chamber, as:

- Plotting the electric field and the equipotential lines.
- Calculating and plotting of electron and ion drift lines and equal arrival time contours. The influence of the magnetic field on the behaviour of the electrons and ions can be simulated.
- Calculation of the  $x(t)$  relations. The programs can produce drift time tables, which may be later used in the reconstruction procedure.
- Signals induced by a charged particle, which traverses the drift cell, can be simulated. These then can be further used as input to an electronics circuitry simulation program (for example SPICE [33]).

Using both programs allows in addition to compare their results. Our goal was to arrive at a simple but optimum arrangement of the field shaping strips and potential wires in the drift cell.



### 4.2.1 Electrostatic simulation of the drift cell chosen

Figures 4.4 and 4.5 show the equipotential lines for a conventional geometry and for our design, respectively. Tilting the wireplanes causes a distortion of the equipotential lines

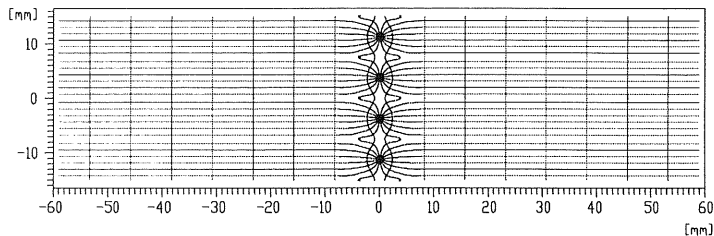


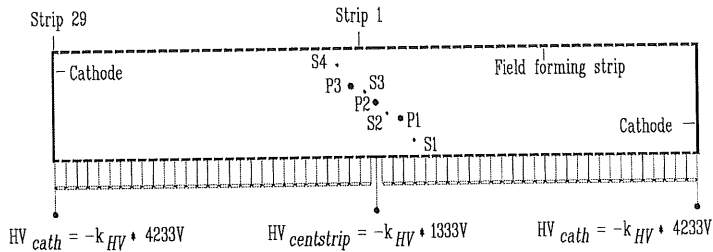
Figure 4.4: Electrostatics of a standard cell.

and also leads to a nonuniform distribution of the collected charge over the four wires. Figure 4.5 shows that about 60% of the field lines end on the outer two wires, numbered 0 and 3, while only about 20% end on the inner two, numbered 1 and 2. In particular, wire 0 collects charge only when a track crosses on the right side of the sense plane and wire 4 collects charge only on the left side whereas wire 1 and 2 collect charge from both sides. By positioning the three potential wires adequately the surface field for all sense wires was equalized, while also trying to maximize the area for charge collection. This requires, that all field lines coming from the drift region should end on a sense wire. Figures 4.7 and 4.8 show the absolute values of the field in the zone close to the wire for a standard cell and the chamber described.

### 4.2.2 The coupling between the drift field and the gas amplification field

One disadvantage of the tilted arrangement is that the cathode voltage which determines the drift field and the potential wire voltage are now strongly coupled. It is necessary to keep these two voltages always at a fixed ratio. This restriction prohibits an independent choice of both the drift field and the gas gain. Figure 4.6 shows the simulated electric field and equipotential lines, if the ratio is changed by 25%. Lowering the potential voltage will increase the area of charge collection seen by the inner wires but as lower the surface charge on the inner sense wires and therefore also the gas gain. If the voltage is too low the field lines start from the field strips as shown in Figure 4.8 and it is obvious that this prevents proper functioning of the drift cell. Changing the ratio in the opposite direction e.g. increasing the potential wire voltage would provide a higher gas gain because of the higher surface charge, but on the other hand the inner two wires will pinch off. For

$$\text{delta } HV_{\text{strip}} = -k_{HV} * 100V \quad HV_{\text{strip } i} = -k_{HV} * (1333V + i * 100V) \quad \text{for } i = 1, \dots, 29$$



Wire potentials

Potential wires     $HV_{\text{pot}} = -k_{HV} * 2000V$                                   Anode wires                                   $HV_{\text{sense}} = 0V$  ( ground )

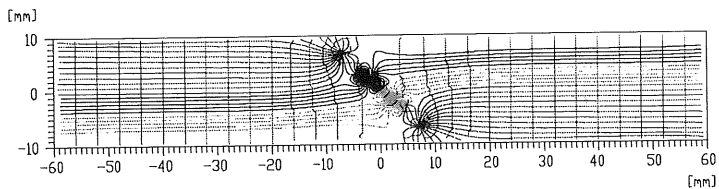


Figure 4.5: Electrostatics of a CIZ cell.

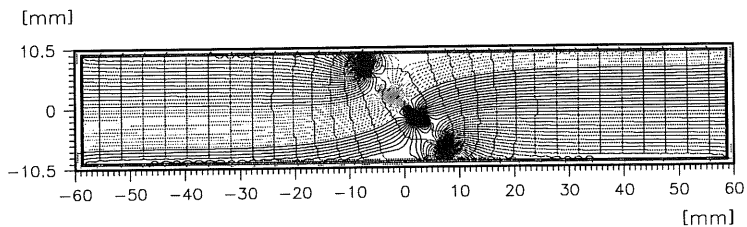


Figure 4.6: Field with low potential wire voltage.

$$z(E) = \text{Log}(E)/\text{Log}(E_{\text{max}}) - 0.5 \rightarrow E(z=1) = 0.7507E+10 \text{ V/m}$$

$$E(x = -10.0 \text{ mm}, y = 0.0 \text{ mm}) = 497.77 \text{ V/cm}$$

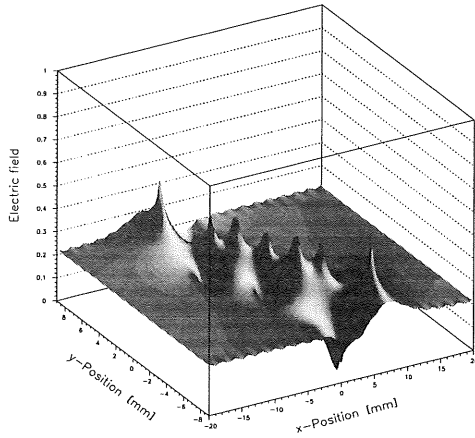


Figure 4.7: Field near the wires in the CIZ cell.

$$z(E) = \text{Log}(E)/\text{Log}(E_{\text{max}}) - 0.5 \rightarrow E(z=1) = 0.9483E+09 \text{ V/m}$$

$$E(x = -7.5 \text{ mm}, y = 0.0 \text{ mm}) = 971.26 \text{ V/cm}$$

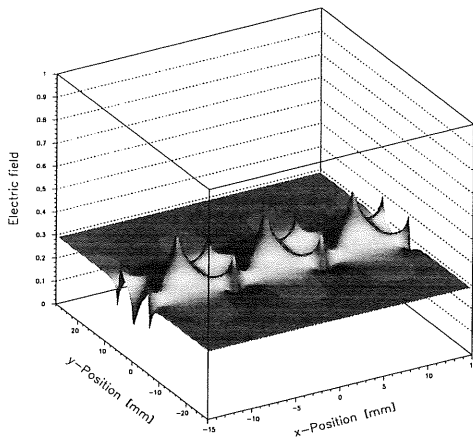


Figure 4.8: Field near the wires in a standard cell.

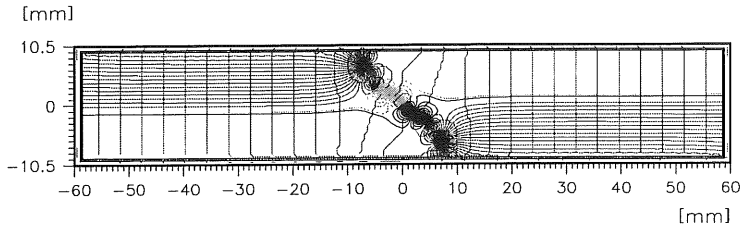


Figure 4.9: Field with high potential wire voltage.

larger distortion no charge would be seen at all on these wires. The optimum ratio is determined by equalizing the surface charge on all four sense wires in the drift cell to provide constant gas gain. The relation between the drift field  $V_{cat}$  and the gas amplification voltage  $V_{pot}$  is illustrated in Figure 4.10. If a specific gas gain for efficient

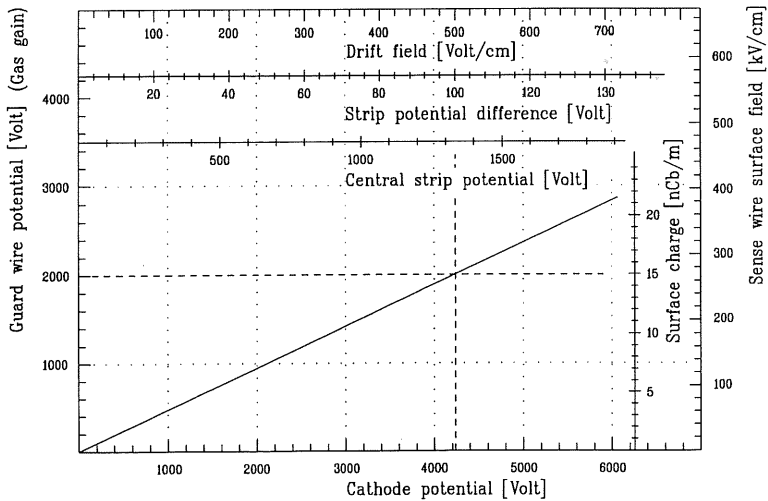


Figure 4.10: Relation between the applied voltages.

operation is required, the corresponding potential wire voltage has to be applied. The coupling, which is typical for this type of cell, now determines also the drift field and the voltage at the central field forming strip  $V_{centstrip}$  (see Figure 4.10).

potentials	decreased potential wire voltage		nominal ratio		increased potential wire voltage	
$V_{cat}$	4233V		4233V		4233V	
$V_{pot}$	1500V		2000V		2500V	
ratio $V_{cat}/V_{pot}$	2.82		2.12		1.69	
surface charge/field	charge nC/m	field kV/cm	charge nC/m	field kV/cm	charge nC/m	field kV/cm
anode wire 0	14.4	258	15.0	270	15.6	281
anode wire 1	12.6	226	14.7	264	16.9	303
anode wire 2	12.6	226	14.7	264	16.9	303
anode wire 3	14.4	258	15.0	270	15.6	281

Table 4.1: Sense wire surface charge and field for different voltage ratios.

#### 4.2.3 Influence of the field forming strip width

An optimum field configuration, e.g. homogeneous field, has to be achieved to guarantee a constant drift field over a large as possible drift volume. In order to obtain a relatively uniform field the drift cell is enclosed by two sets of field forming strips. They are connected to negative potential increasing from the center of the cell. By decreasing the width of the strips one improves in the uniformity of the field in the edge zone, also because the voltage steps become smaller. Figure 4.12 illustrates a section of the drift region with 4 mm pitch field forming strips (strip width 3.75 mm, gap 0.25 mm). The field distortions introduced reach up to a height of 4 mm, i.e. 20 % of the drift cell. Figure 4.12 shows the improvement achieved by reducing the strip width to 2 mm (strip width 1.75 mm, gap 0.25 mm). In the chamber the wires are strung perpendicular to the beam axis and are supported by 1 mm thick dividers, extending from the edges of the polygon. Reducing the width of the strips on these dividers will also reduce the distortions and consequently the dead zone in azimuth.

#### 4.2.4 Influence of double / single layered field forming strips

The strips described above do not entirely close the active volume of the drift cell. The rather moderate drift field may be influenced by external fields leaking through the gaps. Since the distances between parts on high potential and parts on ground potential are quite small in the geometry chosen, which was optimized for minimum radiation length, the electric fields between the field forming strips and ground foil are quite high. Especially near the cathode plane the potential difference is in the order of 5 kV/cm, considerably larger than the drift field of 500 V/cm. This external field will influence the drift field as shown in Figure 4.15. To avoid these distortions we use a second set of strips with the same pitch but offset by half a strip width. The outer layer strips are separated by a

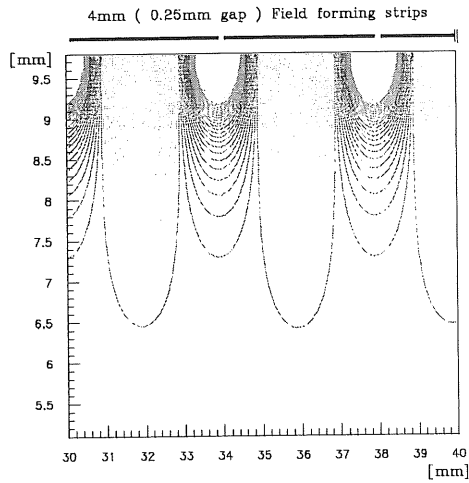


Figure 4.11: Contour plot of the field near the 4 mm wide strips.

$$z(E) = \text{Log}(E)/\text{Log}(E_{\text{max}}) - 0.5 \rightarrow E(z=1) = 0.1894\text{E}+09 \text{ V/m}$$

$$E(x = 32.5 \text{ mm}, y = 7.4 \text{ mm}) = 490.65 \text{ V/cm}$$

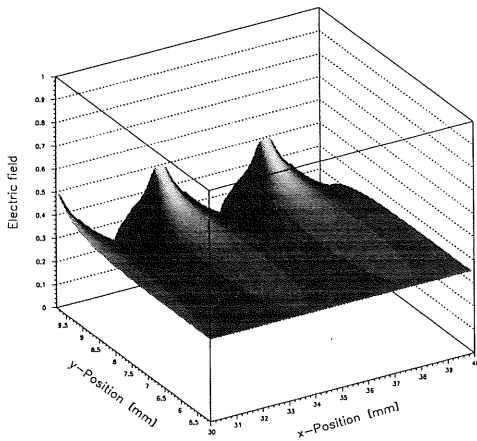


Figure 4.12: Field near the 4 mm wide strips.

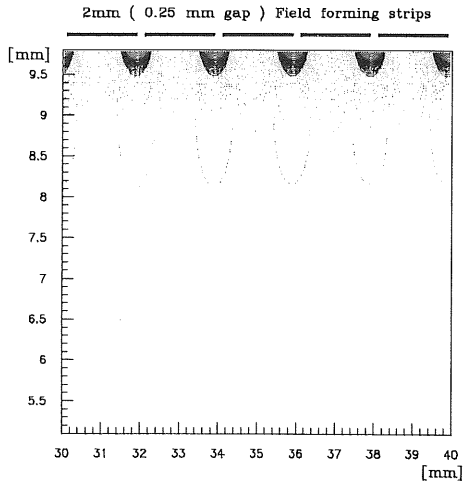


Figure 4.13: Contour plot of the field near the 2 mm wide strips.

$$z(E) = \text{Log}(E)/\text{Log}(E_{\text{max}}) - 0.5 \rightarrow E(z=1) = 0.6914\text{E}+08 \text{ V/m}$$

$$E(x= 32.5 \text{ mm}, y= 7.4 \text{ mm}) = 501.85 \text{ V/cm}$$

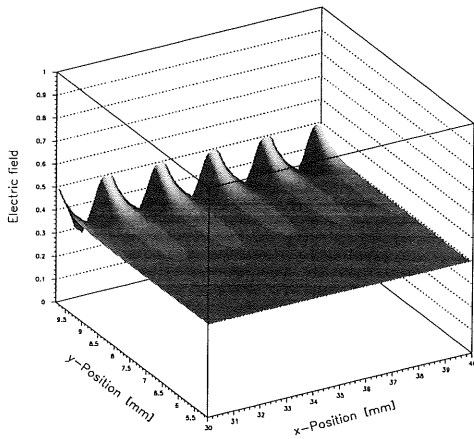


Figure 4.14: Field near the 2 mm wide strips.

$$z(E) = \text{Log}(E)/\text{Log}(E_{\text{max}}) - 0.5 \rightarrow E(z=1) = 0.1201E+11 \text{ V/m}$$

$$E(x = -0.9 \text{ mm}, y = 43.0 \text{ mm}) = 492.50 \text{ V/cm}$$

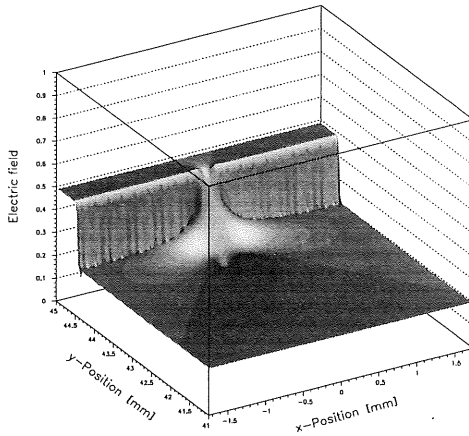


Figure 4.15: Field distortion near the gaps.

$$z(E) = \text{Log}(E)/\text{Log}(E_{\text{max}}) - 0.5 \rightarrow E(z=1) = 0.1045E+11 \text{ V/m}$$

$$E(x = -0.9 \text{ mm}, y = 43.0 \text{ mm}) = 499.40 \text{ V/cm}$$

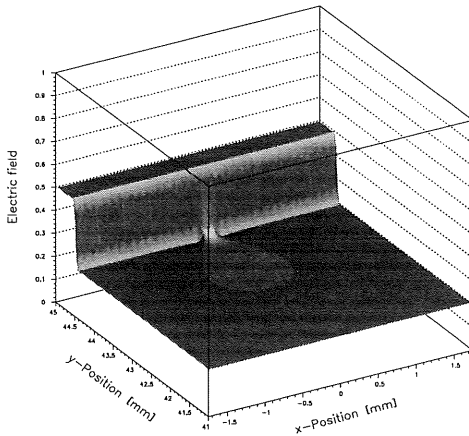


Figure 4.16: The field distortion using double layered strips.



20  $\mu\text{m}$  foil from the inner ones and therefore close the cell nearly hermetically. The field leakage is now negligible as apparent from Figure 4.16.

#### 4.2.5 Dependence of the electric field on mechanical tolerances

The homogeneity of the drift field depends on properly adjusted strip potentials. Distortions are tolerable if they do not influence the charge collection in the drift cell. The same holds for the gas gain of the chamber, which depends on the detector capacitance and hence on the geometry. Mechanical tolerances will therefore effect gain and drift field homogeneity. Figures 4.17 and 4.18 show the simulation of the electric field, where two or three field forming strips are shortened, and the potential step consequently becomes

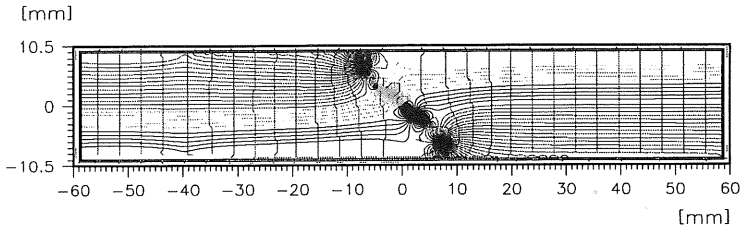


Figure 4.17: Influence of two shortened strips.

larger along the drift direction. The gradient  $\Delta V/\Delta z$  is lower in the region concerned but becomes larger elsewhere. In chambers built with minimum material and wall thick-

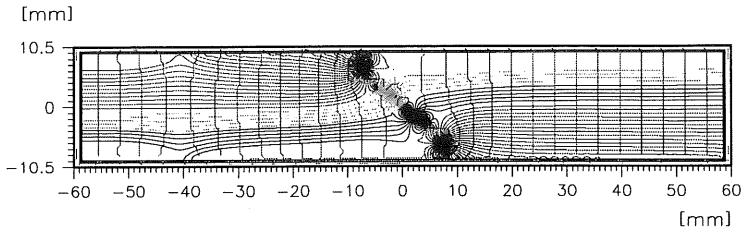


Figure 4.18: Influence of three shortened strips.

ness below 1 mm mechanical variations have to be expected, e.g. due to tolerances and differences in gas pressure between cells. To estimate these effects the electrostatics were simulated changing the position of the set of strips by 1 mm. The shape of the field lines shown in Figure 4.19 does not change much due to the 1 mm shift of the cover towards the cell center. This will therefore not prevent the drift cell from working properly. More

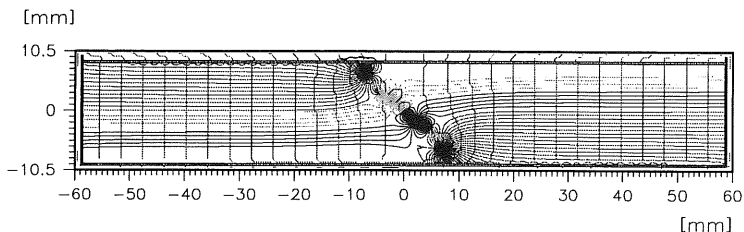


Figure 4.19: Field configuration, if the cover is moved by 1mm towards the center of the cell.

informative is the influence of a shift on the surface charge on the sense wires given in Table 4.2. A change in surface charge in the % range will influence the gas gain drastically, as can be estimated using the information given in Figure 4.28 below.

surface field	undistorted cell	cover moved out by 1mm		cover moved in by 1mm	
	field kV/cm	field kV/cm	$\Delta E$ %	field kV/cm	$\Delta E$ %
anode wire 0	269.5	262.1	2.8	283.3	5.1
anode wire 1	264.4	263.0	0.2	265.2	0.3
anode wire 2	264.4	264.4	0.0	264.5	0.0
anode wire 3	269.5	269.5	0.0	269.5	0.0

Table 4.2: Wire surface charge, if the cover is shifted by 1 mm. The first column contains the values for an undistorted cell.

## 4.3 Simulation of the drift lines and times

### 4.3.1 Choice of gas mixtures

The correlation between drift field and gas gain also restricts the choice of gas somewhat. The optimum gas mixture should reach the plateau, where the drift velocity depends little on the reduced electric field ( $E/p$ ) at  $E \sim 500$  V/cm for normal pressure. The corresponding voltage settings should provide a sufficient multiplication factor  $M$  to achieve good efficiency. The maximum drift distance (6.2 cm) and drift time ( $\sim 1.2 \mu\text{s}$ ) require a drift velocity for the above field setting of  $\sim 50$  mm/ $\mu\text{s}$ . The maximum drift time is mainly given by the length of the signal buffer of the fast analog to digital converter of  $2.5 \mu\text{s}$ . In practice, it is advisable to use only half of this range to resolve timing problems as the absolute time zero is not known precisely. Shorter drift times will reduce the dead

time of the system but on the other hand worsen the resolution because of the higher drift velocity. The maximum drift time is further limited by the length of the pipeline in the trigger system [34], which also includes information from this chamber. The longitudinal diffusion should obviously be as small as possible, but not larger than about  $300 \mu\text{m}/\sqrt{\text{cm}}$ . Since the detector is located only 18 cm away from the beam line in a relatively intense radiation environment good ageing properties are required.

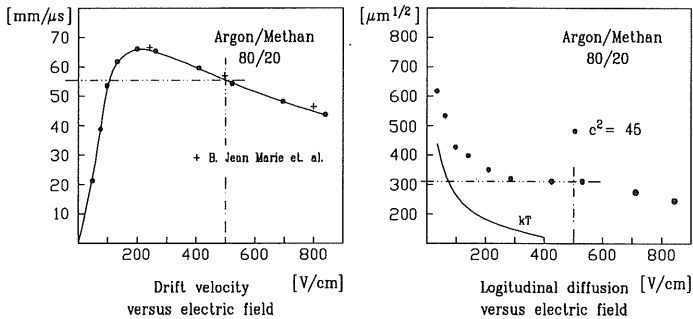


Figure 4.20: Drift velocity and diffusion (from [35]).

#### 4.3.2 Simulation studies without magnetic field

Simulation studies for the drift cell design were done with different suitable gas mixtures e.g.  $\text{Ar}/\text{CO}_2$  (96.7%/ 3.3%),  $\text{Ar}/\text{CH}_4$  (80%/20%) and  $\text{Ar}/\text{C}_2\text{H}_6$  (50%/50%). The drift lines and the isochrones for  $\text{Ar}/\text{CH}_4$  (80%/20%) are shown in Figure 4.21. Since the

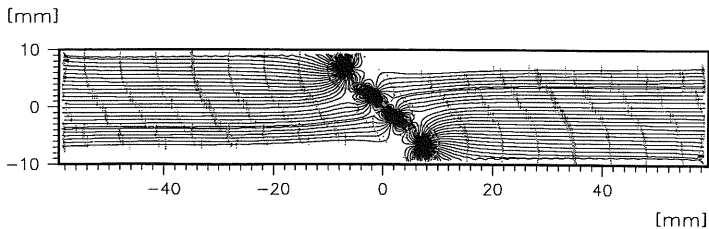


Figure 4.21: Simulated drift lines in a CIZ cell.

space time points calculated are later used in the track reconstruction to assign to a certain signal the corresponding point of primary ionization, the simulation needs to be

quite accurate. Figure 4.21 also shows that the shape of the driftlines varies between the inner and outer sense wires. Here our design again differs from a standard cell, where each sense wire is equal. In Figure 4.22 the drift distance is plotted against the drift time and the electric field for each wire type. Figure 4.23 shows the results for a standard drift cell for comparison. An important difference between the two designs is that the drift line in

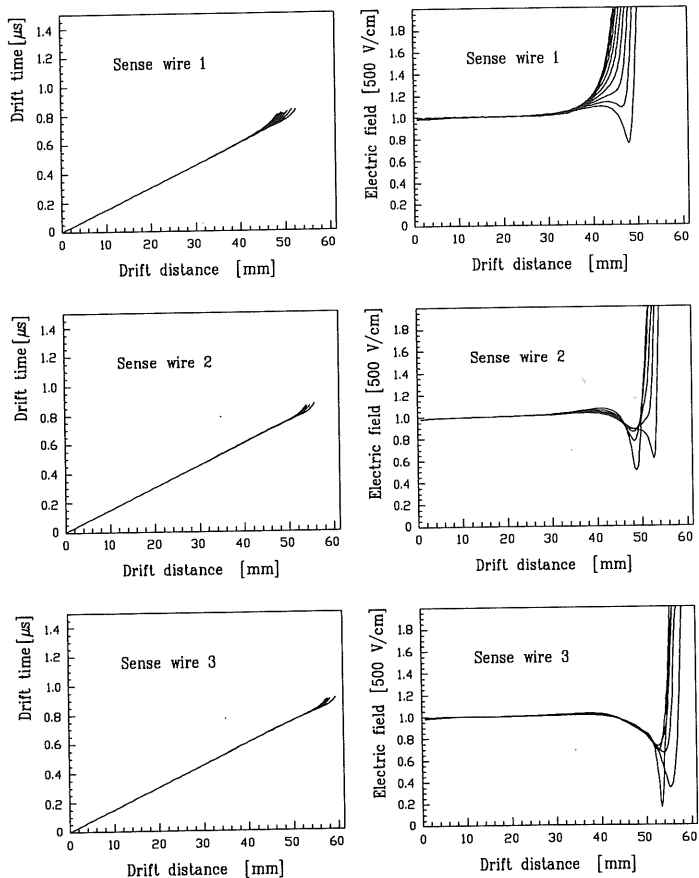


Figure 4.22: Drift distance versus field and time.

the center of the region associated to a given wire is curved, i.e.  $z = z(x, y)$ . The electric field, which determines the drift velocity is plotted in Figures 4.22 and 4.23 in function

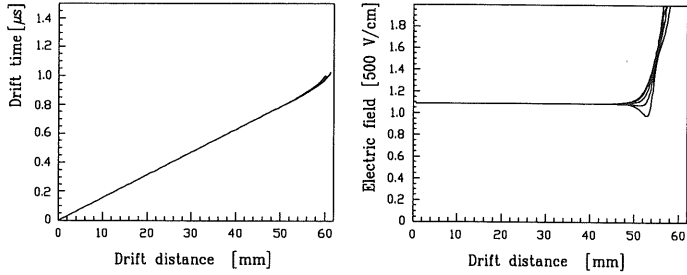


Figure 4.23: Drift distance versus field and time for a standard cell.

of the drift distance. Compared to the standard cell the variations near the sense wires are larger.

### 4.3.3 Influence of the magnetic field

The detector has to operate in a magnetic field of 1.2 Tesla with direction parallel to the beam axis. Figure 4.5 shows that in most parts of the drift cell the electric field is parallel to the magnetic field and therefore also the drift direction of the electrons (ions). But near the sense wire the field line change their direction with respect to the magnetic field direction. This will influence the shape of the drift lines as we know from Chapter 3.

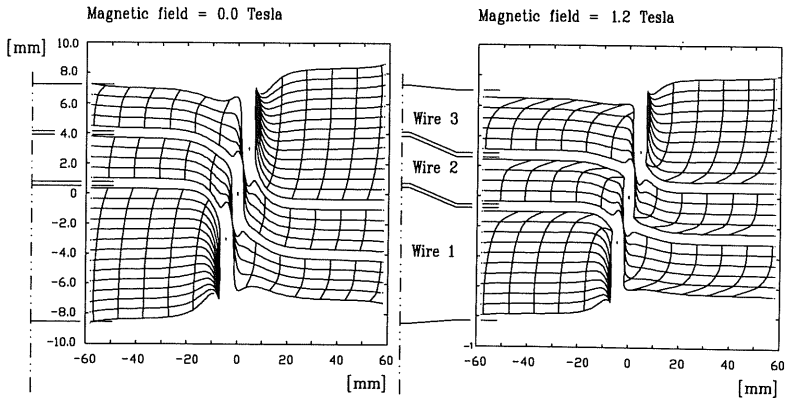


Figure 4.24: Influence of the magnetic field on the shape of the drift lines.

Knowing the cyclotron frequency  $\omega$  for the electrons and the mean time  $\tau$  between two

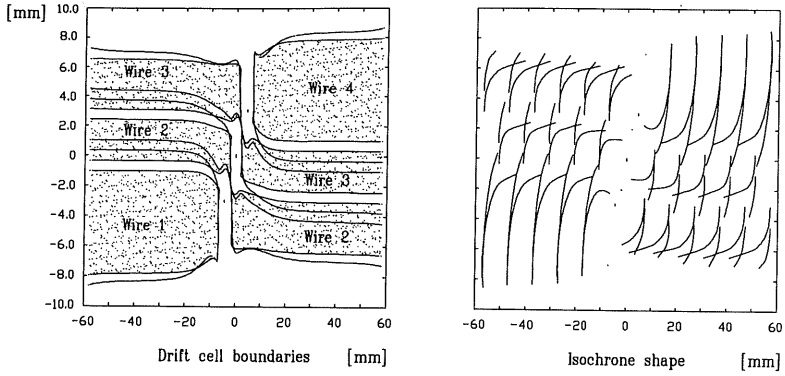


Figure 4.25: Drift region boundaries and isochrone shape, with and without magnetic field. Left: shaded region corresponds to field on. Right: stronger curvature for field on.

collisions in a given gas one can estimate the contribution from the three components to the drift velocity  $\vec{v}_D^e$ . The drift velocity  $\vec{v}_D^e$  in an electric and magnetic field is given by [16]

$$\vec{v}_D = \frac{\mu}{1 + \omega^2 \tau^2} \left( \vec{E} + \frac{\vec{E} \times \vec{B}}{B} \omega \tau + \frac{(\vec{E} \cdot \vec{B}) \cdot \vec{B}}{B^2} \omega^2 \tau^2 \right).$$

With the value for  $v_D^e$  from Figure 4.20 for the electric field of 500 V/cm in the drift region and the magnetic field of 1.2 Tesla we can estimate the influence of the magnetic field. Using the relation below we obtain for  $\tau$  and  $\omega$ :

$$\mu^e = \frac{v_D^e}{E} = \frac{e\tau}{m_e} \quad \tau = \frac{v_D^e m_e}{Eq}$$

$$\omega = 17.6 \times 10^{10} \text{s}^{-1} \text{Tesla}^{-1} \times 0.12 \text{ Tesla} = 2.1 \times 10^{10} \text{s}^{-1}.$$

With  $\tau \cong 7 \cdot 10^{-12} \text{s}$  for Argon / Methan (80%/20%) the component parallel to the magnetic field is

$$\left| \frac{(\vec{E} \cdot \vec{B}) \cdot \vec{B}}{B^2} \omega^2 \tau^2 \right| = E \cdot \cos \alpha \cdot 13.7$$

where  $\alpha$  is the angle between the direction of the electric field and the magnetic field. The component perpendicular to the plane formed by  $\vec{E}$  and  $\vec{B}$  becomes

$$\left| \frac{\vec{E} \times \vec{B}}{B} \omega \tau \right| = E \cdot \sin \alpha \cdot 3.7.$$

As long as  $\vec{E}$  is parallel to  $\vec{B}$  this component will be zero, while the parallel will be maximal for  $\alpha = 0$ . Following the electrical field lines towards the sense wire  $\alpha$  will

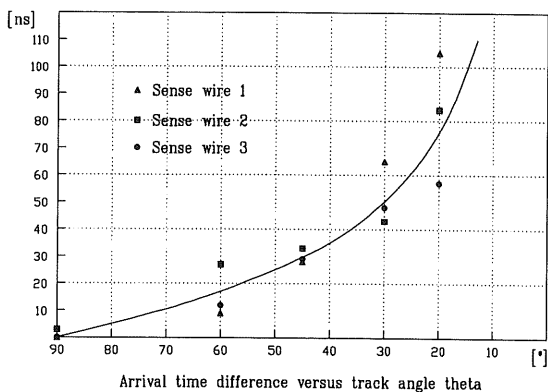


Figure 4.26: Influence of the magnetic field on the drift time.

become larger than zero and this will influence the shape of the drift lines as shown in Figure 4.24. It is also a consequence of the characteristic field shape for this cell designed that the drift regions of each sense wire will be shifted, if a magnetic field is present. The component of  $\vec{E}$  parallel to  $\vec{B}$  will direct the drifting electrons in the boundary zones towards a neighbouring sense wire region. This is illustrated in Figure 4.24, where the shaded regions represent the simulation with the magnetic field switched on. Figure 4.25 also shows an overlay of the isochrones for both cases. With the magnetic field on, the isochrones are bent stronger. The drift time of the first electrons produced by tracks with a polar angle of  $90^\circ$  will not change, because the isochrones lay on top of each other. But for smaller angles the drift time will vary due to the altered drift line shape. The result of a simulation for tracks under different angles is shown in Figure 4.26, where the difference between the drift times with and without magnetic field is plotted.

#### 4.4 Estimation of the gas gain

An important criterium for the design and use of a wire chamber is the gas gain, which depends on the counter geometry, operation voltage and the gas selected. To calculate the gas gain one may use one of several approximate analytical expressions (see [36, 37]), which are valid for the specific regions. Since the multiplication happens near the anode wire, we may assume the field to be cylindrical and then calculate it at a distance  $r$  ( $r < 100 \mu\text{m}$ ) from the surface charge on the wire given by the electrostatic simulation.

$$E(r) = \frac{C_\ell V_0}{2\pi\epsilon_0} \cdot \frac{1}{r} = \frac{Q_\ell}{2\pi\epsilon_0} \cdot \frac{1}{r}.$$

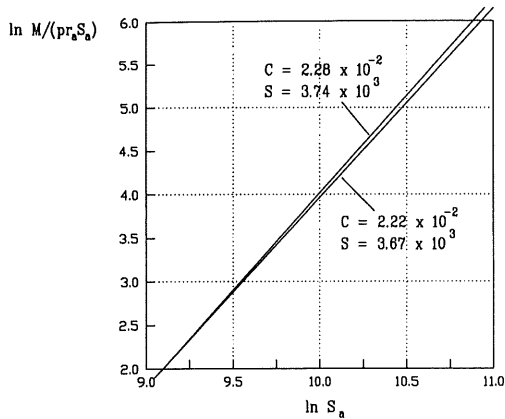


Figure 4.27: Multiplication factor from Charles [38].

Here  $C_\ell$  is the capacitance per unit length of the detector and  $Q_\ell$  the surface charge on the sense wire per unit length. The average energy  $\varepsilon$  obtained by an electron from the electric field between collisions is  $E/\alpha$ , where  $1/\alpha$  is the mean free path. Using the expression above one can calculate

$$\varepsilon = \frac{Q_\ell}{2\pi\epsilon_0 r} \cdot \frac{1}{kN\varepsilon} = \sqrt{\frac{Q_\ell}{\pi\epsilon_0 kN r}}$$

and

$$\alpha(r) = \sqrt{\frac{kNQ_\ell}{2\pi\epsilon_0 r}}$$

The multiplication factor can then be calculated, assuming that the avalanche multiplication starts at the critical distance  $r_c$  from the center of the wire. At  $r_c$  the electric field exceeds the critical value  $E_c$ , which is

$$E_c = \frac{Q_\ell}{2\pi\epsilon_0 r_c}$$

Introducing  $\alpha$  and integrating within the limits  $r_c$  and  $r_a$  one obtains the multiplication factor

$$M = \exp\left[2\sqrt{\frac{kNQ_\ell}{2\pi\epsilon_0}}\left(\sqrt{\frac{Q_\ell}{2\pi\epsilon_0 E_c}} - \sqrt{a}\right)\right] \quad \left(N = 2.69 \times 10^{19} \frac{P}{760 T} \text{ moles/cm}^3\right)$$

$k$  and  $E_c$  are specific to a given gas. Introducing the surface field in the expression above and replacing the constants by  $C_1$  and  $C_2$ , the multiplication factor becomes

$$M = \exp[E_A r_A (C_1 - C_2 / \sqrt{E_a})]$$



This is the formula given by Rose and Korff [39]. Measurements showed that different data are not in agreement with the above expression and therefore several modification of this formula have been suggested. In the notation of Zastawny [40] the expression can be written as:

$$\frac{\ln M}{pr_a S_a} = \int_{S_c}^{S_a} \frac{\alpha}{p} \frac{1}{S} dS$$

where  $S = E/p$ ,  $S_a$  the value for  $S$  at the anode radius  $r_a$  and  $S_c$  the value at the radius  $r_c$  where electron multiplication occurs. And for the gas gain we get for Rose and Korff

$$(\ln M)/(pr_a S_a) = C_1 - C_2/\sqrt{S_a}$$

and for Diethorn [41]

$$(\ln M)/(pr_a S_a) = C_3 \ln S_a - C_4 .$$

Other formulae have been suggested by different authors [36, 37] but for the estimates done below the Diethorn expression will be used. To estimate the gas gain in the drift cell

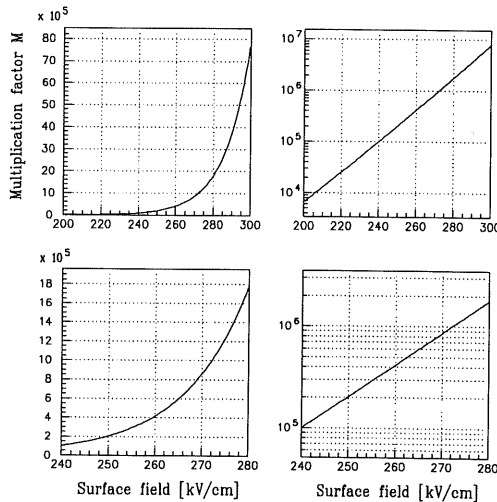


Figure 4.28: Multiplication factor versus the electric field.

the measured data for a mixture of 90% *Ar* and 10% *Methan* will be used. The constants can be taken from Figure 4.27, which yields  $\ln M/(pr_a S_a) = 2.22 \times 10^{-2} \ln S_a - 0.182$  where  $C_3 = 2.22 \cdot 10^{-2}$  and  $C_4 = 0.182$ . Thus the multiplication factor can be written as

$$\begin{aligned} M &= \exp[pr_a S_a (0.0222 \cdot \ln S_a - 0.182)] \\ &= \exp[r_a E_a (0.0222 \cdot \ln \frac{E_a}{p} - 0.182)] \end{aligned}$$

This function is plotted in Figure 4.28 for surface fields ranging from 200 - 300 kV/cm. For a given gas gain one can now estimate the corresponding electric field needed at the wire surface. Combination with the electrostatic simulation allows to estimate the necessary chamber potentials.

#### 4.5 Development of the signal

As discussed above the multiplication process begins at a few wire radii i.e. typically 50  $\mu\text{m}$  from the anode surface. The negative signal on the anode and the positive signal on the cathode result from the motion of the electrons and the ions. With a drift velocity of 50 mm/ $\mu\text{s}$  for the electrons near the anode wire the multiplication process will last less than 1 ns. The electrons will then have been collected on the anode surface and therefore

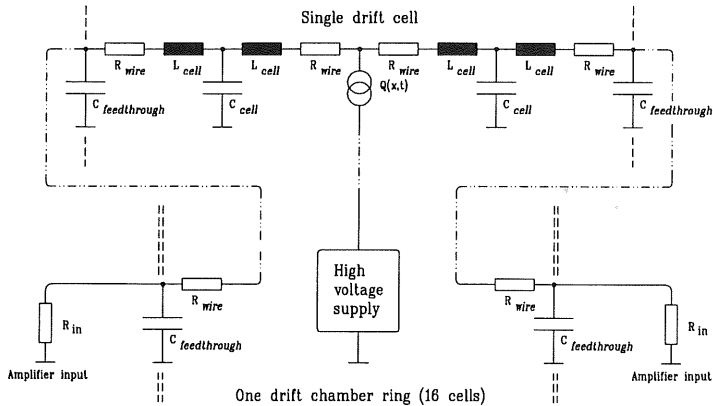


Figure 4.29: Circuitry representing one drift chamber ring.

not contribute much to the signal. The ions on the other hand have to reach the potential wires which are typically 2 mm away from the anode wire. Since their drift velocity is about a factor of 1000 smaller the necessary drift time exceeds 50  $\mu\text{s}$ . The expected signal for the different anode wires is shown in Figure 4.30. The simulation that led to this figure includes the primary ionization process, the drift of the electrons and the avalanche process assuming a multiplication factor of  $10^5$ . Because the electrons contribute only in the order of 1% to the signal, they are neglected and only the ion signal is plotted. The shape of the measured signal at the output will depend on the capacitance, inductance and resistance of the signal wire in the detector itself but also on the parameters of the subsequent electronics. A signal wire can be represented by the electronic circuitry shown in Figure 4.30. In this chamber the wire has to be supported at each edge of the polygon. The necessary wire feedthroughs contribute to the total capacitance of the system, too.

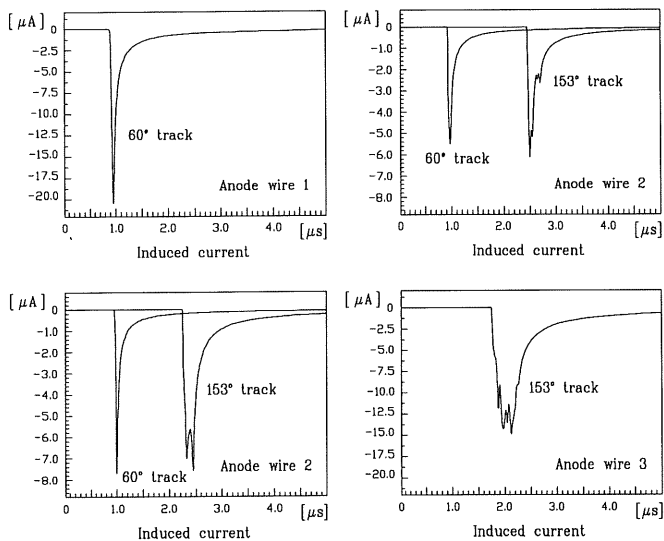


Figure 4.30: Induced current for the four wires in a CIZ cell for two different angles.

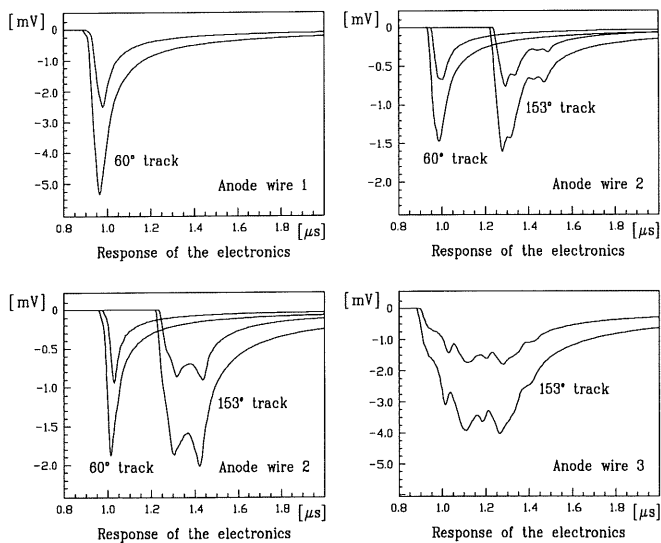


Figure 4.31: Simulated response of the signal electronics.

For the whole ring the single cell shown in Figure 4.29 has to be repeated. Simulated pulse shapes are shown in Figure 4.31. The measured chamber capacitance of 20 pF, an estimated inductance of 1.5  $\mu$ H and the sense wire resistance of 3.4 k $\Omega$  were used as input values for the circuitry simulation.

#### 4.6 Geometrical acceptance of the detector and simulated response

The drift chamber consists of fifteen 12 cm long rings along the  $z$ -axis, each of which is a regular sixteenfold polygon in cross section. It measures tracks with crossing angles  $\theta$  ranging from  $16^\circ$  to  $189^\circ$ , coming from an interaction region extending from -250 mm to +250 mm in  $z$  as illustrated in Figure 4.32. The distance of the center of the drift cell measured from the beam axis is 184.5 mm and the active cell height 20 mm. The 1.6 mm wide cathode rings reduce the active length to 118.4 mm. The dead zone along  $z$  resulting

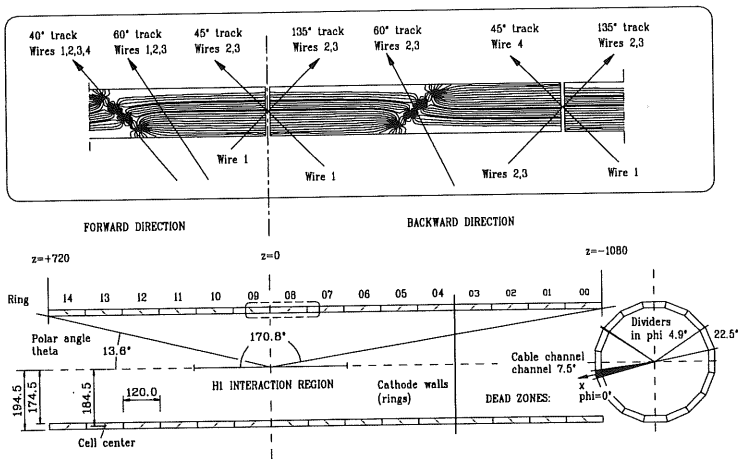


Figure 4.32: Geometrical layout and dead zones of the CIZ.

from the cell walls is 26 mm wide (1.6%). In azimuth the wire supports (thickness of 1 mm) introduce a dead zone at each cell edge of  $0.33^\circ$ . Since the field shape is distorted near the cell walls the total dead zone will however not only be determined by the cell construction. It will be enlarged because of inhomogenities in the electric field near the field forming strips and the wire feedthroughs. At  $\phi = 0$  a 23 mm wide cable channel is situated, which adds to the dead zone in  $\phi$ . These results are summarized in Table 4.3. Because of the wire arrangement it is a priori not clear which of the wires respond to

Dead zones of the CIZ		
dead zone in $z$ (cathode walls)	26 mm	1.6 %
dead zone in $\phi$ (readout channel)	7.5 °	2.1 %
dead zone in $\phi$ (wire support)	4.9 °	1.4 %
dead zone in $\phi$ (wire support+field)	14.4 °	4.0 %

Table 4.3: The values of the dead zones.

a track coming from the interaction region. Depending on the angle  $\theta$  and the position of the vertex the number of sensewires which produce a signal can vary between 2 and 4. Assuming the vertex at the origin (0,0,0) the response for the backward part of the

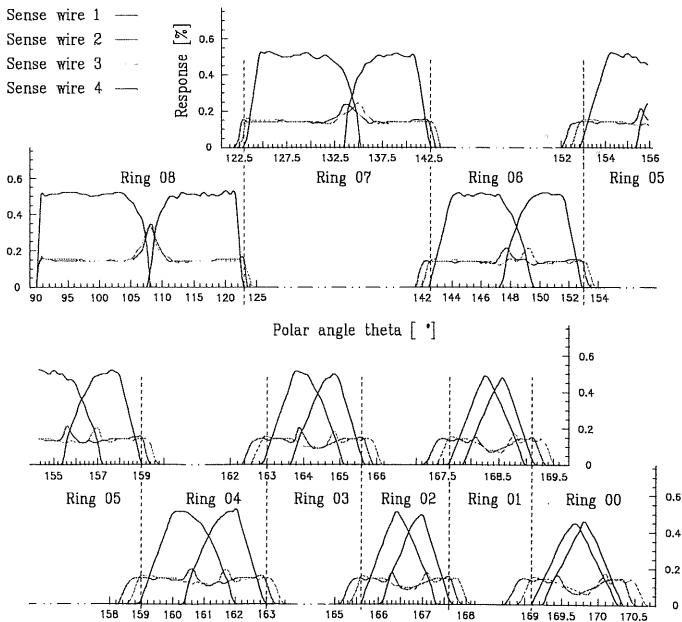


Figure 4.33: Acceptance of the different wires.

detector, which consists of 9 rings is plotted below as a function of the angle  $\theta$ . On the vertical axis the amount of drift region which is effectively crossed by a track is plotted

for each of the four sense wires. Obviously the detector is dead for tracks at  $90^\circ$  which hit a cathode ring and for tracks pointing to a dead region in  $\phi$ . Apart from that one expects at least signals from two wires (Figure 4.33). Tracks which cross the cell center near the signal wires, will lead to signals on all four wires. This then leaves the problem of the left right ambiguity unsolved. In the main drift region one expects three signals which immediately resolve the position in the cell. Near the boundary the inner two wire from neighbouring rings have an overlap that results in signals from both detector parts.

## 5 Construction of the drift chamber

### 5.1 Overview

The drift chamber is surrounded by the inner jet chamber whose carbon fibre wall is used for closing its gas volume (see Figure 5.2). The length of the full detector is 2200 mm reaching from  $-1030$  mm to  $+1080$  mm in the H1 coordinate system. As shown in Figure 5.1 the active region does not cover the entire length, since it starts only at  $-1080$  mm and ends at  $+720$  mm. Fifteen rings, each 12 cm long containing sixteen drift cells, are

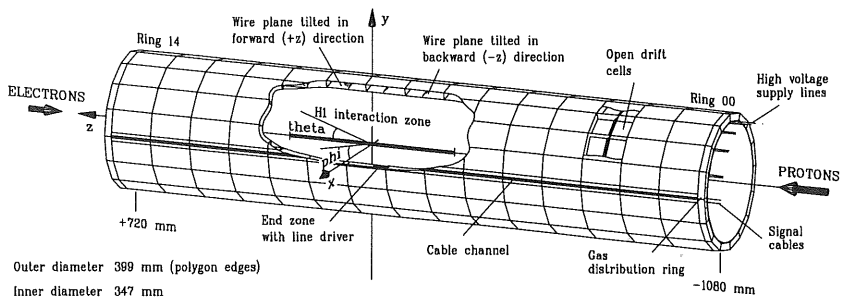
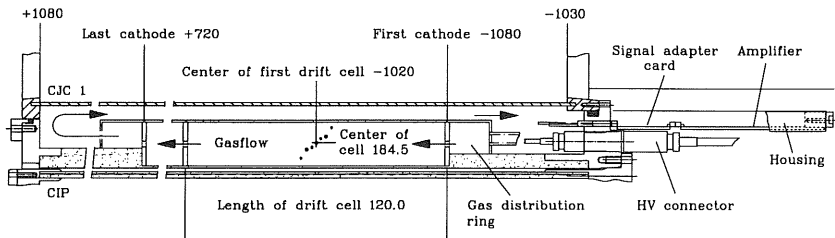


Figure 5.1: Sketch of the drift chamber.

arranged on a regular polygon. The independent rings are separated by printed circuit boards on each side serving as the cathode plane. These walls, the axial dividers extending from the corners of the polygon and the Kapton foil [42] with the field forming strips are glued to the chamber body. The cells are closed electrically with another foil identical to the one on the bottom which is glued to a removable cover. There are four anode wires and three potential wires running around the circumference in each ring. The wire planes in the backward part (9 rings) are tilted backward, the ones in forward direction tilted forward (6 rings). This construction was chosen to get an optimum resolution and to reduce the material as much as possible. The Rohacell cylinder [43], which supports the chamber body in the center, is extended axially towards the flanges, where the gas volume is closed. No further drift cells were added in forward direction, because this range is covered by the forward tracking detector, which has a good resolution for tracks with polar angles smaller than  $16^\circ$ . The inner and outer radii are 173.5 mm and 200 mm, respectively. If the performance of the central inner drift chamber had been the only design criterium, certainly a radially thicker chamber would have been built, allowing for more wires and thus greater redundancy. However, for optimum momentum resolution the minimum radius for the surrounding central jet chamber on the outside had to be taken as small as possible, while on the inside the beam pipe, space for a future vertex

detector and the trigger proportional chamber left little more room. The 28 mm overall thickness thought to be the minimum gap, in which a measurement of the  $z$ -coordinate would be achieved with some reliability. All the necessary high voltage connectors and



\* Remark : units in mm

Figure 5.2: Longitudinal cross section showing the flanges and the gas sealing.

signal amplifiers are mounted on the backward flange, which can be accessed within the detector without removing the whole tracker. This choice allows the removal of the innermost chambers in the parking position of the H1 detector, after the yoke has been opened and the backward calorimeter proportional chamber and the beam pipe have been taken out. Since the innermost chambers are exposed to the highest radiation, it is to be expected that they have to be serviced at shorter intervals than the outer chambers.

## 5.2 Mechanical aspects

### 5.2.1 Construction techniques

For the detector a laminar construction technique was used, starting from a removable steel mandril with an inner diameter of 347 mm corresponding to the chamber radius. The latter was manufactured from a steel tube, milled to a precision of  $25 \mu\text{m}$  over the full length, closed by end caps and equipped with small holes in its walls. These holes were used to stretch the different foils and the Rohacell foam layer on the mandril by evacuating the inner volume. The innermost layer consists of a  $25 \mu\text{m}$  Kapton foil with a  $5 \mu\text{m}$  coating of Aluminum for electrical shielding. To guarantee the electrical isolation towards the chamber cathodes the conducting layer is covered by a  $50 \mu\text{m}$  Kapton foil. On this sandwich a 6 mm thick Rohacell cylinder was glued using epoxy glue ( $20 \text{ g} / \text{m}^2$ ) [44]. The raw foam material had to be baked for 48 hours at  $180^\circ \text{C}$  to assume its final shape. The plates were then cut into 3 romboidal pieces covering the whole surface of the basic cylinder and again heated at  $180^\circ$  for 24 hours while held on a cylinder by Teflon bandages to loose all internal stress. The outer surface of the cylinder was then machined and polished to form sixteen flat surfaces whose cross section is a regular polygon. The



corner where the cable channel sits was then again machined to a flat surface. To bury the high voltage supply lines two 0.5 mm wide grooves were then milled at the fifteen remaining edges reaching from the  $-z$  end of the structure to the  $z$  position where the cathode supply lines had to be contacted later to the corresponding chamber parts. In the cable channel region fifteen parallel grooves were milled for the potential wire supply lines. Then Kapton shielded cables were put into these channels and fixed with epoxy-glu.

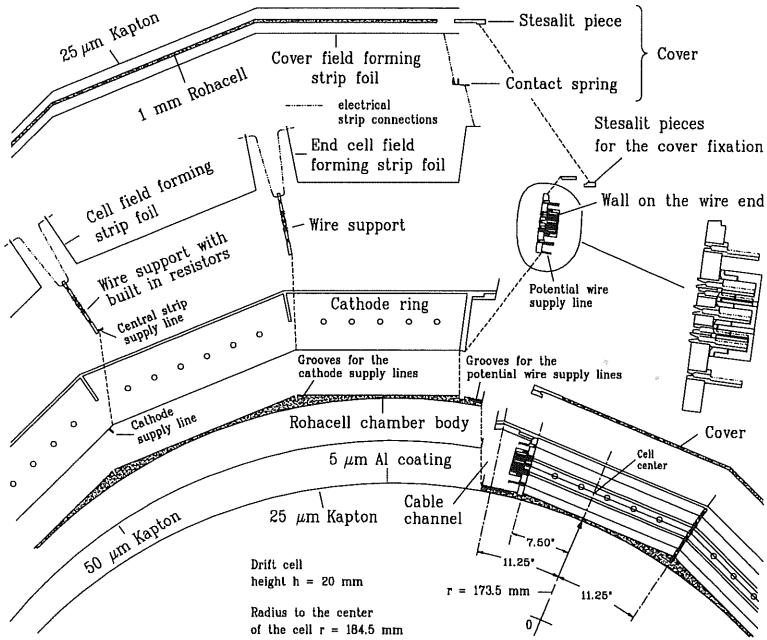


Figure 5.3: Cross section of the CIZ showing the single layers.

the next step precisely ( $\pm 10 \mu\text{m}$ ) positioned printed circuit board rings, 1.6 mm thick wide with  $5 \mu\text{m}$  Cu on each side, were glued to the basic Rohacell body. The cathode supply lines could then be soldered to the corresponding cathode planes. The axial dividers at each edge, including the ones at the readout channel, were then surveyed and positioned with a special tool in  $z$ ,  $r$  and  $\phi$  and then glued to the basic structure. Again using special tools the field forming strip foils were glued into these cells. Each strip was then contacted to the pads on the dividers (26550 solder points in total) through a 1 mm diameter hole. After glueing the gas rings onto the last cathode rings, and cutting the support tool to the desired length, the chamber end flanges were added. Connecting the high voltage supply lines to the connectors arranged around the backward flange in  $\phi$  completed the

basic chamber structure. The assembly was then carefully cleaned and all the connections were tested before the wiring of the detector started. All operations described above were carried out on a lathe equipped with an accurate ( $\pm 0.001$  mm) measuring system. The mandril was kept on the machine during the whole constructing procedure to guarantee the best possible precision. For the cover a similar laminar construction technique was

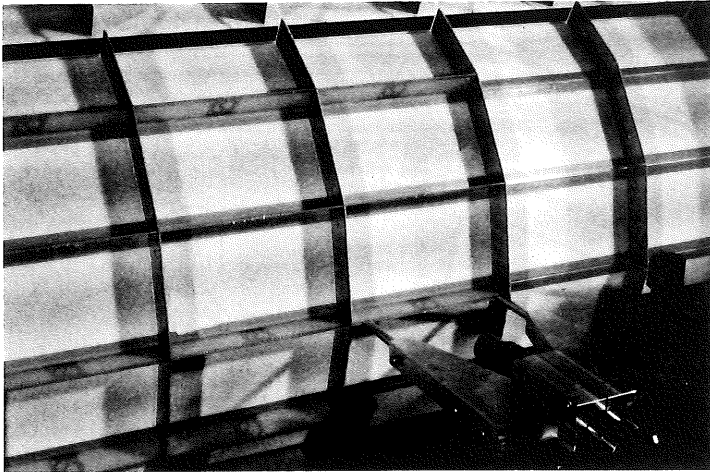


Figure 5.4: Photograph, showing the CIZ during construction on the lathe. With the tool the wire supports are precisely positioned, and then glued to the basic structure.

used. A  $25\ \mu\text{m}$  Kapton foil with the field forming strips on both sides was first equipped with the springs which provide the electrical contact to the bottom strips of the base structure after closing the cell. On a flat tool two end pieces, which consist of glass fibre reinforced epoxy [45] and are used to fix the cover, were then glued to both ends. This strip was now mounted on a mandril with the correct chamber dimensions, and the shape of the 16 fold polygon. The strip was baked with Rohacell pieces, which were already covered with glue on both sides, lastly topped with a  $25\ \mu\text{m}$  thick Kapton foil. The sandwich was then baked as a unit and pressed together, by covering the whole surface with an additional removable foil and evacuating on the inside.

The chamber was wired after it had been removed from the mandril and was installed on a device, where it could be rotated around its axis. The four signal wires ( $20\ \mu\text{m}$  Elgiloy [46]) and the three potential wires ( $120\ \mu\text{m}$  gold [47]) in each ring were then guided through the feedthroughs and soldered to the end pins at the cable channel. For the potential wire the originally foreseen copper beryllium wire could not be used because it was too rigid. The force necessary to straighten the wire over the corners of the cell

exceeded 1 N, which already led to a distortion of the thin chamber structure. A softer gold wire of the same dimension was used instead. Following advice from a goldsmith, we used a solder without lead in it, because the lead will react with the gold and the wire will break immediately. The wires were all strung with a tension of 0.2 N, which suffices for the longest unsupported length of about 7 cm.

### 5.2.2 Cell boundaries

The walls, which separate the cells axially, consist of 1.6 mm thick printed circuit board with  $5\ \mu\text{m}$  Cu serving as cathode plane. These components were precisely milled to an accuracy below  $10\ \mu\text{m}$  on a CNC (computer numerical controlled) machine. The holes which allow the gas flow along the chamber axis are arranged in the center of the cathode plane (Figure 5.5). The tenons along the outer circumference guarantee an exact positioning of the cover. Four different types of walls separate the cells azimuthally. The

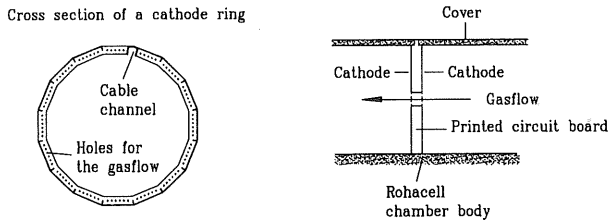


Figure 5.5: Cross section and longitudinal cut of an anode ring.

simplest version supports only the wires and stabilizes the chamber structure. It consists of a 1 mm thick triple layered printed circuit board. Since the field forming strips have to be interrupted near the wire plane, it is necessary to provide a connection between the different single strips on the inner layer. The pins on the outer two layers, later connected to the field forming strips, are plated through. This finally ties all cells belonging to a single ring together. During the manufacturing of the printed circuit boards two precise ( $10\ \mu\text{m}$ ) holes are drilled which later serve as reference positions. The holes for the wire feedthroughs [48] were drilled on the CNC machine. The feedthroughs themselves are then pressed into the board with a special tool. The wall on the wire end consists of a 2 mm thick triple layered printed circuit board. A lefthand and a righthand version is required because of the tilted wire arrangement. The pattern on the inside of the cell is similar to the one described above, including the inner layer. On the outside the wire end feedthroughs are connected to the signal line and to the high voltage supply line for the potential wire. The end pins are pressed into prepared holes and then soldered to the conducting strips. Finally the surface is covered with a  $25\ \mu\text{m}$  Kapton foil. The signal wire and the potential wire pins are insulated against each other with a cover (Figure

5.6) made out of Vespel [49]. At its base the cover and the foil are glued to the board with epoxy glue by pressing them together with a tool and left in the oven at 80° for one hour. The third type of divider (Figure 5.7) is identical to the first one except that 10

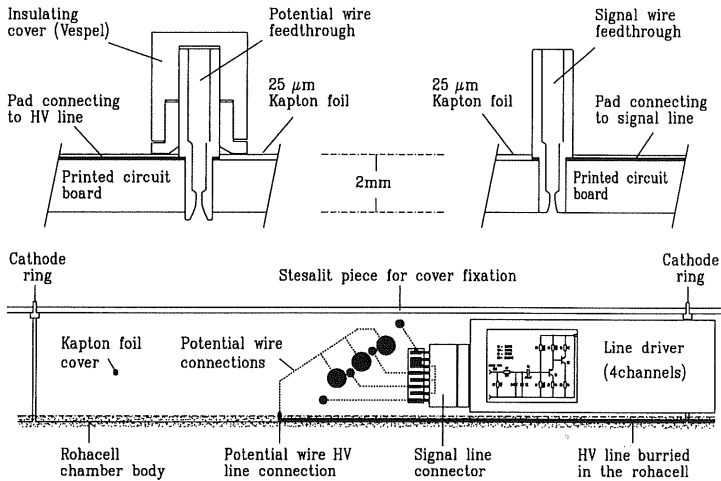


Figure 5.6: Wall on the wire end.

MΩ resistors ( $1.25 \text{ mm} \times 2 \times 0.5 \text{ mm}^3$ ) are embedded in the printed circuit board to save space and reduce the deadzone. For safety two resistors are put in parallel. The resistor chain supplies each field forming strip with the right potential, starting from the cathode towards the center strip. These dividers are located in the chamber structure at the point on the base cylinder, where the cathode supply lines of the corresponding ring end.

### 5.2.3 Field forming strip foil

Two different kind of foils were manufactured [50], short ones glued into each cell and long ones covering the top of the cell around the circumference. Both are double layered to limit field distortions near the gaps and have the same pattern. The basic material is  $25 \mu\text{m}$  Kapton with  $20 \mu\text{m}$  Cu on both sides. As indicated in Figure 5.8 each fieldshaping electrode is 1.75 mm wide and separated from the next by 0.25 mm. The electrode pattern is repeated on the back side of the foil, offset by 1 mm. For the cell foils two opposite strips are contacted through the foil at two points by a technique used in manufacturing multilayered printed circuit boards. This technique requires a thicker copper layer near the contact point for better qualities. To reduce the strip thickness elsewhere to less than  $10 \mu\text{m}$  without destroying the contacts these points were covered by a foil, when the

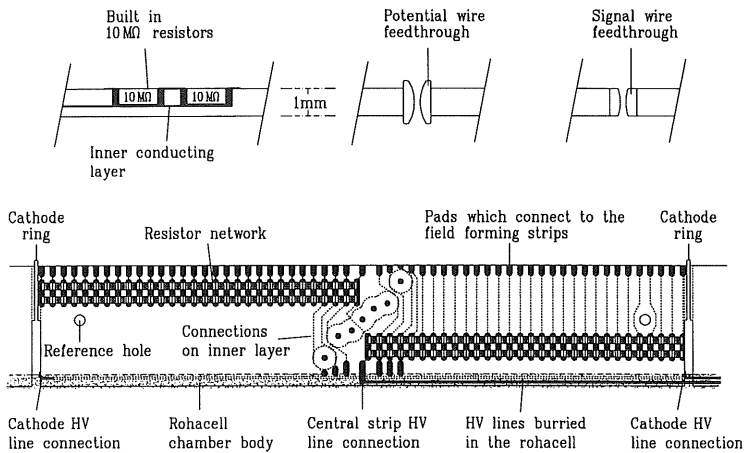
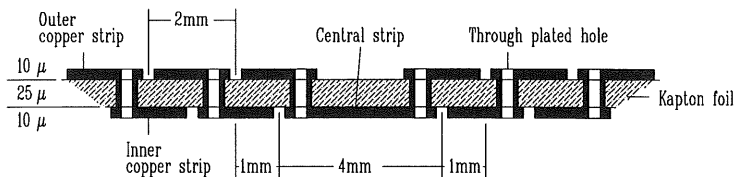


Figure 5.7: Wire support with built in resistor chain.

Cell foil



Cover foil with contact spring

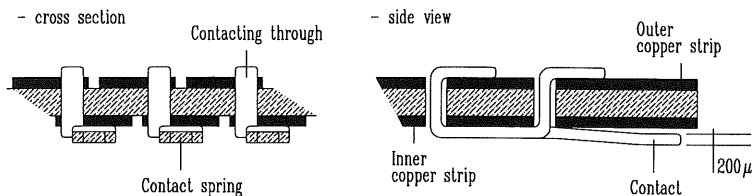


Figure 5.8: Field forming strip foil. The upper picture shows the cell foils with the contacting through, which connects the opposite strips. In the lower picture the cover foil with the contact springs, which perform also the connection, is illustrated.

thickness of the Cu layer was reduced by chemical edging to less than 10  $\mu\text{m}$ . The contact to the strips in the top corner is provided by springs. To avoid oxydation all copper strips are coated with 0.1  $\mu\text{m}$  gold.

### 5.3 Detector parameters

The mechanical parameters and the thicknesses measured in radiation length are summarized in Table 5.1. To enlarge the active thickness in  $r$  as much as possible and keep the

Mechanical properties of the CIZ		
active length $\Delta z$	mm	1800
active zone starts at $z$	mm	-1080
mechanical length $\Delta z$	mm	2254
total length $\Delta z$ <sup>[1]</sup>	mm	2467
thickness $\Delta r$ <sup>[2]</sup>	mm	20
chamber starts at $z$ <sup>[2]</sup>	mm	-1373
inner diameter	mm	347
outer diameter	mm	400
number of drift cells (rings) in $z$		15
number of $\phi$ -sectors		16
number of sense wires per ring		4
number of potential wires per ring		3
mean wire length	mm	1120
drift cell length $\Delta z$	mm	120
maximum drift distance $\Delta z$	mm	61.25
sense wire material		Elgiloy <sup>[3]</sup>
sense wire resistance	k $\Omega$ /m	3.0
sense wire diameter	$\mu\text{m}$	20
potential wire material		Au <sup>[4]</sup>
potential wire diameter	$\mu\text{m}$	120
wire tension	N	0.2
dead zone in $\phi$ (readout channel)	$^\circ$ (%)	7.5 (2.1)
dead zone in $\phi$ (wire support)	$^\circ$ (%)	20.2 (5.6)
dead zone in $z$ (cell walls in active zone)	%	1.6
radiation length in active zones	% $X_0$	0.6
radiation length averaged	% $X_0$	1.2
total weight	kg	8.16
mean density	g/cm <sup>3</sup>	0.11

Table 5.1: Mechanical properties of the CIZ.

<sup>[1]</sup> Incl. preamplifiers; <sup>[2]</sup> gas volume;

<sup>[3]</sup> see [46]; <sup>[4]</sup> see [47].

mass low the CIZ uses the inner carbon fibre wall of the CJC for closing its gas volume. The flanges are sealed with O-rings as shown in Figure 5.2. To avoid axial stress and a torsion of the cylindrical drift chamber only the backward flange is bolted to the CJC, while the forward part may slide by small amounts to account for differences in thermal expansion between the two chambers. For the required resolution of  $300 \mu\text{m}$  in  $z$  the signal wire position should be maintained positioned with an accuracy of  $100 \mu\text{m}$ . The feedthrough position was measured with an accuracy of  $10 \mu\text{m}$ . The inner diameter of the feedthroughs is  $200 \mu\text{m}$  which then automatically guarantees the required accuracy for the  $20 \mu\text{m}$  diameter sense wires. The longest unsupported length is  $7 \text{ cm}$  and the wires

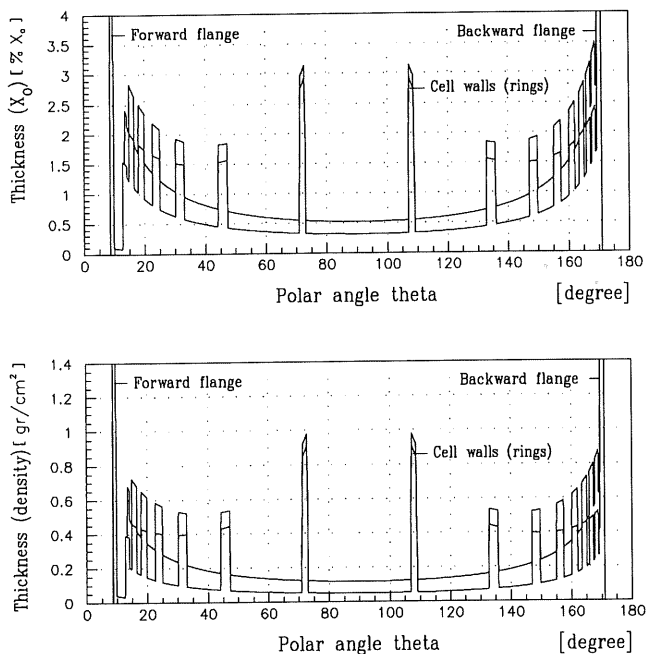


Figure 5.9: Radiation thickness, the lower curves show the values for tracks, which do not hit any cell boundaries in  $\phi$ . The higher values include the  $\phi$  dividers and the material in the cable channel, smeared around over  $2\pi$ .

are strung with a mechanical tension of  $0.2 \text{ N}$ . Therefore the wire displacement caused by electrostatic and gravitational forces is negligible. The total mass of the detector is  $8.1 \text{ kg}$  which gives the mean density of  $0.11 \text{ g/cm}^3$ . The radiation thickness for particles with a vertex at  $z = 6 \text{ cm}$  is plotted in Figure 5.9 in function of the polar angle  $\theta$ . Two

curves are shown, one for the case that the particle does not hit an azimuthal divider wall, and a second curve assuming that the material in these walls and the cable channel is averaged in  $\phi$ .

## 5.4 Gas system

The CIZ is flushed with premixed gas. In the open loop circuit the gas flow and composition is controlled automatically. Especially the pressure of the fragile detector needs to be controlled carefully, because otherwise the cell geometry will be influenced by large variations in pressure. In the first part of the circuit the gas composition is analysed and the flow and pressure are controlled. This part is located in a gas control room on the first underground floor of the H1 experimental hall. The pressure transmitters and the solenoid safety valves (powerless open) are located near the detector at the chamber level in a gas distribution rack. A diagram of the circuit is shown in Figure 5.10. The static pressure relative to atmosphere is measured at this position with highly sensitive pressure sensors in the  $\mu\text{bar}$  range. To hold the chamber pressure during operation within adjustable tolerances of about  $\pm 100 \mu\text{bar}$ , the solenoid valves (*SV1 - 2* and *SV1 - 3*) will be either closed or opened depending on the actual pressure conditions. The hydrostatic pressure resulting from the 28 m height difference is reduced by the membrane pump (*CP1 - 1*) which sucks the chamber gas out and vents it to the atmosphere. A complete analysis of the gas composition is performed by an automatic gas chromatograph station, routinely switched into the circuit. Independent of the use of calibration gases this instrument gives the different gas portions to an accuracy of  $\pm 2\%$  of the measured value with an overall sensitivity of about 300 ppm [51, 52]. Alcohol or water is added by passing the chamber gas over a bath of the corresponding cooled or frozen liquid. The reservoir is installed in a refrigerator where the temperature can be controlled within a certain range. The amount of the additive is then adjusted by varying the bath temperature and consequently the vapor pressure [53].

The electronic control system is integrated in a *VME* system with the necessary resources for monitoring, logging and control equipment. The instantaneous values of all analog outputs of the measuring devices, especially those for pressure and temperature are controlled with a set of suitable parameter allowing variations only within certain limits. If one of the relevant parameters is exceeded warnings or alarms are generated. In the case of an alarm the system is stopped and the high voltage of the detector is switched off via the hardware alarm (see slow control) interlock system. A computer independent hard wired logic protects the chambers against malfunctioning of the program or other unforeseen accidents. In this case the solenoid valves (powerless open) in the distribution rack connect the chambers with an argon flushed reservoir at atmospheric pressure at the detector level. A serial link provides the information on the current situation to the slow control system and the central data acquisition.



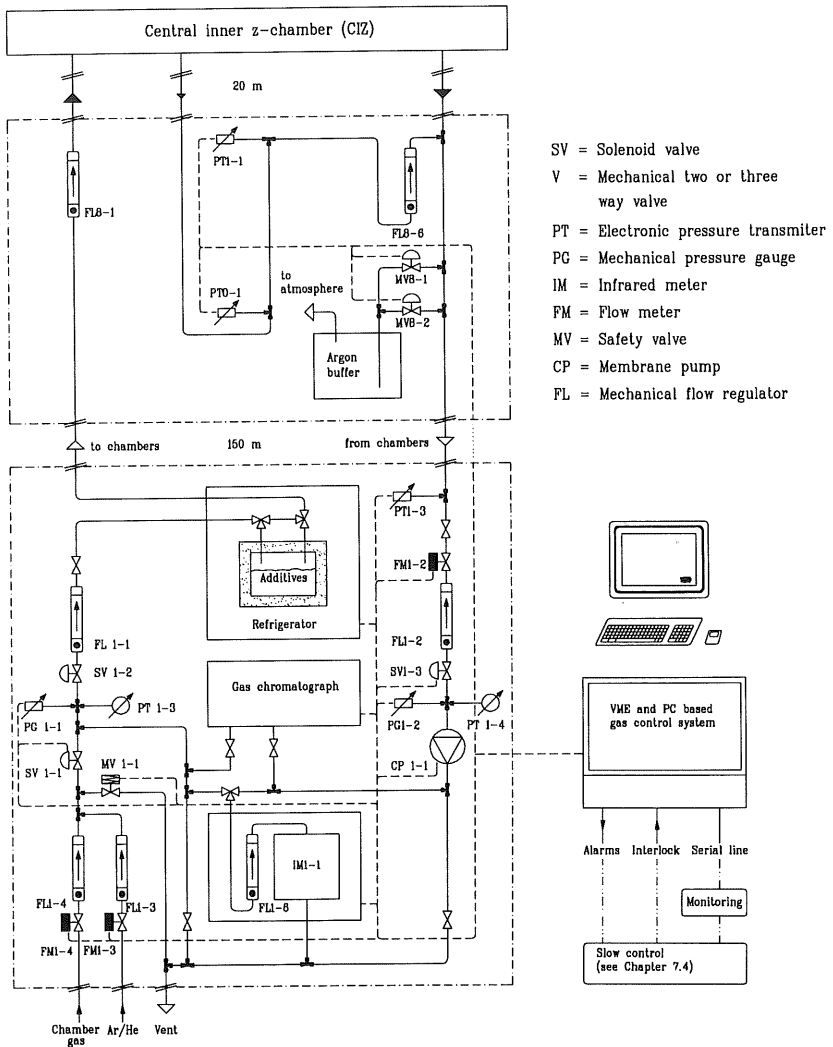


Figure 5.10: Sketch of the gas system.

## 6 Electronic

### 6.1 The high voltage system

Each ring needs three input voltages, two for the cathodes and the field shaping strips and one for the guard (potential) wire. The voltage for each field shaping strip is provided through the built-in resistor voltage-divider network, whose ends are connected to the cathode and the central strip respectively. These points are supplied by the corresponding potentials  $V_{cat}$  and  $V_{centstrip}$  with the two lines mentioned above. Twenty-nine different voltages in  $k_{HV} \times 100$  V steps between  $-k_{HV} \times 4233$  V and  $-k_{HV} \times 1333$  V are applied to the field forming strips. The guard wires are all at the same potential of  $-k_{HV} \times 2000$  V, and the sense wires are grounded. The value for  $-k_{HV}$  under operating conditions is 1...1,2 depending on the used gas mixture. The three potentials necessary are delivered

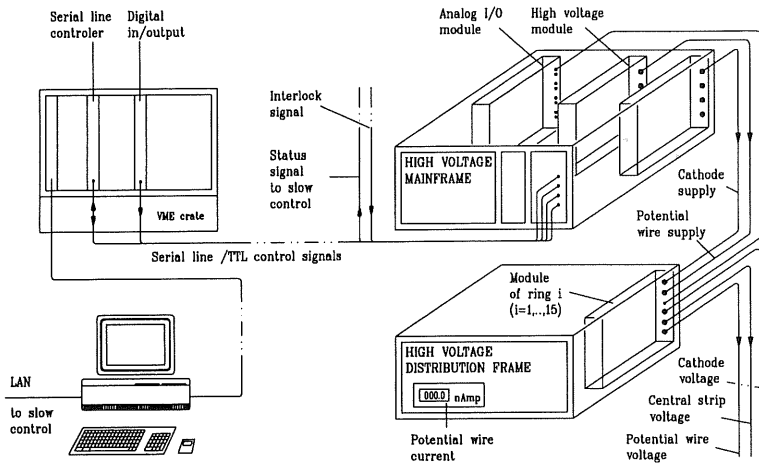


Figure 6.1: Layout of the high voltage system.

by a high voltage distribution resistor network which is for each ring supplied with two voltages  $V_{cat\_sup}$  and  $V_{pot\_sup}$  from a commercial mainframe [54]. The general setup is indicated in Figure 6.1. The two circuits are coupled together as shown in Figure 6.2. This provides stable operation voltages for the central strip and the potential wires and guarantees on the other hand high voltage protection. A drop in one of the two supply voltages will lead to higher currents in the other circuit. These overcurrents can then be used to switch the corresponding channel off. The potentiometers allow an adjustment of

High voltage potentials in the CIZ cell	
Cathodes and strips	$HV_{cath}$ = $-k_{HV} \times 4233$ V
	$HV_{centstrip}$ = $-k_{HV} \times 1333$ V
	Delta $HV_{strip}$ = $-k_{HV} \times 100$ V
	$HV_{strip}$ = $-k_{HV} \times (1333 + i \times 100)$ V for $i=1, \dots, 29$
Potential wires	$HV_{pot}$ = $-k_{HV} \times 2000$ V
Sense wires	$HV_{sense}$ = 0 V (grounded)

Table 6.1: Potentials in the CIZ cell.

each circuit for the corresponding ring. To correct tolerances in the built-in resistor chains different voltages are applied to different rings to achieve a constant electric field. With

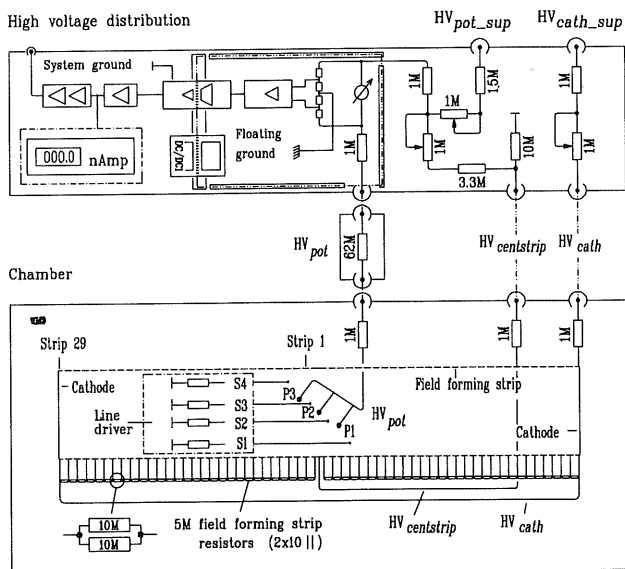


Figure 6.2: Schematic of the high voltage circuit.

the three potentiometers each part can individually be adjusted for this purpose. This allows a simpler operation of the detector, because the same supply voltage then generates

the same electrostatics in every part. In addition the resistors in the potential wire circuit are selected such, that  $V_{cat\_sup}/V_{pot\_sup} = 0.5$  provides the right potential distribution [see Chapter 4]. Since the CIZ is the drift chamber closest to the interaction point, a dedicated current monitoring system was designed and included into each potential wire supply line [55]. It allows to precisely measure the currents in the nA range, which is not provided

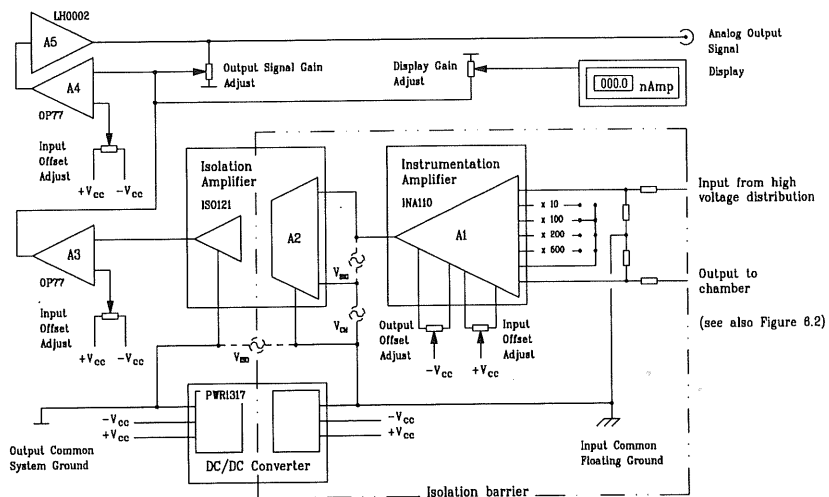


Figure 6.3: Schematic of the current meter.

by the mainframe. The measured currents, converted into an analog voltage signal in the range 0 to 10 V, can be fed into the main system using a special input / output module [54]. Therefore also these values can be recorded by using the standard readout chain which is illustrated in Figure 6.1. The potential wires control the gas amplification, and the activity introduced by interaction products or stray beam can therefore be monitored quite sensitively. Furthermore the high voltage inputs in the chamber are protected by a 1 MΩ series resistor. In the case of sparks or a dark current in the chamber they prevent a fast discharge of the capacitance of the high voltage supply system. The cables installed have a length of 35 m and a total capacitance of 4 μF. The resulting currents could therefore destroy unprotected detectors. During the initial phase at HERA a 64 MΩ series resistor was introduced in addition into the potential wire HV lines. High activity in the detector will cause the currents to rise and hence decrease the potential on the wire. The gas amplification will therefore automatically be reduced. The relation between the different potentials and the resulting values in the drift cells are shown in Figure 6.4.

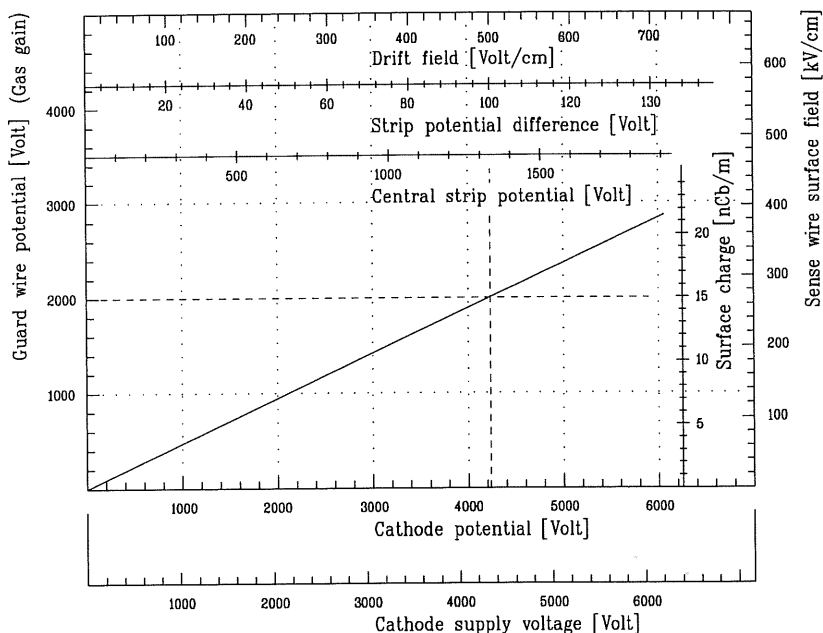


Figure 6.4: Relation of the supply voltages.

## 6.2 The analog signal electronics

The signal wires are read out on both sides to determine also the  $\phi$  coordinate along the wire by charge division. To improve this measurement (see Chapter 3) we selected an alloy [Elgiloy] with a resistance per unit length of about  $3 \text{ k}\Omega/\text{m}$ . For an average length of 120 cm the wire resistance is then of about  $3.6 \text{ k}\Omega$ . The total capacitance was measured for each wire individually to about 20 pF. This is the sum over all capacitances in the sixteen cells of a ring. At the cable channel the signal wires are directly connected to line drivers which allow a proper matching of the impedances to the  $50 \text{ }\Omega$  coaxial cables, which transport the signals to the backward chamber end plate. There the lines are terminated and fed into the standard H1 drift chamber electronics (see Figure 6.6). One of the main DC-requirements which defined the design of the line driver was low power dissipation because the elements are located within the gas volume of the detector. To save space and material we realized a circuit without extra power lines, with the consequence, that the signal and the supply voltage are distributed on the same cable. We wanted to use

Size(4 channels)	45x17 mm <sup>2</sup>
Rise time	<10 ns
Gain	0.4mV/ $\mu$ A ( $I_{out}/I_{in} = 10.9$ )
Input impedance	430 $\Omega$
Output Impedance	50 $\Omega$
Linearity	0.1 %
Power/channel	8 mW
Power	+5 V (from H1 drift chamber amplifier)
Average thickness	0.01 X <sub>0</sub>

Table 6.2: Properties of the CIZ line drivers.

only a minimum number of components with the best possible radiation hardness. The AC requirements were low noise and crosstalk characteristics as well as a safe protection against discharges in the drift chamber. The rise time should be better than 10 ns,

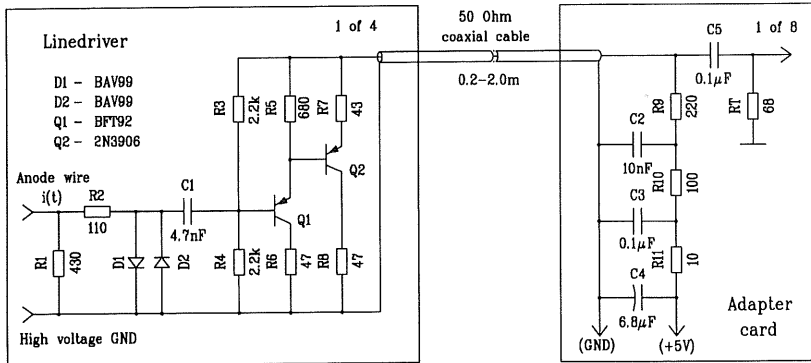


Figure 6.5: Schematic of the linedriver.

the input impedance  $\geq 200 \Omega$  and the output impedance  $50 \Omega$  to match the coaxial cable. The disadvantage of the AC-couplings needed at the input and the output of the device are outweighed by the advantages. The chamber is better decoupled from the electronics, which also allows to minimize reflexions and the noise. The circuit of the line driver is shown in Figure 6.5. It matches the chamber as well as possible to the standard electronics for all drift chambers in the experiment. The power of +5 V is taken from the H1 preamplifier and filtered on the adapter card to guarantee the necessary stability. The input impedance is  $430 \Omega$  and the rise time is better than 10 ns. To save space in the already quite narrow cable channel the coaxial cable serves at the same time as signal and power supply line for the elements installed in the chamber. The decoupling is done on

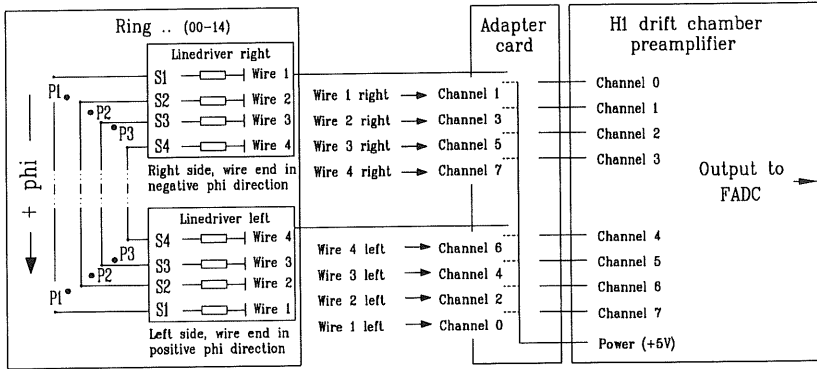


Figure 6.6: Overview of the signal electronics.

the adapter board (Figure 6.5) of the chamber flange. Each line driver has four channels in a volume of  $45 \times 17 \times 5 \text{ mm}^3$  using surface mounted technology (SMD). To further save space a left and right side type line driver were built. Connecting the signal wires directly to an active element provides a better signal shape, while coupling to a coaxial cable or strip line will deteriorate the signal shape, as apparent from Figure 6.7, where the two cases are compared. The rise time is about 40% shorter and the signal amplitudes appropriately higher. The resolution of the detector is mainly determined by the rise of

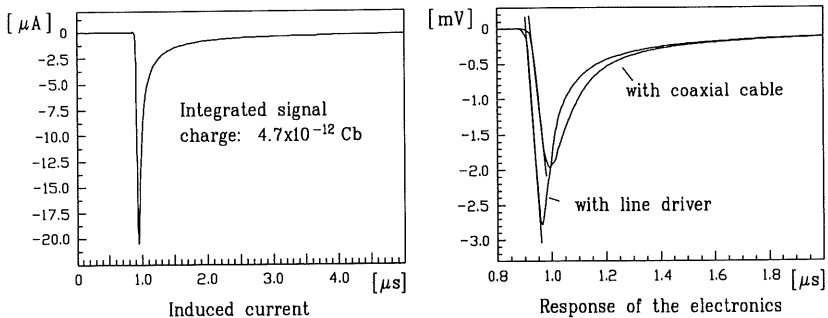


Figure 6.7: Influence of the linedriver on the signal rise time.

the leading edge of the signal (see Figure 8.1) and therefore it is obvious that the active element will result in a better performance. The standard H1 drift chamber amplifier has eight channels in a  $7.2 \times 60 \times 2 \text{ mm}^3$  volume and also uses SMD components on both

Properties of the H1 drift chamber amplifier	
Size(8 channels)	70x70 mm <sup>2</sup>
Rise/fall time	10 ns
Gain	100 mV/ $\mu$ A
Input impedance	200 $\Omega$
Output load	2x50 $\Omega$
Output amplitude	$\pm$ 2.5 V bipolar
Cross talk	< 0.5 %
Linearity	0.1 %
Noise (output)	5 mV
Power/channel	170 mW
Average thickness	0.02 X <sub>0</sub>

Table 6.3: Properties of the H1 drift chamber amplifier.

sides of the printed circuit board. This part fits directly to the CIZ adapter cards. It has an input impedance of 200  $\Omega$  and a differential output of  $2 \times 50 \Omega$ . The output from the preamplifier goes into a shielded twisted pair cable which connects to the 8-bit nonlinear flash analog to digital converter (FADC) with a 100 MHz clock.

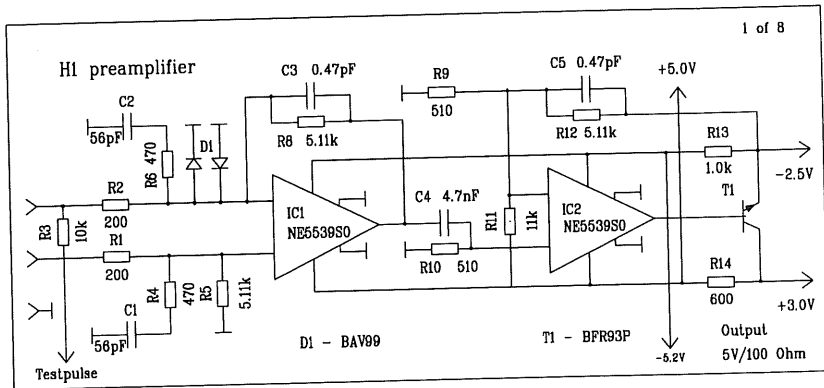


Figure 6.8: Circuit of the H1 drift chamber amplifier.



## 7 The readout and trigger system

### 7.1 The central part of the H1 data acquisition system

For a triggered event a total of over a quarter of a million analog channels are read out and digitised, resulting in some 3 Mbytes of raw information. As the time between successive electron-proton bunch crossings is just 96 ns, various levels of hardware triggering, software filtering and digital compression are employed before reducing final data sizes to acceptable storage media recording rates. The information is processed in parallel from the various subdetector partitions before being finally merged. Four main levels of triggering (filtering) can be enabled on all or part of the detector subsystems. The 3 Mbytes of raw data is reduced to event sizes of between 50 Kbytes and 100 Kbytes so that the final recording rates are restricted. For the data acquisition several hundred processing elements are embedded largely within the IEEE VMEbus standard, a detailed description is given in [56, 57, 58]. The data acquisition system collects the data from the subdetectors or “branches” over an optical fibre link. Then the data is merged and the full-event is distributed to subsystems which monitor and record the data onto permanent storage media. The readout system of each branch is autonomous up to and including a central subdetector VMEbus crate. It contains a dedicated supervisory readout controller, a multi-event buffer (MEB), a VMEtaxi and any input drivers necessary to access the data as seen in Figure 7.1. This architecture allows a particular subsystem to be decoupled from the rest of the detector. During acquisition the data is placed into the multi-event buffer by the subsystem. The Event Coordinator management task running on the master VMEtaxi of the ring searches for the next events in the subdetector multi-event buffers and when all branches are ready with the same event number, the separate banks are transferred via the optical ring into a full-event buffer (FEB). As the Event Coordinator VMEtaxi builds full-event records it simultaneously broadcasts them along its VMEbus to dual-ported memories associated with parallel sets of “full-event units”. Since the memory has read and write access from both the event task processors and the Event Coordinator, data can also be fed back into the system, for example, from the parallel filter farm. The final event records are sent to the central IBM facility at rates up to 7 Mbytes / s.

### 7.2 The trigger system

Because of the small cross section for  $ep$  physics large beam currents are required which result in a bad background environment. At HERA 210 proton and electron bunches circulate in the two rings with the design currents of  $I_p = 160$  mA and  $I_e = 60$  mA. The trigger system has to select interesting  $ep$  candidates from the background which consists basically of synchrotron radiation from the electron beam, proton gas interactions in the beampipe vacuum of about  $10^{-9}$  mbar and stray protons, which produce particle showers

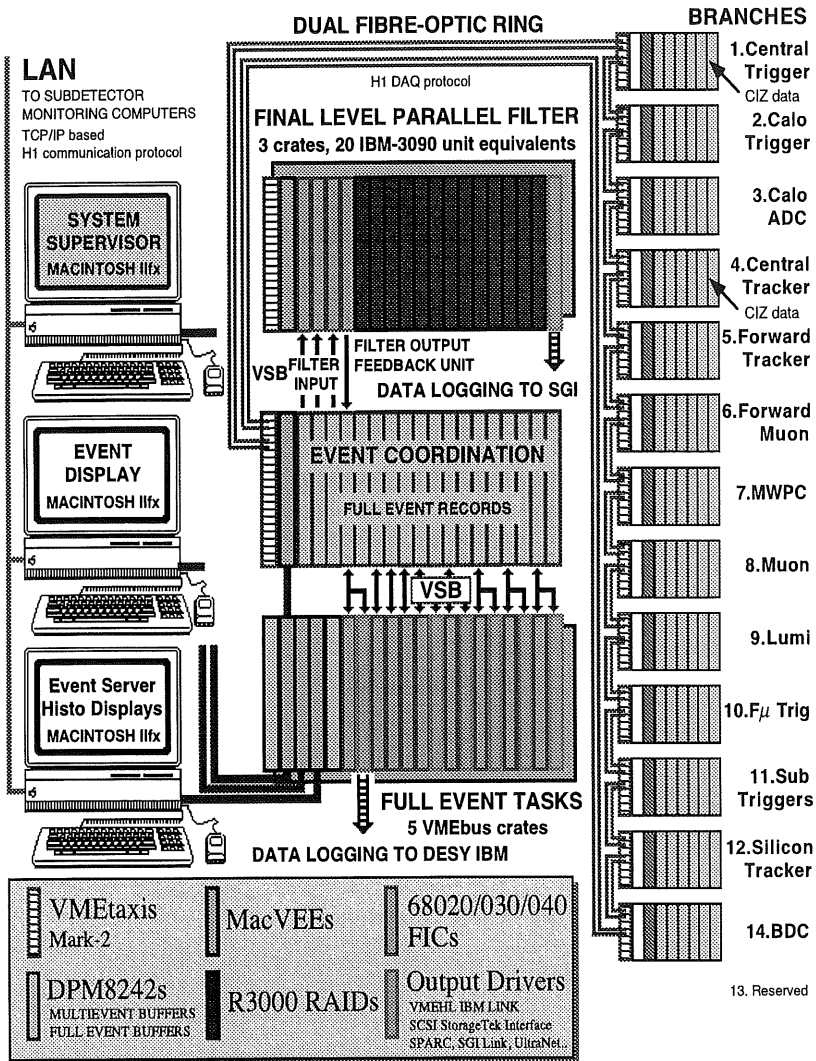


Figure 7.1: Physical layout of the H1 data acquisition. The CIZ data is read out in the central tracker branch, the slow control information (HV, temperature, ..) via the slow control system in the central trigger branch [59].

hitting the accelerator walls. Every 96 ns an electron bunch crosses a proton bunch at the interaction zone of the experiment. The probability for an interaction per bunch crossing (BC) is of the order  $10^{-3}$  which allows long response times as given by the drift chambers (11 BC) and the calorimeter (13 BC). Principally the information from all the detectors can be used to calculate a trigger decision provided that the information is still available after the decision took place. This can be realized in storing the individual data in pipelines with the necessary length. At H1 a four level trigger concept is realized [60,

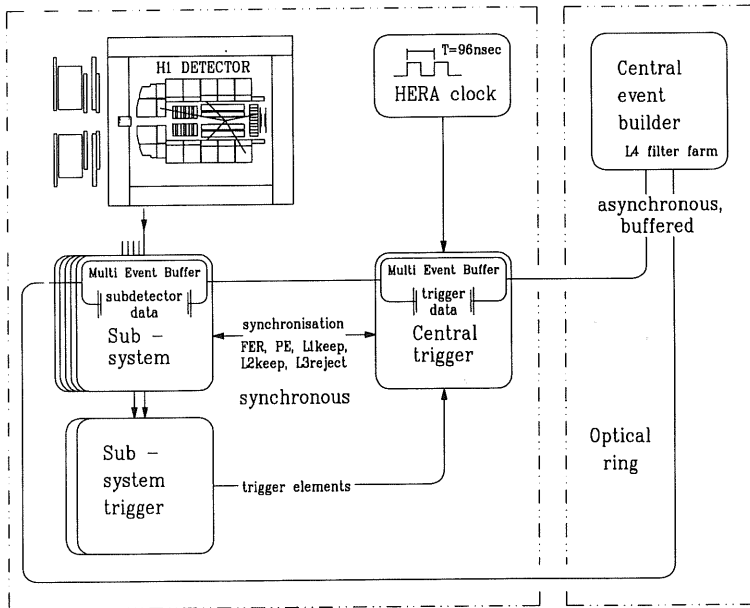


Figure 7.2: Overview over the trigger system.

34, 61]. Here the hardwired first level trigger is pipelined and completely deadtime free. A final first level trigger decision (called  $L1$  keep signal) is available centrally 24 BC ( $\sim 2 \mu s$ ) after the corresponding collision time, which also determines the minimal length of the pipelines. In the case of a  $L1$  keep signal the front end pipelines are held. Deadtime starts now and the level 2 trigger system evaluates more complex decisions based on combined information. After  $20 \mu s$  a  $L2$  keep signal will invoke further readout operations like data transfer and zero-suppression of the driftchamber signals etc. A negative decision on the other hand will result in a fast reject, which immediately starts all pipelines. The third level decision is available after a few hundred  $\mu s$  ( $< 800 \mu s$ ), in case of a reject the readout operations are aborted and the experiment is alive after a few  $\mu s$ . A parallel array of RISC

processors provides the fourth level of software coded filtering. It is integrated into the central data acquisition system and has the raw data of the full event available as a basis for its decisions.

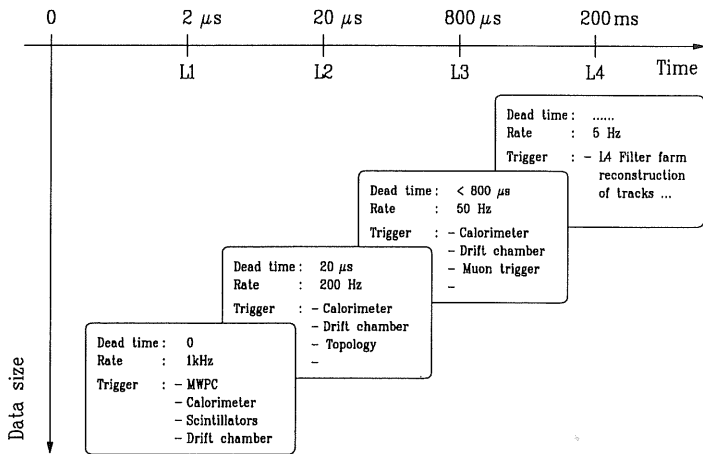


Figure 7.3: H1 trigger levels.

## 7.3 The drift chamber readout system

### 7.3.1 Overview

The readout of the drift chamber described here is implemented in the subsystem or branch which processes the signals from all central drift chambers, i.e. the central jet chambers (CJC1 and CJC2) and both  $z$ -chambers (COZ and CIZ) (see Figure 7.4). The analog signals from the preamplifiers are fed into FADC cards where the pulses are digitised and stored. In the case of a positive trigger (L1keep / L2keep / L3) decision the data is read out and processed by the scanner and later transferred to the multievent buffer (MEB). Each subsystem has a dedicated connection to the central trigger providing the necessary control signals to steer the subsystem, and to the central event builder for the data transfer. The standard H1 subsystem trigger controller crate (STC crate) contains the Subsystem Trigger Controller card which communicates with the central trigger system. The logic card is the hardwired sequence controller of the drift chamber readout system. Combining the responses from the scanner the front end ready (FER) signal is generated and sent to the central trigger system. This signal is required by the central trigger system

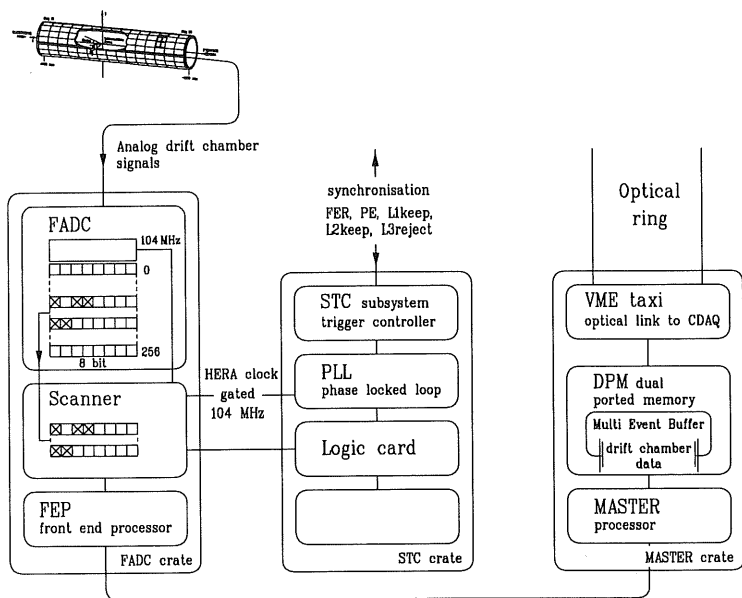


Figure 7.4: The drift chamber readout system.

from all the subsystems before it signals the pipeline enable (PE) signal, which then starts the pipelines for the next event. The introduction of the logic card in the path allows better performance by overlapping some stages of processing therefore the drift chamber readout system runs at almost full throughput with little or no actual dead time. The additional logic provides special functions required in the drift chamber readout. The processor (FIC Fast Intelligent Controller) can broadcast 12 bytes of data to the scanner via a serial link during the scanning. This allows a dynamical processing of the data on the basis of additional information. The 104 MHz phase locked loop (PLL) card generates the sample frequency required by the FADC cards with an accuracy of about 1 ns. The master crate contains the interfaces to the central data acquisition (CDAQ-VME taxi link) and to the front end crates (FADC crates) in the branch. In each of these crates a processor card (FIC), a scanner card and the FADC cards required by the corresponding detector part are installed (up to 16). During data processing the master processor operates asynchronously, waiting for an event to be signalled by the trigger processor and then polling the FEPs until the complete event is transferred to the MEB, ready to be built by the CDAC event builder.

### 7.3.2 FADC card

The analog signals from the drift chamber are digitised in Flash-Analog-to-Digital-Converters. They sample at ten times the HERA bunch frequency and operate in the common stop mode. This means that the analog signals are continuously digitised and stored in the memory until the process is stopped by a level 1 trigger signal. Then the last 254 sampling time slices are recorded in the circular buffer, which corresponds to the past of about 2 *mus*. Sixteen analog inputs can be fed into one FADC card. The standard H1

Ring	Left side sense wire	Right side sense wire	Amplifier channel	FADC i channel	Byte <sup>[*]</sup>			
					bit 31..24	bit 23..16	bit 15..8	bit 7..0
i	1	1	0	X0				3
			1	Y0			2	
			2	X1	1			
			3	Y1	0			
	3	3	4	X2				3
			5	Y0			2	
			6	X3	1			
			7	Y3	0			
i+1	1	1	0	X4				3
			1	Y4			2	
			2	X5	1			
			3	Y5	0			
	3	3	4	X6				3
			5	Y6			2	
			6	X7	1			
			7	Y7	0			

Table 7.1: Correlation between drift chamber wire and the byte, which contains the corresponding data.

[\*] Byte numbering taken from [62].

preamplifier has 8 inputs which is exactly the number of signal lines coming from one drift chamber ring with four signal wires which are read out on both ends. Therefore two rings, i.e. two preamplifier are connected to one FADC card. The differential output signals of a preamplifier are transmitted over a single shielded coaxial cable of about 30 m length which also provides the power and test pulse lines. The bipolar signals are combined and fed to the ADC chip through a transformer eliminating direct current (DC) offsets. The resolution of the used FADC chip is 8 bit. Coupling the input signal to the reference voltage via a resistor network provides a nonlinear response function. Keeping in mind that the signal distribution of such detectors contains many signals of small charge but also a few with large charge, one realizes the advantage of the good 8 bit resolution for small signals and the enlarged dynamical range to 10 bit. The response function is shown

Properties of the F1001 FADC units	
Size(16 channels)	triple euro card, 460 mm deep
Input (bipolar)	4 V matching to FADC with transformer; variable offset ( $\approx 8$ counts)
FADC	8 bit nonlinear = 10 bit linear
Sensitivity	4 mV/bin
Sampling rate	104 MHz
Record length	256 words
Output	analog signals at the front panel; digital information over VME - D16 or D32 block transfer
Maximum readout speed	64 MByte/s (16 MHz/32 bit)

Table 7.2: Properties of the FADC units.

in Figure 7.5 and the linearization is done by the following relation

$$A_{lin} = \left( \frac{A_{notlin} \times 700 \times 1024}{256 - 722 \times A_{notlin}} \right) \frac{1}{2519} .$$

The FADC card is connected over the VME backplane to the scanner. This allows a fast 32 bit wide readout of the FADC memories. The risetime of the signals, which is deliberately degraded by the electronics and the cables, is larger than 20 ns at the ADC input. Therefore the sampling frequency of 104 MHz guarantees a good time measurement.

### 7.3.3 Scanner card

The scanner card in the front end crate is the sample controller for the FADC cards. It drives the FADC cards with the 104 MHz clock. The controlling of the sampling period with respect to the event trigger ( $L1$  keep) can either be done by the scanner or more centrally by the phase lock loop card in the STC crate. In the first mentioned scheme the  $L1$  keep signal has to be distributed to the front end crates where the pipelines will be individually disabled, which can cause timing problems, whereas in the latter case it is only done once for the whole system. In the case of a positive second level trigger signal ( $L2$  keep) the scanner copies the data from the FADC memories into a second level buffer. During this copy operation it performs zero suppression by constructing a table of pointers to the significant data above a programmable threshold. When the scanner has finished it asserts lock, which means that there is valid data in the scanner buffer that the front end processor has not finished dealing with. Only at a positive third level trigger signal the scanner will interrupt the front end processor and initiate the event building

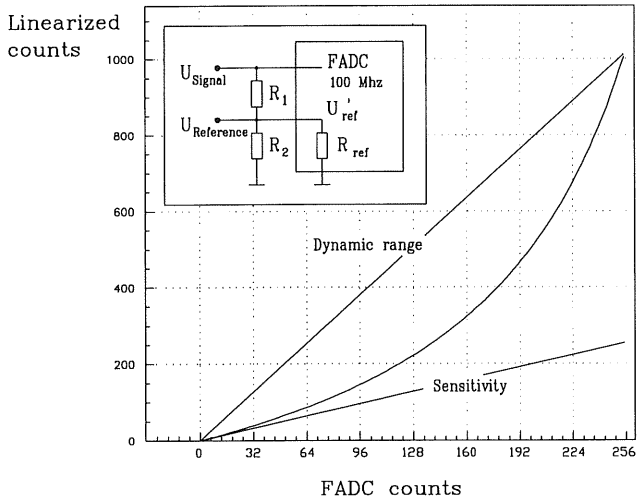


Figure 7.5: FADC response function.

into the multi event buffer. The hit detector of the scanner compares the data to a preset threshold as it is being copied into the scanner memory. Hit flags are produced for each of the 16 channels independently of each other. If two consecutive time slices are above threshold, a start of a hit is recorded, if no previous hit is active. The end of a hit is assumed, if two consecutive time slices are below threshold. An additional feature allows to require pulses with a minimum length. If the active hit ends before a preset number of time slices — counted from the start time — the hit flag will be cleared. When the hits are read out from the processor the program adds time slices to the front (presamples) and the back (pastsamples) of the pulse. The presamples are used in the pulse shape analysis to evaluate the pedestals. The threshold and the number of pre- and post samples can be selected in the drift chamber readout program. The actual settings for every run are stored in the run start record.

## 7.4 The slow control system

Slowly varying detector parameters like temperature, gas mixture, high voltage, etc. are monitored and steered by the slow control subsystem computers. These computers are connected to the Central Slow control over the Local Area Network (LAN) where the so called Slow Events (SE) are collected. The CSC computer then provides the data for the online display of the detector status. If the central data acquisition is running the



information is also injected into the main data stream through the central trigger system, as shown in Figure 7.6 otherwise it is sent directly to the IBM mainframe. Hardware alarms as for example a gas system alarm are maintained by the second part of the slow control system. Only hardwired combinatorial logic is involved to handle critical situations and does therefore not depend on computers. All hardware alarm signals are connected to a central routing device. Here any logical combination of the input signals can be generated and again distributed as for example the high voltage interlock signal.

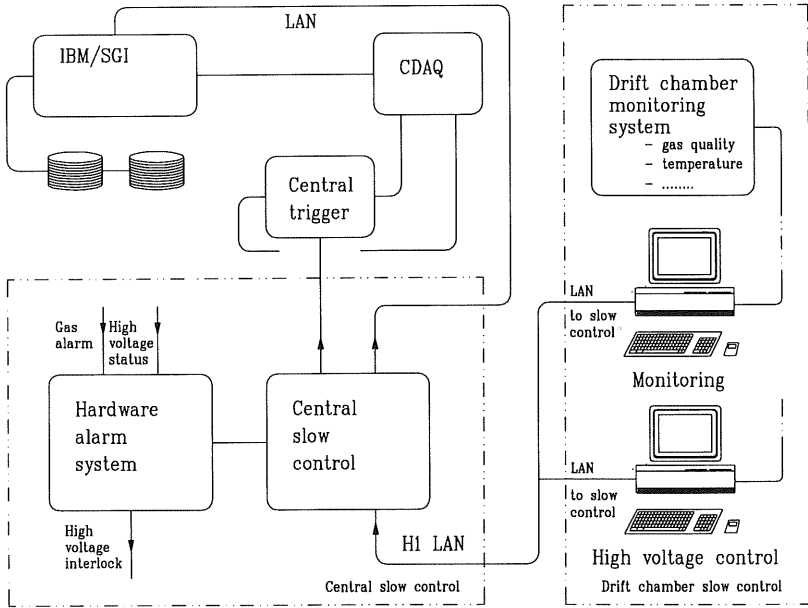


Figure 7.6: Slow control system.

## 8 Pulse shape analysis and space point reconstruction

### 8.1 Introduction

The use of FADC's (flash analog to digital converters) in the readout to record the time development of the drift chamber pulses ensures significantly improved resolution compared to more conventional simple threshold sensitive electronics. Accurate timing is facilitated and the pulse shape information permits the determination of the charge integral for each pulse. The latter is exploited in the charge division measurements, giving true space points along the wire. In other chambers of the detectors, it allows  $X$ -ray detection as well as energy loss ( $dE/dx$ ) measurements, whereas in the CIZ the information from normally three hits is not sufficient for this purpose. The benefits of recording the pulse shape outlined above outweigh the drawbacks of using FADC's, the most severe of which is the huge quantity of raw data generated. Sampling at 100 MHz one FADC would take only  $10\mu s$  to produce a kilobyte of raw data. It is therefore essential to perform some form of "zero suppression" as early as possible in the readout chain. This zero suppression will be effected by the scanner in each crate (see Chapter 7). It will rapidly transfer the entire content of the FADC memory into its own internal buffer and simultaneously produce a set of pointers to regions containing non zero data. The data in the scanner will then be read out by the front end processor (FEP). This information may be analysed in a dedicated program to give a drift time and pulse integral for each hit, which will then be passed on to the later stages of the data analysis. The charge time algorithm ( $Qt$  algorithm) reduces the amount of data again by a factor of about five. The program can process the data on the front end processor (FEP) and therefore reduce the size already at this stage. Using the measured drift time and the charge difference from both wire ends the track coordinate in  $rz$  and the azimuthal angle  $\phi$  will be reconstructed, respectively. This analysis can already be done online on the  $L4$  filter farm.

### 8.2 Determination of the charge and the time ( $Qt$ analysis)

The digitized raw pulses with suppressed base line, as provided by the scanner hit detector and zero suppression, must first be re-linearized before attempting any pulse analysis. The linearization function is given by the nonlinear characteristic of the FADC (see Chapter 6). After re-linearization the pulse finding function then steps through the linearized cluster and locates all the pulses. From the presamples the pedestals are first determined for each cluster individually. Two subsequent channels with increasing content define the start of a pulse. If the pulse was rising and we have found the maximum we fit the drift time and store the information on that pulse. Requiring a minimum separation from the previous pulse a possible second or further ones can be found. If the second pulse occurs on the tail of the first, both are tagged as overlapping. The end of the pulse is defined as two

adjacent channels on a falling edge below a threshold or by the start of a next one. After processing all the clusters the program loops over the pulses found and tries to combine the information from both wire ends. For those pulses belonging together the integration bands are defined and the drift time is computed weighting with the amplitude from both sides. The arrival times from the two sides may only differ within narrow limits. Finally the charge integration is performed.

### 8.2.1 Timing algorithms

A simple threshold cut on the raw FADC data would create a set of 'integer' drift times associated with the 9.6 ns binning resulting from the sampling frequency. For the gas mixture of  $Ar/CH_4$  (80/20) at the drift field of  $500 \text{ V cm}^{-1}$  the drift velocity is such that 9.6 ns corresponds to a drift distance of about  $500 \mu\text{m}$ . In order to achieve the desired accuracy of  $300 \mu\text{m}$  over the drift space, an improved drift time must be reconstructed on the basis of information from the adjacent FADC bins on the "leading edge" of the pulse. In the CIZ code two methods are implemented to obtain the drift time from a fit to the FADC signal. In the first electron method (FEL) a line is fitted to the rising edge of the pulse ignoring the first and the last point, where the maximum occurs. The intercept of this line with the pedestal is then defined as the FEL drift time. In the differential center of gravity method (DCOG), the differences between adjacent channels from the start of the pulse to the maximum are computed. The drift time is then defined as the center of gravity of these differences of samples. The drift times computed in these two methods are not the same as indicated in Figure 8.1. The FEL method is generally considered

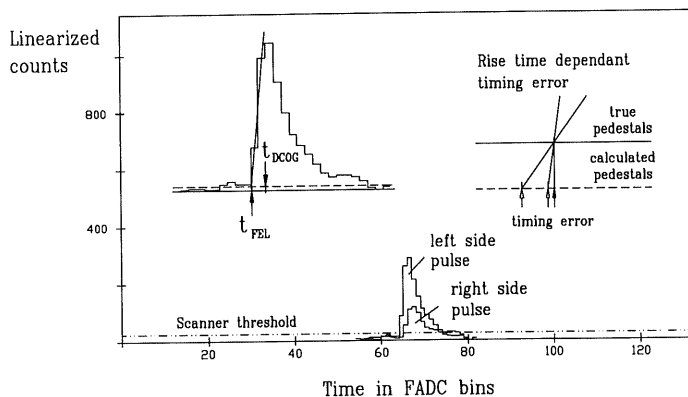


Figure 8.1: Typical pulses seen at the two ends of a wire in the CIZ.

better for high resolution chambers [63], here both methods are equally good for isolated

pulses. For closely spaced pulses of unknown shape, the DCOG method will give a better estimate of the true drift times. A comparison and overview of different time algorithms can be found in [64].

### 8.2.2 Characteristic drift time distributions

For uniformly illuminated drift cells the drift time distributions have a characteristic shape due to the cell structure. The maximum drift distance is shorter for the outer wires compared to the inner ones. The outer wires also collect charge from both sides, however only in the range of about 3 mm, for longer drift distances only electrons from one side produce a signal. The inner wires on the other hand collect charge from both sides in

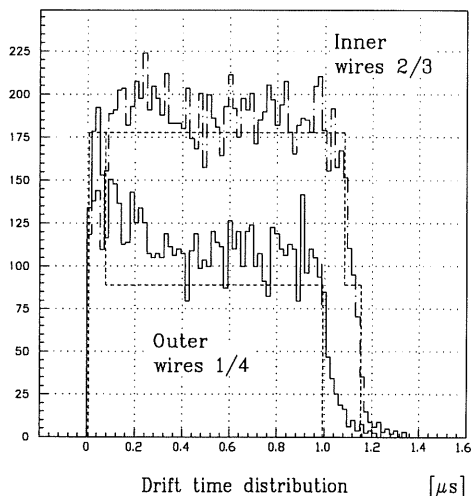


Figure 8.2: Characteristic drift time distribution, the dotted lines indicate the expected distribution for uniformly spread primary ionisation.

the drift cell over the full range. The maximum drift distance for the left and the right side respectively are different because the wires are not located in the cell center. The resulting drift time distribution is illustrated in Figure 8.2. Such a plot is often used to measure the drift velocity.

### 8.2.3 Charge integration and characteristic distribution

In addition to the coordinate along the drift direction the CIZ provides also the position along the wire. This is achieved by using a resistive anode wire and reconstructing the

coordinate in  $\phi$  by division of the charge collected at each end of the wire (see Chapter 3). For an accurate charge division measurement not only the FADC pulse integral must be well defined, but also the estimate of the underlying pedestal. The pedestal is estimated by taking the average of all bins proceeding the region of the first pulse on that wire. The pulse integral is simply taken by the summation of the bins in the specified region. As a consequence of the peculiar chamber construction the inner and outer wires do not collect the same amount of charge, as shown in Figure 8.3.

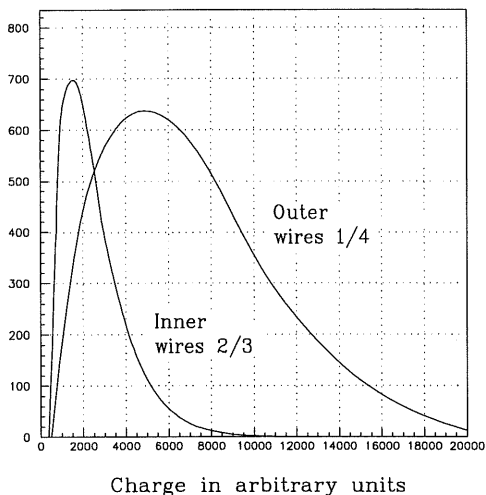


Figure 8.3: Characteristic charge distribution (both wire ends summed).

## 8.3 Space point reconstruction

### 8.3.1 General

After the drift times and the charges have been computed, the position  $(z, r)$  and the position in  $\phi$  have to be determined. From the charges at both wire ends  $\phi$  is given by (see Section 3) charge division

$$\phi_{Hit} = \phi_0 - \phi_{length} \times \frac{Q_{left} - g_{rel} \times Q_{right}}{Q_{left} + g_{rel} \times Q_{right}}$$

where  $\phi_0$ ,  $\phi_{length}$  and  $g_{rel}$  are calibration constants. Due to the large range of allowed crossing angles in the detector ( $16^\circ$  to  $169^\circ$ ) there is not a simple relationship between

drift time and the position in the chamber. The position  $(z, r)$  is a function of drift time ( $t_D$ ), wire number ( $n_w$ ) and crossing angle ( $\theta$ ), which is unknown initially. The procedure depends crucially on the knowledge of the isochrones in the chamber (see Chapter 4), which are parametrised as circular arcs in the form

$$(z - a(t_D))^2 + (x - b(t_D))^2 = \rho(t_D)^2$$

with  $r = r_0 + x$ . Here  $z$  and  $r$  are the coordinates in the chamber and  $a, b$  and  $\rho$  are functions of the drift time and wire number. Using the simulation program [31] lookup tables for  $a, b$  and  $\rho$  in time steps of 100 ns have been obtained. For a given drift time the isochrone parameters are then computed via interpolation in the table, where the values of  $z$  and  $r$  are constrained to be within ranges given by  $x_{max}(t), x_{min}(t), z_{max}(t)$ . Using the center of the isochrone section an initial guess for the position  $(z, r)$  is simply given by

$$z_{guess} = a(t) + \rho(t) \quad r_{guess} = r_0 + x_{guess} = r_0 + b(t) .$$

Two procedures are then applied to correlate hits with one another to reconstruct segments in a single drift cell or to link the hits to track segments from other detector parts.

### 8.3.2 Reconstruction of CIZ segments

Independent from other outside information single track segments in the CIZ cell can be reconstructed. These can then later be linked to segments from other detector parts [65], or independently be used for tests. To correlate hits in a drift cell a search is made starting with the earliest hit on each wire looking for hits which are close to each other in  $\phi$  and relatively close in time. If two hits on wires 2 and 3 can be matched, then wires 1 and 4 are examined for hits which are close in  $\theta$ , and which agree with the rough crossing angle obtained from wires 2 and 3. If these conditions are met, the hits are connected, and if either wire 1 or wire 4 showed a hit, the corresponding side of the wire plane is known. There is a small region around the sense plane where it is possible to have all four wires in a track, or only wires 2 and 3. These special cases are allowed, however there can be an ambiguity on which side of the wire plane the track crossed. To resolve it additional information from another CIZ cell (e.g. cosmics) or either from another detector part is required.

From the associated hits and their isochrone parameters the absolute position can be calculated. Using the initial guess for the  $(z, r)$  position, a line is fitted through the coordinates of the hits

$$z_i^0 = a(t) + \rho(t) \quad x_i^0 = b(t) \quad z = \alpha \cdot x + \beta .$$

For the next iteration the point on the isochrone which has the same slope  $\alpha$  as the above line, is taken as the next guess to the true points.

$$z_i^{k+1} = a_i + \rho_i / \sqrt{1 + \alpha_k^2}$$

$$x_i^{k+1} = b_i + \rho_i \cdot a_k \sqrt{1 + \alpha_k^2}.$$

If any of the  $x_i$  are larger than the corresponding  $x_{max}$ , or smaller than  $x_{min}$ , the point  $(z_{max}, x_{max})$  or  $(z_{min}, x_{min})$  is taken as the next value of  $(z, x)$ . Then the value

$$\chi_A^2 = \sum_{i=1}^n (\alpha_{cir} - \alpha_k)^2$$

is computed, where  $\alpha_{cir}$  is the tangent of the circle at the point, and  $\alpha_k$  is the slope of the new line. This procedure is repeated until  $\chi_A^2$  is smaller than a cut off value. If this occurs the  $\chi^2$  is calculated as following

$$\chi^2 = \sum_i^n \frac{(z_i - \alpha \cdot x_i - \beta_i)^2}{\sigma_z^2}.$$

The resulting values of  $(z, r)$  are then taken as the coordinates in the chamber, and the slope is the tangent of the crossing angle.

### 8.3.3 Linking CIZ hits to CJC segments

If a vertex has been found by the jet chamber reconstruction program, and if it is assumed that all tracks originate from this vertex the appropriate coordinates for hits in the CIZ can be calculated, and the corresponding hits found can be collected in a linking module. [65, 66].

Given the vertex coordinate  $(z_v, r_v = 0)$ , and the isochrone parameters for the hit  $(a_i, b_i, r_i, z_i^0, x_i^0)$ , the slope  $\alpha$  can be estimated as

$$\alpha = \frac{z_i^0 - z_v}{x_i^0 + r_0}$$

where  $r_0$  is the nominal chamber radius. Using  $\alpha$ , a better point can be obtained as

$$\begin{aligned} z_i^1 &= a_i + \rho_i / \sqrt{1 + \alpha^2} \\ r_i^1 &= b_i + \rho_i \cdot \alpha / \sqrt{1 + \alpha^2}. \end{aligned}$$

Both the left and the right solution for every valid hit in the CIZ are computed. The reconstruction program then uses the CJC track information to project into the CIZ and identify hits which could be associated with the track. If an association is made, with the track information from the CJC an improved  $z$  and  $r$  for the hits can be provided. The more precise  $\phi$  value from the CJC also allows to better determine radial coordinate, which varies because wires are strung along a polygon and not along a circle.

## 8.4 Calibration constants and their determination

The final determination of the space point in  $r, z$ , and  $\phi$  also depends on a number of calibration constants and parameters. These include geometrical constants like the accurate wire position. Electrostatic and gravitational forces will move the wires away from their original position. A mechanical deformation of the detector will change the wire position also. Secondly, there are parameters which depend on the running condition of the drift chamber, as the drift velocity which is a function of the applied electric field as well as the magnetic field. Finally the readout and signal electronics influence the measurement of the time and the charge. The measured time has therefore to be corrected

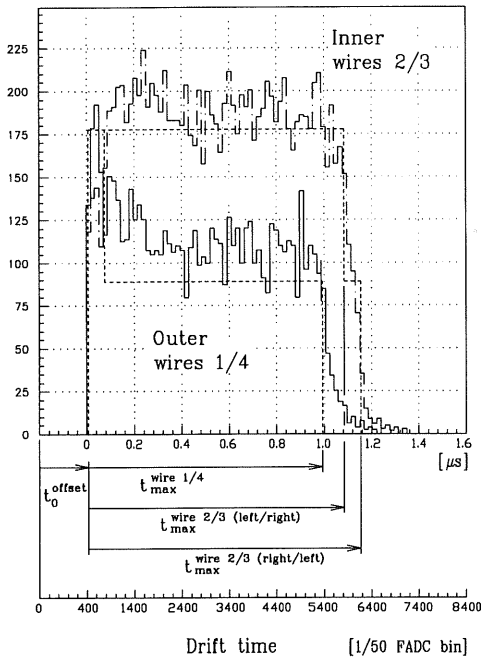


Figure 8.4: Calibration constants  $t_0^{offset}$  and  $v_D$ .

for all known offsets. The drift time to calculate the position is then given by

$$t_D = t_M - t_0^{offset} - t_0^w$$

where  $t_M$  is the measured time as provided by the  $Qt$  routine,  $t_0^w$  is the wire by wire offset introduced by differences in cable length and propagation times and  $t_0^{offset}$  is the global



time offset determined by the global cable length and delays in the readout system. The drift velocity is contained in the isochrone map, nevertheless a linear correction factor  $c_{scale}$  is used for a precise adjustment. The isochrone map is scaled linearly to correspond to the actual drift velocity. Similarly for the determination of the  $\phi$  coordinate, which can be calculated from

$$\phi_{Hit} = \phi_0^w - \phi_{length}^w \times \frac{Q_{left} - g_{rel}^w \times Q_{right}}{Q_{left} + g_{rel}^w \times Q_{right}}$$

the necessary calibration constants have to be known. This are the center of the wire  $\phi_0^w$ , the effective wire length  $\phi_{length}^w$ , determined by the ratio of the amplifier input resistance to the resistance of the anode wire, and the relative gain factor  $g_{rel}^w = g_-^w / g_+^w$ , which corrects for differences in the amplifier gain. The parameters, depending on the geometry, like the wire positions and the wire centers  $\phi_0^w$  are given by the precision of the chamber alignment. The most crucial parameters are the global time offset  $t_0^{offset}$ , the drift velocity

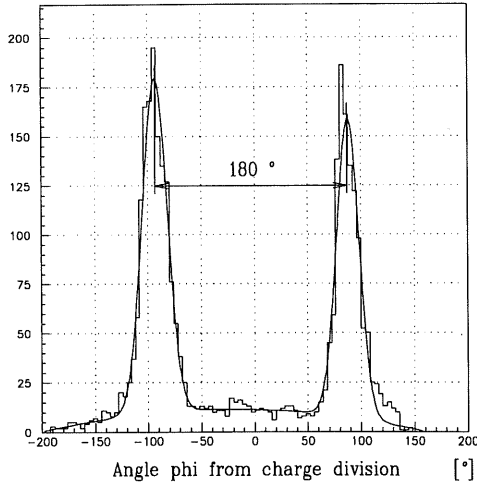


Figure 8.5: Charge division from cosmic tracks.

$v_D$  (respectively  $c_{scale}$ ) and the effective wire length  $\phi_{length}^w$ , they have to be determined immediately. In a later step the wire by wire corrections as  $t_0^w$  and  $g_{rel}^w$  can be evaluated and applied. In principle all these constants may be determined internally without reference to other devices. The time offset and the drift velocity can be evaluated simply from the drift time spectrum. As indicated in Figure 8.4 the rising edge of the distribution gives the time  $t_0^{offset}$  and the falling edge the maximum drift time, which corresponds to the maximum drift length. The drift velocity is then calculated by  $v_D = \ell_{Dmax} / t_{Dmax}$ . In

matching the track segments, which cross the wire plane we have another possibility to determine  $t_0^{offset}$ . The drift velocity can be determined too, matching the segments from tracks which cross the cathode cell boundaries. However, for the CIZ the precision of these methods is limited by geometry and the small number of wires. Using cosmic tracks also the effective wire length can be determined internally by looking at the measured  $\phi$  distributions. The difference between the two peaks visible in Figure 8.5 should be  $180^\circ$  for vertical tracks. A more precise and accurate determination of the calibration constants can be done with respect to an external detector. With the accurate  $\phi$  information from the CJC the constants  $\phi_0^w$ ,  $\phi_{length}^w$  and  $g_{rel}^w$  can be determined for the CIZ. On the other side the CJC uses the accurate  $z$  information from the  $z$ -chambers to tune their  $z$  resolution. For the  $t_0^{offset}$  and  $v_D$  calibration of the CIZ the  $z$  information from the COZ can be used. A calibration method, using the whole set of the central detectors, will be described in the next chapter.

## 9 Chamber performance — cosmic and test beam data

### 9.1 Intrinsic resolution

Using cosmic rays the intrinsic resolution was measured during a cosmic ray test. Two scintillation counters were arranged, one on top of a drift chamber ring and a second one on the bottom of the neighbouring ring. As a consequence the cosmic ray tracks triggered by the scintillators crossed the top cell of one ring and the bottom cell of the other. Requiring two reconstructed segments, one above and one below, a common line fit was then made to both, i.e. to six points. In Figure 9.1 the distance between the

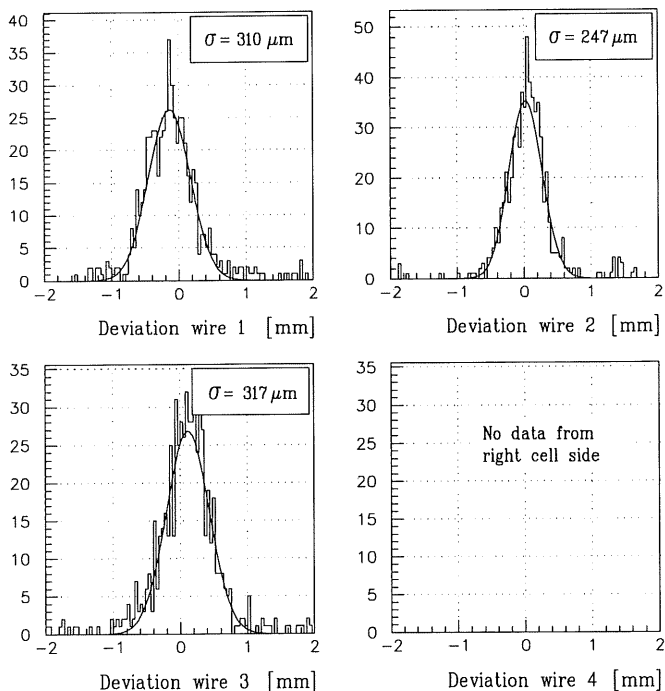


Figure 9.1: Deviation of the single wires for tracks, which pass the right cell side (no signal on wire 4).

measured points and the fitted line are plotted for each wire. This data shows the true

performance of the chamber. From the width of these distributions we deduce a resolution of  $\sigma = 310 \mu\text{m}$ ,  $247 \mu\text{m}$ , and  $317 \mu\text{m}$ , respectively. These results are compatible with the measurements done with a prototype [67]. In Figure 9.2 we show the latter results for the resolution in function of the drift distance for the  $ArCH_4$  gas mixture. It is decomposed into the typical contributions and can be written as

$$\sigma^2 = \sigma_S^2 + \sigma_{Diff}^2 + \sigma_c^2$$

where  $\sigma_S$  is the contribution of the primary electron statistics, it falls off as the inverse of the distance from the wire. The second term is due to the electron diffusion, it is a function of square root of the drift distance  $\sigma_{Diff} = \sigma_{0Diff}\sqrt{\ell}$  and  $\sigma_c$ , a constant background contribution, which is due to the timing resolution of the electronics and timing algorithms. Tracks cross the chamber between  $\theta = 20^\circ$  and  $\theta = 170^\circ$ . The results shown in Figure 9.2 indicate that the resolution is independent of the crossing angle, and hence one of the primary design criteria for CIZ has indeed been met.

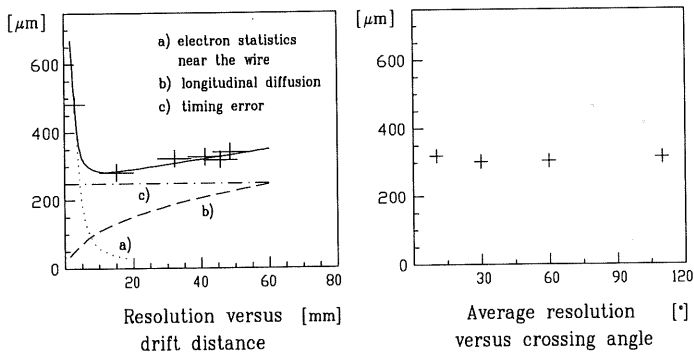


Figure 9.2: Resolution as a function of drift distance and crossing angles (test beam results [67]).

## 9.2 Combined resolution

The H1 tracking detectors have been designed to provide a good momentum resolution in combining the information from the different subdetectors. A clean cosmic event, which penetrates the central tracker from above and passes near the beam axis, produces signals in the CJC, COZ and the CIZ. The reconstruction in the jet chamber recognizes it as two tracks coming from the vertex. The linking procedure picks up the hits in the  $z$ -chambers and fits the tracks with using the more accurate  $z$  information. For cosmic

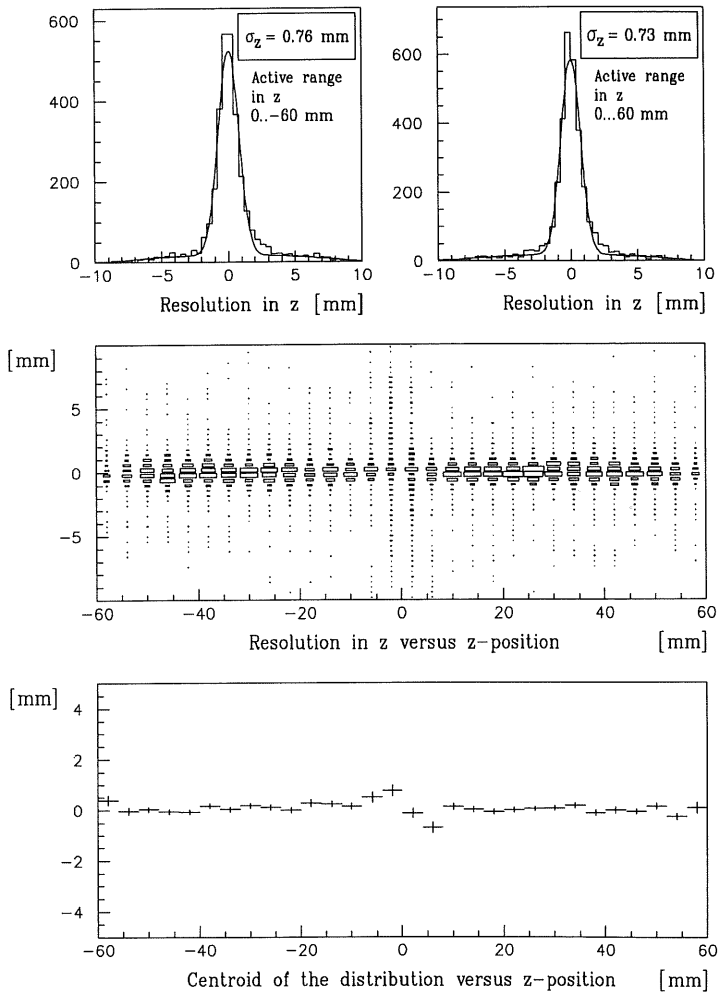


Figure 9.3: Combined resolution in z, it is determined with cosmic tracks.

rays tracks above and below the beam line can be fitted to one straight line in the  $z, s$  plane, where  $z$  is the coordinate along the beam axis and  $s$  the arclength. This procedure allows to intercalibrate the chambers using information from other detectors and to control their resolution. In the magnetic field the particles travel along a helix in space, with a symmetry axis parallel to the field direction. In the  $x - y$  projection, the track appears

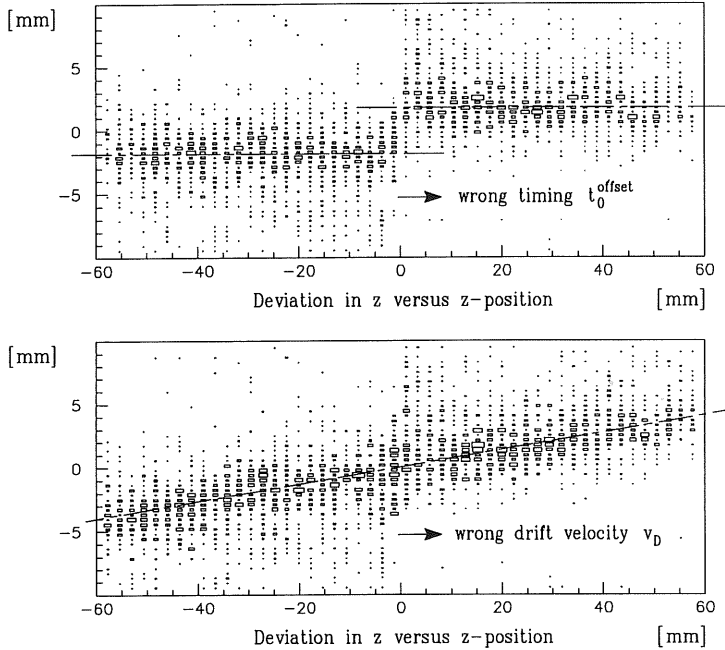


Figure 9.4: The systematic shifts are due to wrong calibration constants  $t_0^{offset}$  and  $v_D$ .

as a circle of radius  $\rho = \frac{1}{\kappa}$ , while in the  $z - s$  projection, it appears as a straight line. The arclength at a point  $(x_i, y_i)$  can be calculated as follows. If  $r_i = \sqrt{x_i^2 + y_i^2}$

$$s = \rho \cdot \arccos \frac{\rho^2 + d^2 - r^2}{2\rho \cdot d}$$

where  $d = \rho - r_0 \text{sign}(\kappa)$  and  $r_0$  is the distance of closest approach to the  $z$  axis. The arclength  $s$  is zero for  $r = r_0$ . Using the  $(z_i, r_i)$  pairs for the correlated  $z$ -chamber hits, we use the CJC information to convert them to  $(z_i, s_i)$  pairs in the  $z - s$  plane. The parameters  $\kappa$  and  $r_0$  are taken from the CJC tracks. The points should then fall on a line

$$z = \alpha \cdot \rho + \beta .$$

Reverting the sign of  $s_i$  on one of the tracks all the points from both track segments satisfy the same linear equation. Fitting a straight line with  $n$  points, each of which is measured with an error  $\sigma_i = \delta z_i$ , we can solve for  $\alpha$  and  $\beta$ . We can carry out different fits, which are useful for the calibration and to determine finally the achieved resolution. Using the COZ we can calibrate the CIZ. Fitting the data from the COZ and looking at the deviations

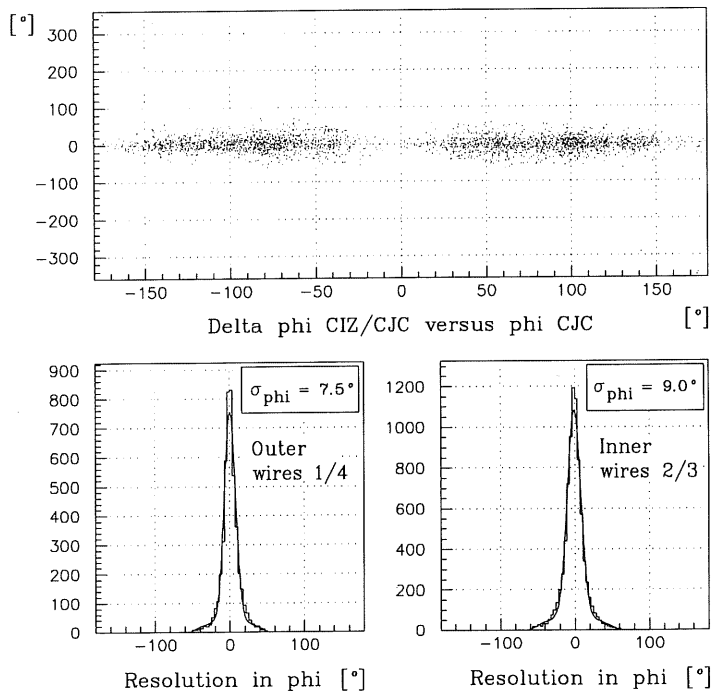


Figure 9.5: Resolution in  $\phi$ , this coordinate is determined by charge division.

of the CIZ hits from the track fit as a function of the drift distance, we will immediately see systematic shifts, caused by wrong time zero offsets or drift velocity as illustrated in Figure 9.4. Finally we can compute the resolution by making the line fit excluding the corresponding hit, and then computing the distance from this hit from the line. Repeating the same procedure with the COZ, we arrive at its calibration too, with the resolutions given in Figure 9.3. This calibration can still be improved, if a sufficiently large number of calibration events is available, which make individual wire to wire corrections possible. So far only a global fit assuming all wires are identical has been performed. The resolution along the wire in  $\phi$  is shown in Figure 9.5. From Chapter 3 we know that it depends

on the measured charge. Because the inner wires collect less charge, their  $\phi$  resolution is worse compared to the outer wires. Taking the  $\phi$  coordinate of the track at the radius of the CIZ hit and calculating the difference to the  $\phi_{CIZ}$  given by charge division, the resolution can be determined and, if necessary, we may also calibrate the charge division constants.



## 10 Chamber performance at HERA

### 10.1 Operation at HERA

The CIZ is the innermost drift chamber in the H1 detector and is therefore very sensitive to the background conditions. The number of hits from e-p collisions compared to cosmic tracks is much higher as shown in Figure 10.1. The sensitive current meter, which is introduced in the potential wire supply lines allows to measure the load of the chamber. The current depends on the rate because it is proportional to the collected charge per time for a normally running detector. In the first luminosity period of 1992 the maximum currents per ring were 50 nA which gave typically 10 nA / 20 mb<sup>-1</sup> (luminosity). The beam tune quality varied dramatically and the measured currents in the CIZ were

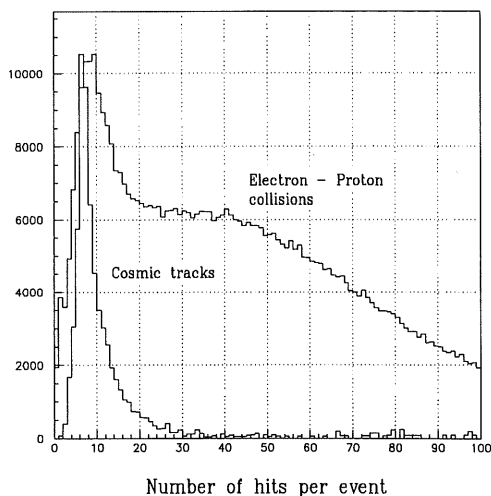


Figure 10.1: Number of hits per event. For cosmic tracks it peaks at 6, which is exactly what one expects.

strongly correlated with it. A gas mixture of 80/20 Ar / CH<sub>4</sub> was used. During this first running phase under beam conditions some problems occurred with the operation of the chamber. Firstly the last ring in  $-z$  direction could no longer be operated with the desired voltage on the potential wires following an electron beam loss near the H1 detector. Strangely, and unexplainably this effect disappeared after a period of time with no collisions. Cosmics could still be measured with full voltage. Since similar effects have been described in the literature [68], and have been cured by adding a small percentage

of water to the gas mixture, we also added 0.2% water. In 1993 the running period, the electron-proton beam currents and therefore the luminosity was higher by one order of magnitude. As a consequence the chamber currents increased roughly proportional to the luminosity. Figure 10.2 shows the currents measured for the 1993 period and the actual high voltage settings. During the cosmic test phase (run number < 50000) no currents could be measured on the potential wires, which means that they were less than 1/10 of a nanoampere. The values near 50 and 25 nA represent the load currents during the switching on phase of the chamber for different ramp up times. Despite the admixture of

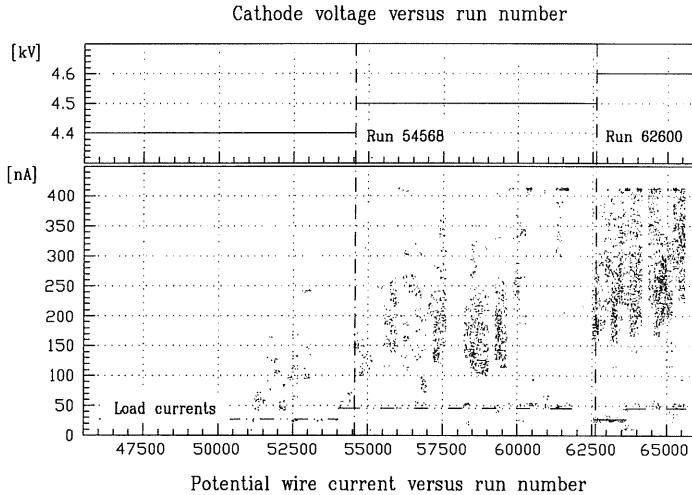


Figure 10.2: Potential wire current during the 1993 luminosity periode. The upper picture shows the corresponding cathode voltage.

0.2% water to the chamber gas the problems with the potential wire voltage on the last ring occured again after a short running time. During the whole running period further rings started to show the same effect, with the consequence that one had to reduce the voltage on the corresponding wires too.

## 10.2 Efficiency

To determine the efficiency a simple procedure was used which relies only on the data from the CIZ. This allows a fast and independent check of the detector. If a track crosses the cell at a certain distance from the wire plane, it is clear from which wires one expects a signal. Therefore one looks first at a signal on the outer wires, which lies in a given time

window. The minimum time is chosen in a way that the tracks do not pass near the center of a cell to avoid ambiguities. Given a pulse one then searches for a hit on an inner wire. These two hits define a line on which the third hit must be. In addition, shifting the time window over the drift cell, allows to study the dependence of the efficiency on the drift time, e.g. the drift distance. To avoid a bias, introduced by protons from e-p collisions,

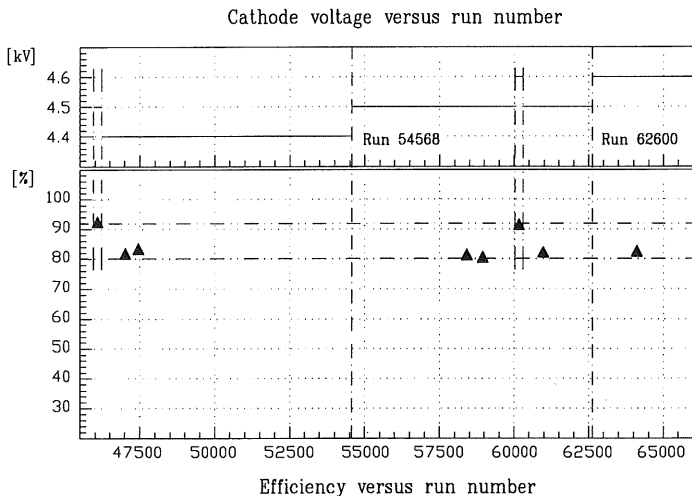


Figure 10.3: The efficiency and the cathode voltage as a function of run number for the 993 luminosity period.

minimum ionizing cosmic were always used to determine the value of the efficiency. The results and the corresponding voltage settings are illustrated in Figure 10.3. It shows a main loss already after a short period of collisions of about 10%. To improve the efficiency a high voltage was increased twice. But in both cases the efficiency decreased to 80% after a short period of collisions. This effect can now be explained by the deposits found in the signal wires (see Chapter 10.5).

### 0.3 Correlation of beam and chamber currents

The information, provided by the slow control and the current monitor system allows to study the correlations between the chamber currents and the HERA electron and proton beams. The measured chamber current provides also information about the background conditions and can therefore serve as a criteria to turn the tracking chambers off. Figure 10.4 shows the correlation between the chamber current measured in one CIZ ring plotted

against the electron and the proton beam current, the ToF (Time of flight detector, see Chapter 2) background and the luminosity. The fact, that for a small range of proton

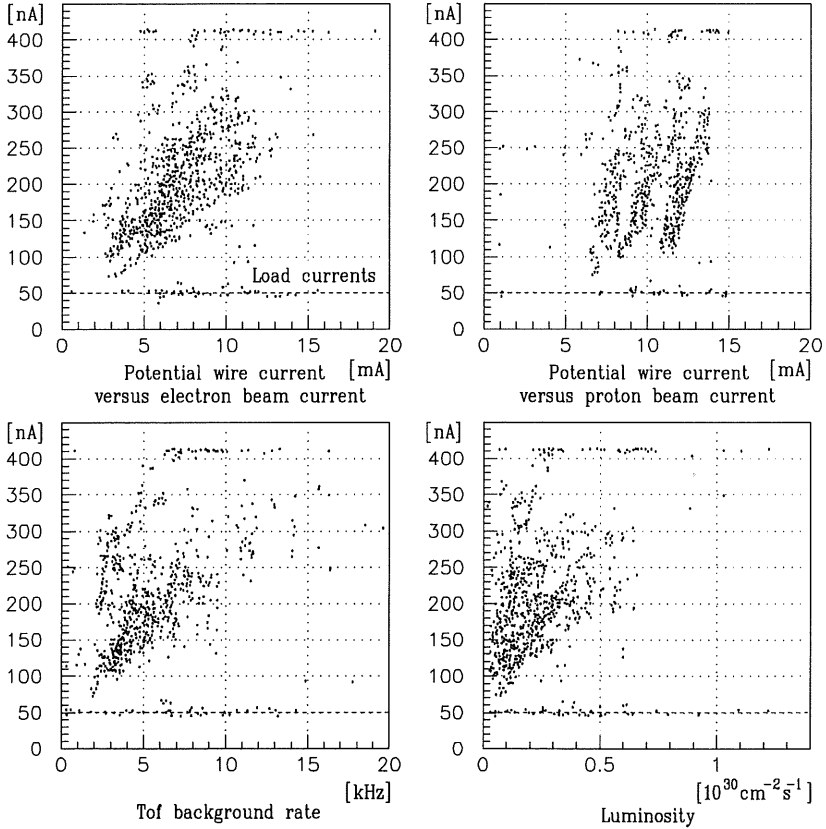


Figure 10.4: Potential wire current correlations. The structure in the upper right picture indicates, that the current is mainly dependant on the electron beam.

beam current the chamber current varies quickly can be explained by the decrease of the electron current. The lifetime of the electron beam is typically a few hours, while a proton fill can last for days. The correlation between electron and chamber current is quite clear, which indicates that the load of the chamber originates mainly from the electron beam. This can be illustrated by inspecting one proton fill (Figure 10.5). The proton current, the electron and the corresponding chamber current are plotted versus the run number

(time). Since the proton current stays rather constant for both electron fills one can clearly deduce the dependence on the electron beam current (Figure 10.6). Ideally the

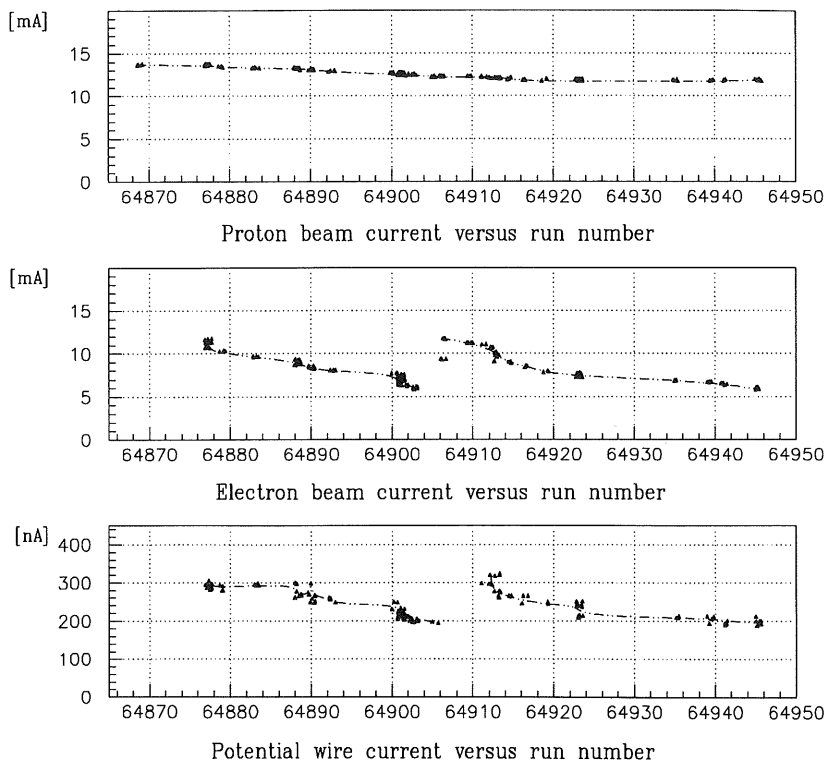


Figure 10.5: Electron and proton currents for a proton filling. For the second electron filling the proton current stays rather constant.

chamber should only see collisions from the vertex, but even without colliding beams the background is rather high. This is shown in Figure 10.7 where the influence of the electron beam is illustrated. Even the electron beam alone causes a high chamber current. The large fluctuations are due to manipulations of the synchrotron radiation shielding masks. This indicates that the background comes mainly from synchrotron radiation.

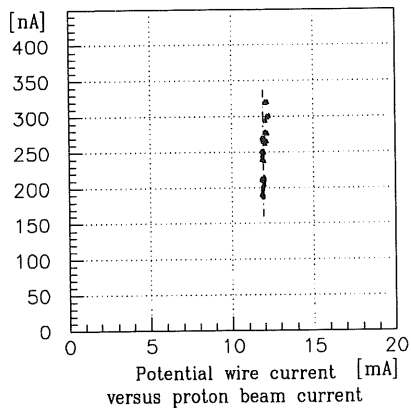
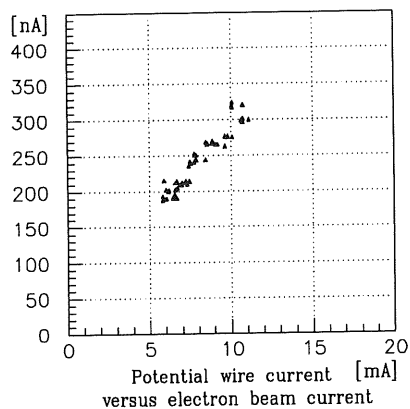


Figure 10.6: Potential wire correlations for one electron filling. The proton current is constant, so that one clearly sees the dependence of the chamber current on the electron beam.

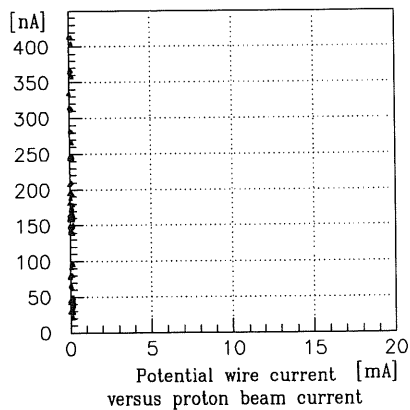
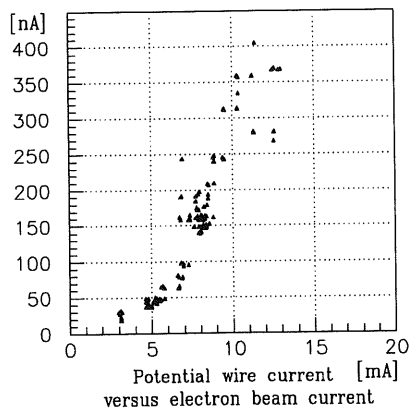


Figure 10.7: Potential wire current measured only with electrons.

## 10.4 Estimation of the total accumulated charge

In order to explain the gain loss and the wire deposits (see the next chapter) knowing the total accumulated charge on the sense wires will provide valuable information. From the scatter plot in Figure 10.8, which contains the values from the 1993 luminosity period, we deduce the average chamber current per electron beam current to be  $(40 \pm 15)$  nA / mA per ring. With an average electron beam current of 7.7 mA, an average running time of 817 s per run and 3190 runs [69] the total accumulated charge may be estimated

$$Q_{Total} = 3190 \times 817 \times 7.7 \times (40 \pm 15) \times 10^{-9} \text{As} = (0.8 \pm 0.3) \text{As} .$$

This is approximately the charge collected on the four sense wires in one drift chamber ring where each is about 120 cm long. Therefore the accumulated charge per unit length is

$$Q = \frac{Q_{Total}}{4 \times 120 \text{cm}} = (0.0017 \pm 0.0007) \text{Cb/cm} .$$

This is at least a factor of 6 less than the total accumulated charge, for which radiation damage effects have been reported in the literature [70].

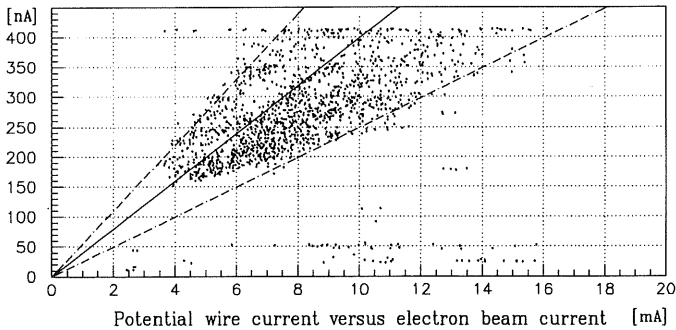


Figure 10.8: Potential wire current versus the electron beam current.

## 10.5 Analysis of the wire surfaces

To trace the origin of the high voltage problems at the potential wires and the gain loss in the detector we analysed the wire surfaces. All sense wires showed visible deposits. The layer thickness as seen on the raster electron microscope photograph in Figure 10.11 reaches up to a few  $\mu\text{m}$ . The elements, found on the surface by an EDAX (Energy dispersive analysis of X-rays) analysis are exactly the ones which we expected although we did not want to expect them. As shown in Figure 10.10 we found carbon and silicon. In the rings which showed high voltage problems, we discovered spots with carbon deposits on the potential wires. The result is shown in Figure 10.10.

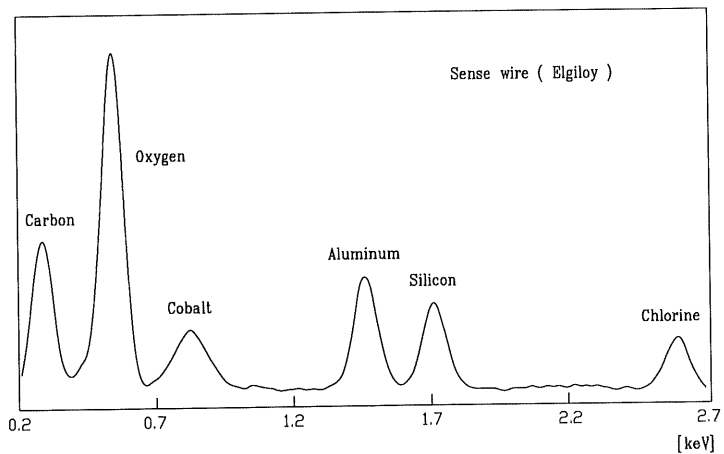


Figure 10.9: Elements found on sense wire surface.

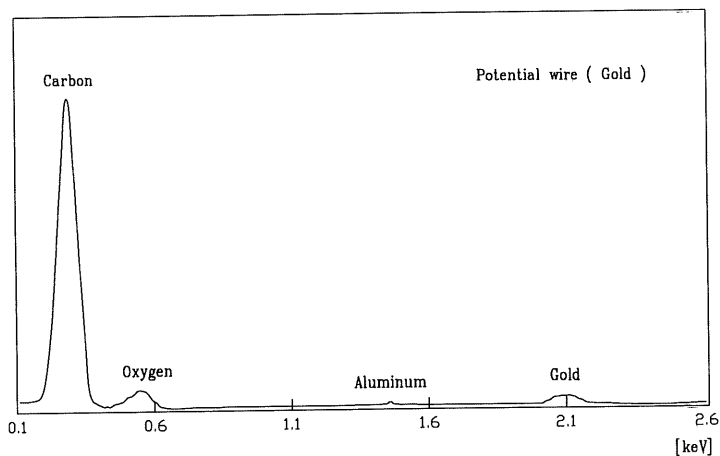


Figure 10.10: Elements found on potential wire surface.



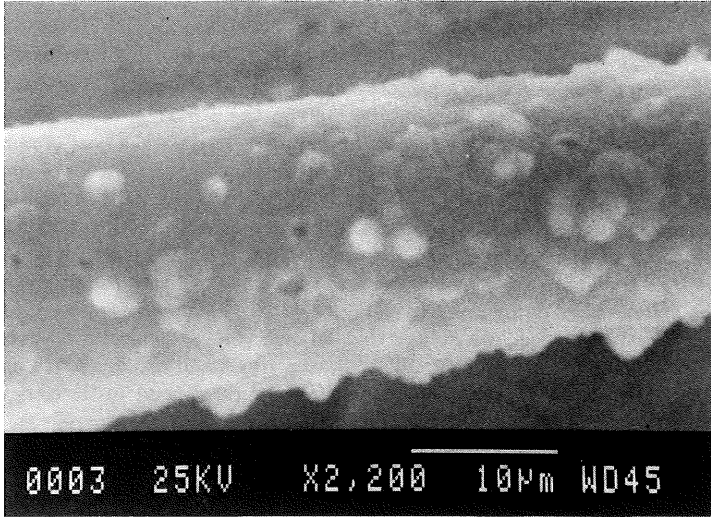


Figure 10.11: Photograph of a sense wire, which was taken out of the CIZ during the winter shutdown 1993.

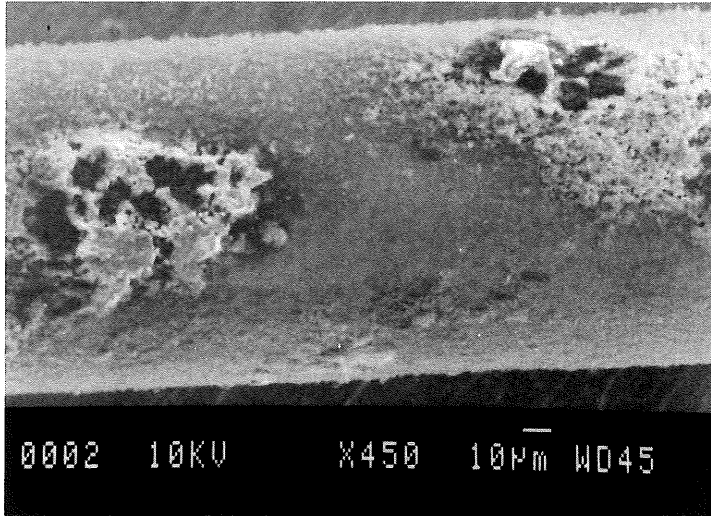


Figure 10.12: Photograph of a potential wire, which was taken out of the CIZ during the winter shutdown 1993.

## 11 Summary

Based on experience gained with a prototype and additional studies, described in this thesis, the full size detector was successfully built in the workshop of our institute. A major effort allowed to reduce the thickness of all parts. To meet the goal of minimizing the dead areas, many dimensions became quite small, which required a lot of specialized art work and new design concepts. Reducing the thickness of the walls as far as possible in the end lead to a rather fragile structure, which even required an element of luck, before it could be successfully introduced into the central part of the H1 tracking system. The experience from tests and operation showed that the technology used is quite reliable. No major high voltage breakdowns were encountered so far, which were expected to be one of the most serious problems, considering that all high voltage connections are buried in the chamber support body, and that isolation over very small distances was necessary. The measured resolutions in  $z$  and along the wire in  $\phi$  correspond to the design values and are compatible with those from the prototype.

The CIZ was operated in the luminosity periods of 1992 and 1993. The load in the central part of the H1 detector from the background seems to be considerable. The charge introduced by the synchrotron radiation background is larger. It is distributed over only 60 signal channels in this detector. Compared to the central inner multiwire proportional chamber (CIP) with about the same active volume, but  $2 \times 480$  wires, this is 10 times less and of course a disadvantage. Low angle tracks e.g. background coming from vertices outside of the detector may produce primary electrons over the whole length of a drift cell, finally producing huge pulses. The currents may be large enough, that impurities in the gas from outgassing materials or leftover dirt from the construction may crack near the wires and produce deposits, which will then hamper optimal operation of the detector. Adding water to the gas mixture did not eliminate these effects, and we did not try ethanol which has been considered as an alternative in the past. Part of these problems may be due to the adverse conditions under which this chamber had to be built in the old institute (insufficient clean room) and hence should be remedied in the construction of future detectors in the new clean room. The data quality is also affected by the actual noise conditions. Compared to stand alone tests we discovered a 10 MHz background induced by the synchronisation frequency (HERA clock). Most of this noise can be suppressed with a simple method at the scanner level, but the signal slope will still be influenced.

The analysis of the wire deposits explains the gain drop, but it is still not quite understood what caused the ageing. The accumulated charge is too low to explain it. Therefore in the next luminosity period the chamber will be operated with another gas mixture (Ar / Ethane (50 / 50)) to study the influence of the gas mixture. In one ring we changed also the signal wire type from the original high resistivity wire (Elgiloy) to gold plated tungsten rhenium with a lower resistivity. This will provide information on the influence of the wire material. To equalize the difference in the charges seen by the inner

and outer wires, we increased the input resistance of the line driver for the inner wires. This will decrease the charge division resolution somewhat, but lead to larger signals.

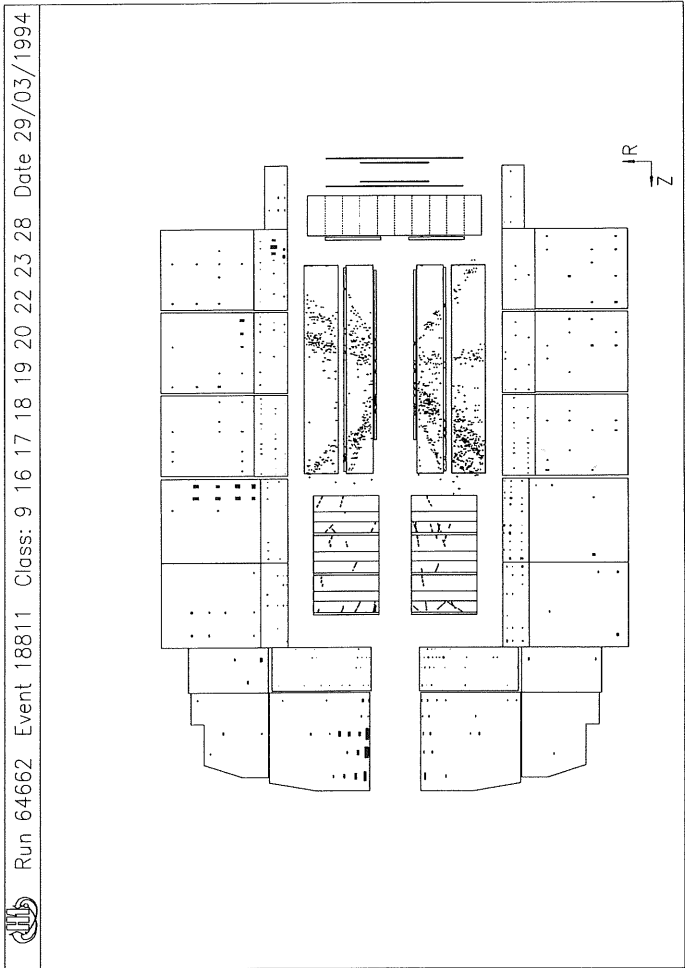


Figure 11.1: High  $Q^2$  event seen in the H1 detector.

## References

- [1] B. H. Wiik, HERA status, in ref. [8], vol. I, p. 1.
- [2] F. Willeke, in ref. [71], p. 28.
- [3] G. Wolf, Deutsches Elektronen-Synchrotron, DESY, Hamburg, 1986, DESY 86-089.
- [4] J. Feltesse, Measurement of inclusive differential cross sections, DPhPE, CEN-Saclay, France.
- [5] J. Feltesse, HERA the new frontier, December 1991, DPhPE 91-22, CEN-Saclay, France.
- [6] A. Jacquet, and F. Blondel, in ref. [72], p. 391.
- [7] Proc. of the HERA workshop, Hamburg (1987), R. D. Peccei ed., DESY, Hamburg (1988), vol. I, II.
- [8] Proc. of the workshop on Physics at HERA, Hamburg (1991), W. Buchmüller and G. Ingelman eds., DESY, Hamburg (1992), vol. I, II, III.
- [9] G. Bernardi, W. Hildesheim, A detailed simulation of  $F_2$  measurability at HERA, LPNHE-Paris report LPNHE-92-01 (1992); in ref. [8], vol. I, p. 79.
- [10] W. Bartel et al., Prospects for charm physics with the H1-Detector at HERA, pres. by F. Ould-Saada, Proc. 4<sup>th</sup> Int. Symp. on Heavy Flavour Physics, Orsay, France (1991), eds. M. Davier, and G. Wormser (Editions Frontières, Gif-sur-Yvette 1992), p. 515; see also S. Egli et al., in ref. [8], vol. II, p. 770.
- [11] H1 Collaboration: I. Abt et al., The H1 Detector at HERA, DESY 93-103, July, 1993.
- [12] R. L. Gluckstern, Nucl. Instr. and Meth. **A24** (1963) 381.
- [13] M. Schulz, Untersuchung von Methoden zur Kalibrierung der H1-Jetkammer, DESY FH1T-93-01.
- [14] Particle data booklet.
- [15] F. Sauli, Principles of operation of multiwire proportional and drift chambers, CERN 77-09.
- [16] K. Kleinknecht, Detektoren für Teilchenstrahlung, Teubner 1992.
- [17] W.W.M. Allison and J.H. Cobb, Ann. Rev. Nucl. Sci. **30** (1980) 253.
- [18] H.A. Bethe, Annalen d. Physik **5** (1930) 325.

- [19] L.D. Landau, J. Exp. Phys. (USSR) **8** (1944) 201.
- [20] R.M. Sternheimer, Phys. Rev. **88** (1952) 851.
- [21] J. Fehlmann, The time expansion chamber, Diss. ETH Nr. 8711.
- [22] J.H. Parker and J.J. Lowke, Phys. Rev. **181** (1968) 290.
- [23] G. Schultz, CERN EP Internal Report 76-19 (1976).
- [24] J. Groh, Computersimulation der Elektronenlawine in zylindersymmetrischen elektrischen Feldern, DESY FH1T-89-03.
- [25] S.A. Korff, Electrons and nuclear counters (Van Nostrand, New York, 1946).
- [26] S. Eggli, Schnelle Zweitkoordinaten Bestimmung bei Driftkammern und ihre Anwendung bei H1 Spurdetektoren, Uni Zürich 1990.
- [27] V. Radeka and P. Rehak, IEEE Trans. Nuc. Sci. NS-26 (1979) 225.
- [28] T.J. Killian - BNL, CERN-EP, 80-35 (1980).
- [29] G.A. Erskine, Nucl. Instr. and Meth. **A105** (1972) 565.
- [30] R. Klatt et al.,MAFIA - A three dimensional electromagnetic CAD system, Proceedings of the 1986 Linear Accelerator Conference, SLAC-303 (June 1983), p.276.
- [31] J. Fehlmann, WIRCHA a program package to simulate drift chambers, ETH Zürich (1985).
- [32] R. Veenhof, GARFIELD a drift chamber simulation program, CERN (1991).
- [33] E. Hoefner and H. Nielinger, SPICE Analyseprogramm für elektronische Schaltungen, Springer Verlag 1985, (ISBN 3-540-15160-5).
- [34] R.J. Ellison and U. Straumann, The H1 trigger, DESY, H1-05/90-137.
- [35] F. Piuz, CERN-EF 82-11 (1982).
- [36] Z. Kowalski, Nucl. Instr. and Meth. **A234** (1985) 521.
- [37] S.Shalev and P. Hopstone, Nucl. Instr. and Meth. **155** (1978) 237.
- [38] M.W. Charles, J. Phys. E: Sci. Instr. **5** (1972) 95.
- [39] M.E. Rose and S.A. Korff, Rhys. Rev. **59** (1941) 850.
- [40] A. Zastawny, J. Sci. Instr. **43** (1966) 179.
- [41] W. Diethorn, Report NYO-6628 (1956).

- [42] Kapton (Polyimid), Du Pont International SA, 1211 Genf 24, Switzerland.
- [43] Rohacell 51: Roehm GmbH, Darmstadt, Germany.
- [44] Araldit: epoxy glue manufactured by CIBA-Geigy AG, Basel, Switzerland.
- [45] Glass fiber reinforced epoxy (Vetronit), Schweizerische Isola-Werke, 4226 Breitenbach, Switzerland.
- [46] Elgiloy, American fine wire Company, Grover City, Cal. 93433. (It is an alloy of 39.53% Co, 20.34% Cr, 15.42% Ni, 15.25% Fe, 7.16% Mo, 1.95% Mn, 0.48% Si, 0.07% C and a trace amount of Be. The 20  $\mu\text{m}$  diameter has a yield strength of 350 kpsi, a tensile strength of 390 kpsi.) With the resistance per unit length  $\cong 3 \text{ k}\Omega/\text{m}$ .
- [47] Müller Feindraht AG, American fine wire, 8800 Thalwil, Switzerland.
- [48] Feedthroughs manufactured by H. Girod SA.
- [49] Vespel (Polyimid), Du Pont International SA, 1211 Genf 24, Switzerland.
- [50] Foils manufactured by R. Goulon, 8134 Adliswil, Switzerland.
- [51] H. B. Dreis, Bau einer automatisierten Gaschromatographie Messtation für den H1 - Detektor, Diploma thesis, RWTH Aachen (1991), unpublished.
- [52] W. A. Dietz, Response factors for gas chromatography, Esso Res. and Eng. Co., Analytical Res. Div., Linden, New Jersey, 68 (1967).
- [53] S. Masson, Ph. D. thesis, RWTH Aachen (1993), unpublished.
- [54] CAEN High Voltage System SY 127, Costruzioni Apparechiature Elettroniche Nucleari S.p.A., I-55049 Viareggio.
- [55] K. Esslinger, and P. Rößmann, A sensitive current monitor for drift chambers, Nucl. Instr. and Meth. **A334** (1993) 649.
- [56] The VMEbus specification, IEEE standard 1014.
- [57] W. J. Haynes, Bus-based architectures in the H1 data acquisition system, VITA Int. Conf. Open Bus Systems '92 in Research and Industry, Zürich, Switzerland, (1992), ISBN 90-72577-11-6 (1992) 27; Rutherford Appleton Laboratory report RAL 92-048 (1992).
- [58] W. J. Haynes, Experiences at HERA with the H1 data acquisition system, in ref. [73], p. 151; DESY report 92-129, Hamburg (1992).
- [59] Figure courtesy W. J. Haynes.
- [60] E. Elsen, The H1 trigger and data acquisition system DESY, H1-01/93-262.

- [61] S. Eichenberger, A fast pipelined trigger for the H1 Experiment at HERA, Ph. D. thesis, Universität Zürich, (1993).
- [62] W. Zimmermann et al., A 16 channel VME flash ADC system (F1001-FADC), H1 internal report, DESY, Hamburg (1989), unpublished; manufacturer: Struck, Tangstedt/Hamburg.
- [63] J. Va'Vra, Nucl. Instr. and Meth. **A244** (1985) 391.
- [64] D.P. Sankey, Simultaneous track reconstruction and electron identification, RALT-115.
- [65] C.A. Meyer, The central inner z-chamber online and offline reconstruction software, 19 March, 1993.
- [66] B. Fominykh and F. Linsel, A short description of the H1REC modules CNREC and CNBREC, H1 software note number 42, September, 1993.
- [67] P. Robmann et al., Nucl. Instr. and Meth. **A277** (1989) 368.
- [68] H. Kado, Performance of the JADE vertex detector, Proceedings of the Workshop on radiation damage to wire chambers, LBL-21170 UC-34D CONF-860162, p.207.
- [69] S. Levonian, DESY Hamburg, private communication .
- [70] J. A. Kadyk, Nucl. Instr. and Meth. **A300** (1991) 436.
- [71] Proc. XV<sup>th</sup> Int. Conf. on High-Energy Accelerators, Hamburg (1992), J. Rossbach ed., Int. J. Mod. Phys. A (Proc. Suppl.) **2A** (1993).
- [72] Proc. of the study for an *ep* facility for Europe (1979), U. Amaldi ed., DESY-report 79-48 (1979).
- [73] Proc. Int. Conf. on Computing in High Energy Physics 92, Annecy, France (1992), eds. C. Verkerk and W. Wojcik, CERN-Report 92-07, Geneva (1992).

## Acknowledgements

I have experienced a very enjoyable and most interesting time at the Physik-Institut. The friendly atmosphere enabled my creativity to blossom. I want to thank everyone very much for their contributions to this work.

In relation with the experiment I had the opportunity to spend a great and valuable time at the Deutsches Elektronen-Synchrotron (DESY) in Hamburg. Many thanks to all the people of the H1 collaboration.

This work was supported by the Swiss National Foundation.



## Curriculum vitae

### Personalien

Name : Robmann  
Vorname : Peter  
Geboren : 10. 3. 1957 in Dottikon AG  
Bürgerort : Turbenthal

### Bildungsgang

1964 - 1974 : Primarschule und Bezirksschule in Dottikon und Lenzburg  
1974 - 1977 : Kantonsschule in Aarau, Matura Typus C  
1978 - 1988 : Studium der Physik (Mathematik, Astronomie)  
an der Universität Zürich  
1988 : Diplom in Experimentalphysik  
Diplomarbeit : 'Entwicklung und Bau eines  
zylindrischen Driftkammer-Prototyps  
für den H1 Detektor'  
Unter Leitung von Prof. Dr. P. Truöl  
1988 - 1994 : Wissenschaftliche Mitarbeit beim H1 Experiment am  
Elektron-Proton Speicherring HERA in Hamburg (DESY)  
und Dissertation bei Prof. Dr. P. Truöl

### Dozentenverzeichnis

H. Amann	W. Kündig	G. Scharf
C. Amsler	P.F. Meier	H.R. Schwarz
D. Brinkmann	V. Meyer	A. Steiner
E. Brun	H.H. Müller	J.O. Stenflo
R. Engfer	M. Nagasawa	H.H. Storrer
P. Gabriel	U. Niederer	N. Straumann
M. Greuter	H. Nussbaumer	K. Strebel
H. Jarchow	B.D. Patterson	A. Thellung
W. Jaus	H. Pruis	P. Truöl
G. Karrer	G. Rasche	M. Waldmeier
H. Keller	W. Reichert	F. Waldner